



HAL
open science

Statistical inference of Water Column Depth through radiometric and geometric analysis of Spectral Imagery

Mohamed Ali Ghannami

► **To cite this version:**

Mohamed Ali Ghannami. Statistical inference of Water Column Depth through radiometric and geometric analysis of Spectral Imagery. Engineering Sciences [physics]. ENSTA Bretagne, 2024. English. NNT: . tel-04880318

HAL Id: tel-04880318

<https://hal.science/tel-04880318v1>

Submitted on 10 Jan 2025

HAL is a multi-disciplinary open access archive for the deposit and dissemination of scientific research documents, whether they are published or not. The documents may come from teaching and research institutions in France or abroad, or from public or private research centers.

L'archive ouverte pluridisciplinaire **HAL**, est destinée au dépôt et à la diffusion de documents scientifiques de niveau recherche, publiés ou non, émanant des établissements d'enseignement et de recherche français ou étrangers, des laboratoires publics ou privés.



Distributed under a Creative Commons Attribution - NonCommercial 4.0 International License

THÈSE DE DOCTORAT DE

L'ÉCOLE NATIONALE SUPÉRIEURE
DE TECHNIQUES AVANCÉES BRETAGNE

ÉCOLE DOCTORALE N° 648
Sciences pour l'Ingénieur et le Numérique
Spécialité : *Signal, Image, Vision*

Par

Mohamed Ali GHANNAMI

Statistical Inference of Water Column Depth through Radiometric and Geometric Analysis of Spectral Imagery

Thèse présentée et soutenue à le 6 décembre 2024 à l'ENSTA Bretagne, France

Unités de recherche : Lab-STICC (UMR CNRS 6285), ENSTA Bretagne

Département des sciences géomatiques, Université Laval

Rapporteurs avant soutenance :

Jocelyn CHANUSSOT Research Director, INRIA
Anders KNUDBY Associate Professor, University of Ottawa

Composition du Jury :

President :	Thierry CHONAVEL	Professor, IMT Atlantique
Examiners :	Audrey MINGHELLI	Professor, University of Toulon
	Thierry CHONAVEL	Professor, IMT Atlantique
	William NEY CASSOL	Assistant Professor, Université Laval
Thesis Director :	Isabelle QUIDU	Associate Professor HDR, ENSTA Bretagne
Co-Thesis Director :	Sylvie DANIEL	Full Professor, Université Laval
Supervisor :	Guillaume SICOT	Associate Professor, ENSTA Bretagne

Contents

Contents	ii
List of Figures	v
List of Tables	vii
Introduction	1
1 Spectral Imagery Analysis in Coastal Monitoring	12
1 Spectral imagery characteristics	12
1.1 MS and HS resolutions	14
1.2 Sensor arrays	15
1.3 Acquisition Platform Classification	16
Satellite imagery characteristics	16
Medium-altitude imagery characteristics	17
Close-Altitude Imagery characteristics	19
2 Radiometric WCD estimation	20
2.1 Empirical approaches	20
2.2 Radiative transfer approaches	20
2.3 Calibration and Atmospheric Correction in RT approaches	22
Radiometric data calibration	22
Remote Sensing Reflectance	23
3 Geometric WCD estimation	24
3.1 3D reconstruction in land photogrammetry	25
Rigorous methods	25
Approximate methods	25
3.2 3D reconstruction in through water photogrammetry	26
Corrective approaches	26
Ray tracing approaches	27
2 Statistical Inference for Uncertainties in Environmental Parameters Analysis	30
1 Theoretical foundations	31
1.1 Main inference perspectives	32
1.2 Uncertainty and inference metrics	33
2 Variance-covariance framework	35
3 Likelihood-based inference framework	37
4 Profile likelihood-based inference	39

4.1	Nuisance in radiometric and geometric inference	39
4.2	First-order inference	40
4.2.1	Profile likelihood	40
4.2.2	First-order statistical tests	41
4.3	Evaluation of Confidence Intervals performance	42
5	Higher-order asymptotic inference	44
5.1	Sufficiency and ancillarity	45
5.2	Modified likelihood ratio	46
5.3	Profile likelihood adjustments	47
6	Practical aspects of likelihood based inference	48
3	A Likelihood-based Triangulation Method for Uncertainties in Through Water Depth Mapping	51
1	Methods for uncertainty evaluation in through water photogrammetry . . .	52
2	Methodology	54
2.1	Approach and rationale	54
2.2	Pose probabilistic modeling	55
2.3	Geometric likelihood	59
2.3.1	Positional likelihood	60
2.3.2	Refracted likelihood	61
3	Results	62
3.1	Experimental setup	63
3.2	Water Column Depth inference	65
3.2.1	Water Column Depth Uncertainties	65
3.2.2	Evaluation of uncertainty metrics	68
3.3	Water Air Interface height inference	69
4	Discussion	73
5	Conclusion	75
4	Likelihood-based Inference for Bathymetric Uncertainties in Semi-Analytical Models	76
1	Related works	77
1.1	R_{rs} uncertainty evaluation	77
1.2	WCD uncertainty in Semi-Analytical models	78
2	Methodology	79
2.1	Shallow water Semi-Analytical model [14]	80
2.2	Statistical modeling	82
3	Results	83
3.1	Experimental setup	83
3.2	WCD profiling results	86
3.2.1	Profiling analysis	86
3.2.1.a	Ideal case	86
3.2.1.b	Asymmetric case	87
3.2.1.c	Practical identifiability case	90
3.2.1.d	Outliers case	91
3.2.2	Refinement impact	93
3.3	First-order inference results	95
3.3.1	Hyperspectral data	95

3.3.2	Multispectral data	98
3.4	Second-order inference results	102
4	Discussion	104
5	Chapter conclusion	106
5	Conclusion	107
1	Revisiting research objectives	107
1.1	Geometric WCD inference	108
1.2	Radiometric WCD inference	109
2	Implications for future research	110
2.1	Practical applications	111
2.1.1	Application to real datasets	111
2.1.2	Integration with existing technologies	112
2.2	Integrated approaches	113
2.2.1	Expanded application of likelihood-based inference	113
3	Final perspectives	114
A		116
1	GUM methodology for uncertainty	116
1.1	Variance-covariance matrix in linear and non-linear models	117
2	Equivalence between the EFIM Wald test and the variance-covariance propagation under Gaussian errors	118
3	Derivation of the profile adjustment	119
B		120
1	Absorption	120
2	Backscattering	120
3	Academic achievements	122
	Bibliography	123

List of Figures

0.1	Passive imaging and vertical datums in coastal zones with passive imagery . . .	2
0.2	Inference scheme in spectral imagery in radiometric and geometric approaches	7
0.3	Methodology Diagram for Radiometric and Geometric Inference	9
1.1	The solar spectrum at extraterrestrial and sea level conditions	13
1.2	Overlay of spectral response functions and reflectance of different surfaces . . .	15
1.3	Remote sensing images from drone, airborne, and satellite platforms	17
1.4	Remote sensing coastal zones with passive imagery	21
2.1	Conceptual illustration of precision, accuracy, trueness	34
2.2	Least squares estimation with variance-covariance	36
2.3	Geometric interpretation of Fisher Information	38
2.4	Geometric illustration of profile Likelihood	41
2.5	First-order statistical tests and hypothesis testing	44
3.1	Representation of refraction geometry.	56
3.2	Quaternion based rotation for camera attitude.	57
3.3	Illustration of the Bingham concentration parameter influence.	59
3.4	Geometric configurations for drone scenario for a FoV of 48° and an overlapping of 60%.	63
3.5	Normalized \mathbf{x}_f profile likelihood 2D heatmaps	65
3.6	WCD uncertainties with t_o based 95% confidence intervals.	66
3.7	Drone scenarios: rejection rates of r and t_o statistics.	68
3.8	Airborne scenarios, point P_c : rejection rates of r and t_o statistics.	69
3.9	Drone and "Excellent" INS scenario: WAI height inference based on Likelihood profiling for 1 and 10 samples.	70
3.10	Drone, P_c scenarios, WAI height uncertainty across different INS classes.	71
3.11	Depth averaged WAI height uncertainty across different INS classes and sample Sizes for each point.	72
4.1	Profile likelihood ideal scenario in the WCD radiometric inference	86
4.2	First-order test statistics curves in an ideal scenario in the WCD radiometric inference	87
4.3	Profile likelihood and first-order test statistics curves for an asymmetric case in hyperspectral scenarios	88
4.4	Statistical distribution of the WCD MLE for the parameterization TWDB at a WCD of 20 meters in the hyperspectral scenario	89
4.5	Profile likelihood and first-order test statistics curves for an asymmetric case in multispectral scenarios	89

4.6	Profile likelihood and first-order test statistics curves depicting practical unidentifiability in multispectral scenarios	90
4.7	Profiling outlier cases in hyperspectral and multispectral scenarios	92
4.8	Violin plot for the Wald statistic t_e at 1m depth in clear water conditions . . .	96
4.9	Violin plots of computed 95% CI from first-order statistical tests in the hyperspectral scenario	97
4.10	Violin plots of computed 95% CI in the multispectral scenario for 1 meter . . .	99
4.11	Violin plots of computed 95% CI in the multispectral scenario for 1 meter . . .	100
4.12	Violin plots of computed 95% CI from first-order statistical tests in the multispectral scenario	101
4.13	Second-order adjustments in multispectral and hyperspectral data for the scenario TWDB at 5 meters	103

List of Tables

1	Inference Notations	viii
2	Radiometric Notations	ix
3	Geometric Notations	x
1.1	Comparative Overview of Satellite Platforms for Coastal Remote Sensing	18
3.1	Base-Height ratios for homologous points for both drone and airborne scenarios	64
3.2	Experimental setup classes for the WCD geometric inference under different camera pose qualities.	64
4.1	Radiometric analysis parameterizations	83
4.2	Operational configuration for the radiometric WCD inference under SA model	84
4.3	Visualization of spectra at different depths for each parameterization.	85
4.4	HySpex MLE refinement metrics	94
4.5	MSI-2 MLE refinement metrics	94
4.6	First-order statistical tests rejection rates for the HysPex sensor.	98
4.7	First-order statistical tests rejection rates for the MSI-2 sensor.	102
B.1	List of achievements	122

Thesis Notations and Symbols

In this study, italicized variables represent model parameters, while non-italicized variables typically refer to underlying data and the tilde variables are true parameter values. Bold variables denote vectorial or matrix entities.

Table 1 – Inference Notations

Symbol	Description
$\tilde{\boldsymbol{\theta}}$	True values of the parameters
\mathbf{y}	Observed data
$\boldsymbol{\theta}$	Parameters underlying the data
ψ	Interest scalar parameter
$\boldsymbol{\omega}$	Nuisance vector parameter
$L(\psi, \boldsymbol{\omega}; \mathbf{y})$	Likelihood function
$\ell(\psi, \boldsymbol{\omega}; \mathbf{y})$	Log-likelihood function
$\hat{\boldsymbol{\theta}}$	Maximum Likelihood Estimates (MLE)
$\hat{\psi}$	MLE of interest parameter
$\hat{\boldsymbol{\theta}}_{\psi}$	Constrained MLE
$\hat{\boldsymbol{\omega}}$	MLE of nuisance parameter
$\ell_p(\psi; \mathbf{y})$	Profile log-likelihood
$r(\psi; \mathbf{y})$	Signed log-likelihood ratio statistic
$t_o(\psi; \mathbf{y})$	Wald test statistic using Observed Information
$t_e(\psi; \mathbf{y})$	Wald test statistic using Expected Information
$s(\psi; \mathbf{y})$	Score statistic
$j_p(\hat{\psi}; \mathbf{y})$	Observed Fisher Information of ψ at the MLE
$i_p(\hat{\psi})$	Expected Fisher Information of ψ at the MLE
$\mathbf{j}(\hat{\boldsymbol{\theta}}; \mathbf{y})$	Observed Fisher Information Matrix of $\boldsymbol{\theta}$ at the MLE
$\mathbf{i}(\hat{\boldsymbol{\theta}})$	Expected Fisher Information Matrix of $\boldsymbol{\theta}$ at the MLE
$\mathcal{A}(\mathbf{y})$	Estimated confidence interval
α	Significance level
$z_{\alpha/2}$	Critical value for $\alpha/2$ tail of standard normal distribution

Table 2 – Radiometric Notations

Symbol	Description
γ, ν, β	Semi-analytical empirical values from literature
R_{rs}^+	Above-surface remote sensing reflectance
R_{rs}^-	Subsurface remote sensing reflectance
z	Water Column Depth (WCD)
ω_c	Water column parameters
ω_b	Bottom parameters
$\rho(\omega_b)$	Bottom reflectance
α_m	Mixing ratio between sand and vegetation reflectances
a	Absorption coefficient
b_b	Backscattering coefficient
a_w	Absorption by water
a_ϕ	Absorption by phytoplankton
a_{cdom}	Absorption by colored dissolved organic matter (CDOM)
a_{nap}	Absorption by non-algal particles
Chl	Concentrations of chlorophyll
CDOM	Concentrations of colored dissolved organic matter
TSM	Concentrations of total suspended matter

Table 3 – Geometric Notations

Symbol	Description
\boldsymbol{v}_s	Interior orientation vector
\boldsymbol{v}_f	Line-of-sight unit vector
\boldsymbol{x}_f	Homologous point position vector
$[x_f]_x, [x_f]_y, [x_f]_z$	Homologous point object coordinates
h	Water Air Interface (WAI) height
\boldsymbol{x}_s	Parameter of sensor position vector
\mathbf{x}_s	Measured sensor position vector
$\boldsymbol{\Sigma}_s$	sensor position variance-covariance
\boldsymbol{q}_f	Line-of-sight quaternion
\mathbf{q}	Measured line-of-sight quaternion
M	Bingham orientation parameter
C	Bingham concentration parameter
h	Water-air interface height parameter
$n_{\text{water}}, n_{\text{air}}$	Refraction indices for water and air medium
ξ_i, ξ_r	Incidence angle and refracted angle
\boldsymbol{q}_{ref}	Backward refraction quaternion
\boldsymbol{v}_h	Backward refracted line-of-sight
\boldsymbol{x}_h	Incidence point
\boldsymbol{n}_z	Nadir vector

Introduction

General context

The coastal marine environment is of major interest to a broad spectrum of institutional structures as well as scientific communities and industrial entities. This is largely correlated with the economic and social stakes (e.g. harbour, urban areas), strategic issues and the commercial activities (e.g. aquaculture) concentrated in these areas [1]. Taking into consideration the coastal risk as the product of exposure, vulnerability and hazards (e.g. sea level rise), coastal zones monitoring and management are mandatory in order to guarantee a sustainable growth within the coastal cover [1; 2; 3].

Among the different information requested to conduct activities and increase knowledge about the coastal domain, bathymetry is one of the fundamental components. Indeed, bathymetry-derived products are crucial for most maritime applications in coastal zones : navigation safety (e.g. navigation charts compilation), harbor development (e.g. pre/post-dredging surveys), and monitoring aquatic resources. Bathymetry is also required for regional hydrodynamic models and, as such, for a variety of further downstream products which are related to the overall state of the coastal system such as surface currents, hydrology, and seabed morphodynamics. Bathymetry provides the morphology of ocean floors, lake floors or river floors. It should not be confused with the **Water Column Depth (WCD)**, as shown in the Figure 0.1, which is the difference from the water surface to the seabed. **WCD** is a strongly time-dependent measurand whereas bathymetry is a conceptually robust quantity which is defined with respect to a designated¹ vertical datum (chart datum in the figure) aiming to factor out variable components such as tidal oscillations. Except for satellite altimetry which is not relevant for the fine regional scales in coastal areas, bathymetry is often determined from **WCD** measurements. Consequently, the rest of the document will focus on the **WCD** measurements, crucial for the ultimate attainment of bathymetric information.

On the technological side, various innovations emerged in the last decades leading to the development of sensors which are dedicated to bathymetric measurements. Modern hydrographic

1. Chart Datum vertical reference is established through a deliberate and methodical process. This process considers regional tidal patterns and relies on empirical methods to predict and establish its long-term trends.

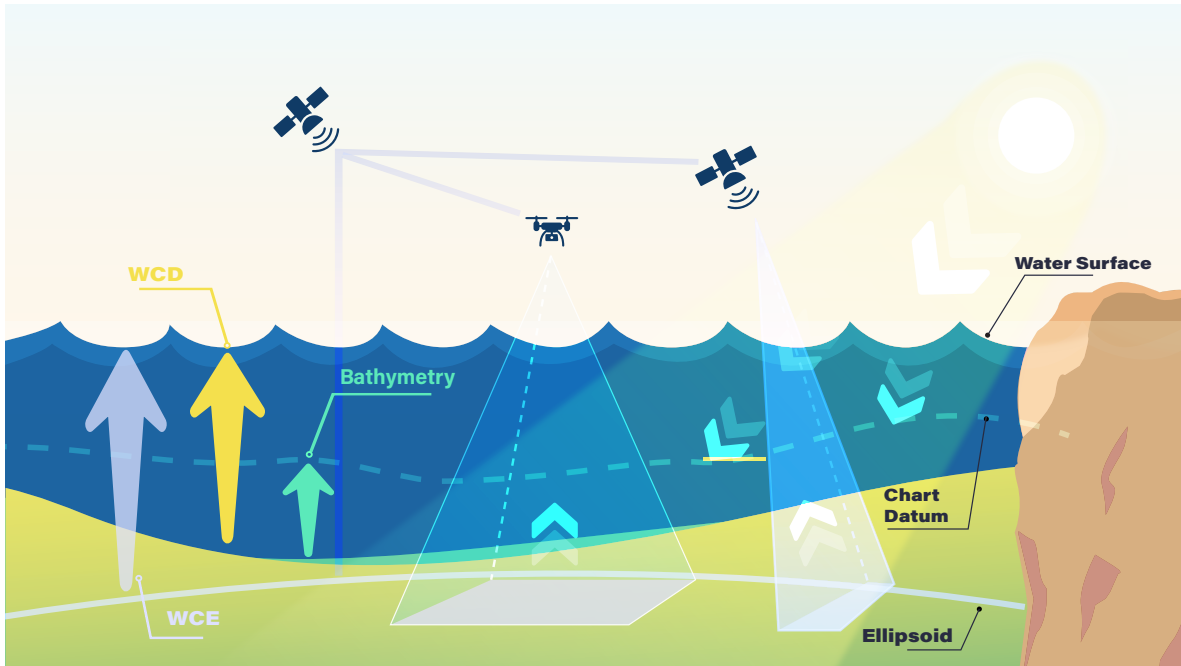


Figure 0.1 – Passive imaging and vertical datums in coastal zones with passive imagery: Bathymetry is counted from the seabed to the chart datum. WCD is counted from the seabed level to the sea surface level while Water Column Elevation (WCE) is counted from the reference ellipsoid to the seabed level. Two types of optical sensors are illustrated: frame cameras for the drone platform and a satellite based push-broom sensor (line scanner).

surveying techniques can be decomposed into two components: the sensor component which is related to the measurement principle and the navigation component which is related to the mobile mapping platform that is recurrent across surveying techniques (e.g. vessel, drone). The classical integration workflow organizes the survey area into elementary seabed nodes based either on the sampling properties of the sensor or a specified resolution. Each node is georeferenced in a reference system based on sensor mounting angles and lever arms, as well as the navigation hardware: Global Navigation Satellite Systems (GNSS) receivers and Inertial Navigation System (INS). After the integration of all sources of information (navigation and sensor measurements), subsequent processing is often required in order to compile bathymetric products.

The arsenal of surveying seabed sensors in coastal areas can be categorized into two main categories. The first category corresponds to the acoustic sensors (Sonars) such as Single-Beam Echo-Sounder (SBES) and Multi-Beam Echo-Sounder (MBES) for which the measurement principle is based on estimating the range which is traveled by an acoustic wave actively emitted by the sonar usually mounted on a hydrographic vessel. Compared to other forms of energy, such as electromagnetic waves, acoustic waves are the most effective for the marine environment due to their lower absorption and superior ability to propagate through water. As a consequence, these surveying technologies offer the best performances in terms of mea-

surement quality and processing chains maturity as they helped to shape the hydrographic standards across history. Nonetheless, they are less adapted for shallower waters (less than 5 meters) and rather require substantially greater investments (time, equipment and human resources).

The second category involves remote sensing technologies (aircrafts or satellite based) which can be associated to either **Light Detection and Ranging (LiDAR)** technology as an active sensor or to other passive optical sensors, based on **Charged Coupled Device (CCD)** or **Complementary Metal Oxide Semiconductor (CMOS)** arrays, which fall under the category of spectral imagers. An excellent review on the remote sensing technologies for measuring bathymetry can be found in [4].

Airborne **LiDAR** technology is increasingly gaining adoption in hydrographic surveys as it provides a cost-efficient mean for mapping shallow waters up to 40 meters depending on the water transparency citehydrobook. **LiDAR** technology is based on electromagnetic waves in the Blue-Green spectrum for penetration, ideally with an additional **InfraRed (IR)** channel for determining the water interface and hence the **WCD**. Notably, georeferencing techniques are analogous to those adopted in traditional acoustic surveys. **LiDAR** has also been adopted for bathymetry mapping in satellite missions such as the recent NASA's Ice, Cloud, and Land Elevation Satellite-2 (**ICESat-2**), launched in September 2018.

Conversely, passive imagers such as frame and push-broom sensors, provide an encouraging alternative for inferring the coastal waters optical properties as a complement to the previously cited active technologies. Indeed, a significant amount of research involving airborne and space based spectral imagery (**Hyperspectral (HS)**, **Multispectral (MS)**), has demonstrated the ability to retrieve water biophysical properties such as: chlorophyll-A concentration, suspended particles matter, benthic habitats in addition to the **WCD**. Passive imagery solutions not only offer access to synoptic scales but also provide a further more cost-efficient option for coastal bathymetry. This is especially due to their ability to provide frequent and synoptic observations, as well as the availability of crowd sourced and public spectral datasets, such as Sentinel-2 hub, and the evolution of image processing software.

Thus, **WCD** derived from optical imagery (**HS/ MS**) meets a crying need for adapted and efficient solutions for coastal and shallow areas.

Problem statement

The study of spectral imagery can be conducted based on two categories of information : radiometric and geometric. By radiometric information we refer broadly to the spectral signature associated to each pixel in the georeferenced data. The geometric information

originates from various sources: navigation data for the position and attitude of the platform, sensor viewing geometric properties such as the focal length and ground truth measurements which can be incorporated into the georeferencing procedure. Conveniently, the approaches for retrieving pixel-wise **WCD** are partitioned accordingly: radiometric and geometric.

Radiometric approaches

As for current applications in passive remote sensing, radiometry is the information commonly used to trace the **WCD** at a pixel-level in coastal areas by means of satellite or airborne spectral observations. Two main categories of approaches have been developed to map bottom depth from sea reflectance: empirical and radiative transfer based approaches [5].

Pioneering the empirical approaches, [6] has developed an empirical technique that adapts a linear band ratio regression model to the radiometric data. This model parameters can be evaluated with in-situ measurements. Empirical methods have certain shortcomings: sensitivity to spatial variability (seabed, atmospheric properties), requirement for in-situ measurements, and finally the difficulty of performing physical interpretations [5; 7; 8]. The second category of methods is based on the physical modeling of the radiative transfer of light in the water column to predict the reflectance of the sea surface as a function of the water column properties. The methods based on the radiative transfer constitute an alternative approach that can overcome the two latter issues of the empirical methods but can be exposed to the first one in a sense that they are vulnerable to spatial heterogeneity. The performance of the radiometric **WCD** methods is inherently dependent on the overall factors involved in the observation experiment: water quality (i.e. turbidity, color), atmospheric conditions (i.e. clouds, aerosol), seabed reflectance and sun illumination geometry. The complexity of these different optical factors dictates limits on radiometric observations with regard to **WCD** accuracy. Other factors associated to the radiometric quality are linked to the sensor radiometric performance such as the Signal to Noise Ratio (SNR) and optical distortions.

Geometric approaches

Recently, scientific interest has emerged towards application of photogrammetric methods such as **Structure from Motion (SfM)** and **Multi View Stereo (MVS)** to map coastal bathymetry. Unlike the radiometric estimation, photogrammetric methods estimate the seabed elevation with respect to the ellipsoid which corresponds to the **WCE** minus the **WCD** (see Figure 0.1). The **WCE** can be converted into **WCD** after subtracting the water surface elevation relative to the ellipsoid and correcting the refraction due to water. These methods do not explicitly account for the refraction of light rays which is induced by the air-water interface. Instead, the refraction bias is corrected based on ancillary knowledge of **Water Air Interface (WAI)**

height for deriving the **WCD**, or in-situ bathymetric data in order to directly obtain depths referenced with respect to the chart Datum. Geometric information also suffers from well-known sources of noise and systematic errors. In passive imaging in general, i.e. full-frame cameras or push-broom scanners, images are characterized by distortion effects that require geometric correction. Distortion in images may be attributed to the platform (i.e. variations in attitude, orbit and velocity), the sensor (i.e. calibration uncertainty), or the observed environment (i.e. earth rotation and curvature, local topographic effects, atmospheric refraction and map deformation) [9]. In order to improve the geometric accuracy of imagery, Ground Control Point (**GCP**) are often required for they can be used as measurement to calibrate the geometric model. These field measurements are often associated to deploying more resources, and specifically not conceivable in coastal areas [10].

WCD uncertainty

Uncertainty of **WCD** retrieved from passive imagery is required in order to inform end users with the derived product quality and its fitness-for-use. As an example, uncertainty is crucial for navigation safety and it is also required in statistical spatial data assimilation methods. In Hydrography, the **Combined Uncertainty and Bathymetric Estimator (CUBE)** is the widely adopted algorithm in which, uncertainty is used to guide the Hydrographer to filter and validate data in compliance with the **International Hydrographic Organization (IHO)** standards [11; 12].

Current research in passive imagery primarily focuses on enhancing the accuracy of **WCD** estimations, often sidelining the crucial aspect of uncertainty evaluation [7; 13]. While accuracy and precision are pivotal, they cannot be fully understood without a comprehensive grasp of the inherent uncertainty. Numerous studies strive to bolster **WCD** estimation capabilities and robustness, with precision assessment typically relying on the availability of reliable ground control points for field validation. However, when such verified data is inaccessible, the importance of accurately estimating uncertainty becomes paramount as the primary means to gauge the accuracy of **WCD** estimates.

It is within this framework that our research finds its significance, emphasizing the uncertainties associated with both radiometric and geometric approaches. The frequent omission of uncertainty analysis in geometric studies and its insufficient consideration in radiometric approaches contribute to a gap in scientific contributions, potentially explaining the slow integration of passive imagery into international standards compared to other surveying techniques. Our work aims to address this gap by conducting a detailed study of uncertainties, which are often relegated to a secondary concern following the correction of systematic errors. However, a rigorous uncertainty evaluation is essential for a complete understanding of the accuracy and precision of spectral imagery products, necessitating joint expertise in the

radiometric and geometric aspects of measurement.

Research question

Despite notable progress in radiometric and geometric methodologies for assessing WCD, integrating these techniques remains a complex challenge that is yet to be fully overcome. Radiometric methods are particularly susceptible to environmental variables and typically exhibit reduced effectiveness in optically complex waters and diverse scenes. Conversely, geometric approaches struggle in the absence of distinct features within images and often default to approximate models, which lack the precision of rigorous modeling that necessitates a thorough understanding of sensor optical properties.

Passive imagery is increasingly recognized as a promising tool for mapping coastal WCD. However, this potential is curtailed by significant limitations inherent to the prevailing radiometric and geometric methods. Notably, a substantial gap exists in the form of deficient uncertainty evaluation methods, which hinders the ability to confidently quantify the WCD and its associated accuracy. This deficiency underscores the central challenge confronting our research: How can we derive WCD and its associated uncertainty from remote sensing imagery (whether satellite or airborne, hyperspectral or multispectral), and overcome the constraints of current methodologies?

Research hypothesis and objective

Our inquiry into WCD from spectral imagery address the meticulous evaluation of uncertainty, acknowledging that such assessment is pivotal to the integrity of depth estimation and integral to the comprehensive process of inference, a central theme of this research.

The estimation of WCD from spectral imagery hinges on the precision with which uncertainties are quantified and managed. Radiometric and geometric approaches, each come with an array of uncertainties that are often addressed in isolation, leading to disjointed and potentially suboptimal WCD estimates.

The diagram in Figure 0.2 illustrates the complexities of error sources in the process of WCD inference. It exposes a clear division between the inner workings of model biases (central blue blocks) and the external noise factors (outer green blocks). The blue blocks represent the systemic biases inherent in the radiometric and geometric models, such as atmospheric conditions and sensor inaccuracies, which can be corrected through calibration processes. In contrast, the green blocks encompass noise factors that arise from the stochastic nature of environmental and sensor variables, often left unaccounted for in conventional modeling.

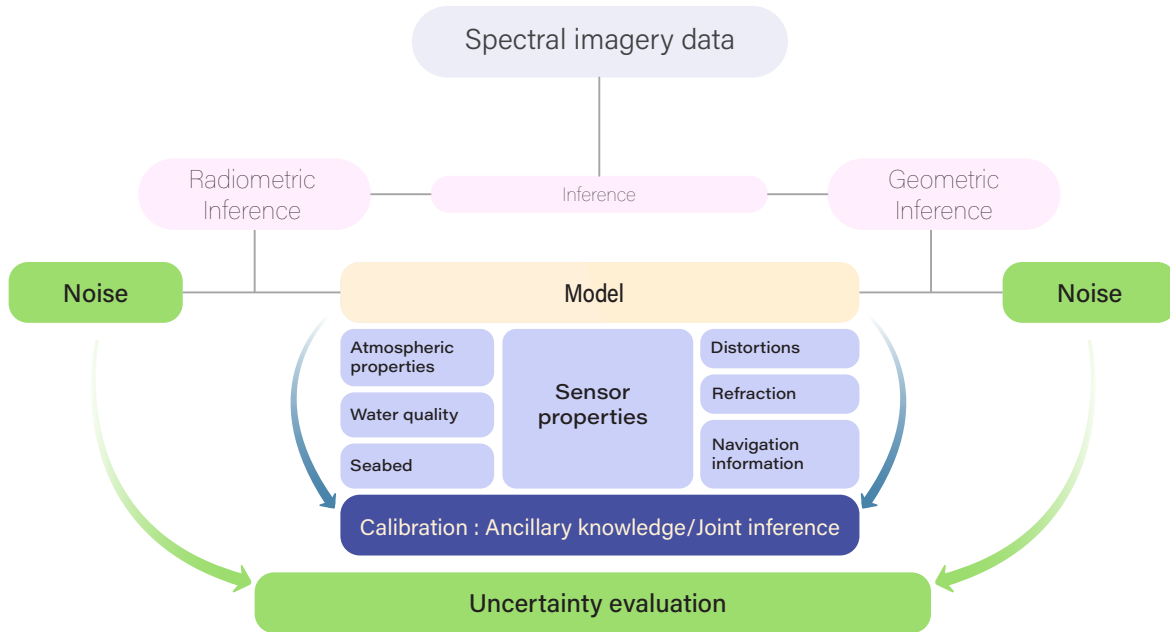


Figure 0.2 – Inference scheme in spectral imagery in radiometric and geometric approaches

Inference, in this context, is the process by which we deduce the **WCD** and its associated uncertainties from the spectral data. It involves not only the estimation of the depth itself but also a comprehensive accounting for the confidence in these estimates. A valid inference amounts to express the uncertainty surrounding the **WCD** estimates accurately.

We hypothesize that a unified, likelihood-based inference framework can systematically synergize the radiometric and geometric analysis of spectral images, thus enriching the estimation process of **WCD**. This integrated framework is poised to offer a novel pathway to handle uncertainties, by addressing the various error sources not as separate entities but as interconnected components of a single, cohesive system.

Research Hypothesis

The deployment of likelihood-based inference framework is anticipated to establish a unified methodology for the quantification of uncertainties in Water Column Depth (WCD) estimates derived from spectral imagery. This methodology constructed on the foundations of this framework will be applicable in both radiometric and geometric analysis, aiming to provide a comprehensive model for uncertainty evaluation and enhance the credibility of WCD assessments.

Building upon our research hypothesis, the overarching aim of this study is to devise a statistical inference-based methodology that synergizes radiometric and geometric information for **WCD**. This proposed methodology seeks to offer a comprehensive approach to quantify uncertainties in **WCD** estimations from spectral imagery, enhancing the ability to qualify spectral imagery derived bathymetric products.

In pursuit of this aim, our specific objectives are twofold:

1. Design a geometric inferential approach adapted to stereo-photogrammetric triangulation, allowing for the evaluation of **WCD** uncertainties within the likelihood framework.
2. Design a radiometric inferential approach that utilizes **Radiative Transfer (RT)** modeling, including **Semi-Analytical (SA)** models, to facilitate the assessment of **WCD** uncertainties through the likelihood framework.

By reaching these objectives, the study will help improving the integration of radiometric and geometric data, leading to a more reliable and comprehensive methodology for **WCD** estimation. This integrated approach is anticipated to advance the field of marine and coastal geospatial analysis significantly.

Methodology

The methodology hinges on the adoption of a likelihood-based inference framework to quantify uncertainties in radiometric and geometric analysis of spectral images. Its aim is to fuse the stochastic and systematic uncertainties under a unified inferential approach, as posited in our research hypothesis. The inferential process should be meticulously designed to accommodate the non-linear and complex interactions inherent in the spectral data and the underlying environmental processes. Herein, we focus on advanced statistical techniques, providing explicit modeling of the data generating process including **WCD** influence on data as well as sources of uncertainties in the data, which are pivotal for quantifying the reliability of **WCD** estimates.

Figure 0.3 presents the inferential framework adopted for this analysis, combining radiometric and geometric insights. The blue blocks encapsulate the predictive model components and the green blocks represent the stochastic noise elements.

Radiometric Analysis: Our approach is grounded in existing radiometric modeling techniques, focusing on spectral inversion processes, underscored by simulations based on Lee’s model [14] and incorporating multivariate Gaussian errors for noise modeling such as in [15]. The complexity of interactions between light and water necessitates moving beyond first-order inference methods. We explore profile likelihood adjustments to address the non-linearities inherent in **SA** models, as a promising perspective to enhance the precision of uncertainty quantification in radiometric **WCD** estimates.

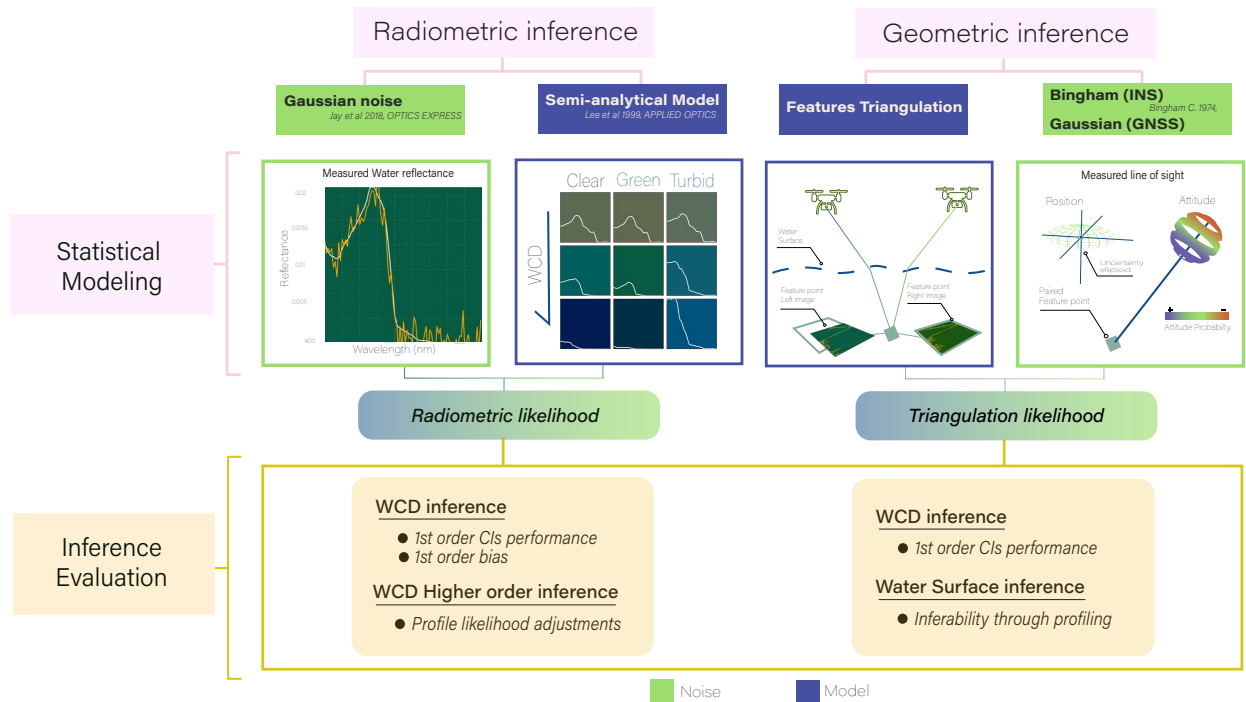


Figure 0.3 – Illustrative methodology for radiometric and geometric inference, highlighting the interplay between model components (blue blocks) and noise elements (green blocks), with profile likelihood and confidence intervals (CI) as cornerstones for uncertainty evaluation.

Geometric Analysis: For geometric statistical modeling, we introduce a novel approach for through-water photogrammetry triangulation, tailored for estimating **WCD** from noisy sensor pose observations. Unlike radiometric analysis, geometric analysis generally finds first-order inference methods sufficient, relying on variance-covariance propagation to effectively balance model components and noise elements.

In both analyses, profile likelihood and its associated statistical tests are pivotal for assessing **WCD** uncertainty, aligning with our hypothesis that a unified likelihood-based approach can enhance **WCD** estimation from spectral imagery.

Overall, our methodology underscores the critical role of profile likelihood and its extensions in both radiometric and geometric analyses, demonstrating its effectiveness in enhancing our understanding and quantification of **WCD** uncertainties from spectral imagery.

The methodological pivot away from empirical data towards simulation and modeling is a strategic choice, affirming that true insights often require a controlled exploration of theoretical constructs. In such a controlled environment, the interplay between model elements (blue blocks) and uncertainties (green blocks) can be dissected and understood without the confounding variables inherent in empirical data. This approach ensures that the inferences drawn are not muddled by unaccounted-for complexities, allowing

for a clear delineation of the model’s capabilities and limitations. The pursuit of higher-order inference in the radiometric analysis is a testament to the necessity of a controlled environment. Taking into account the complexities of interactions between light and water in coastal waters, first-order asymptotic descriptors for uncertainty may fall short.

Thesis Outline

After this introduction dedicated to the context, the motivation of the research, and the objectives of the thesis, the rest of the manuscript is structured as follows:

- **Chapter 1: Spectral Imagery analysis in coastal monitoring** - This chapter methodically examines spectral imagery analysis in coastal monitoring. Focusing on **WCD**, it explores various sensor technologies as well as the diversity of radiometric and geometric estimations methods.
- **Chapter 2: Statistical Inference for Uncertainties in Environmental Parameters Analysis** - This chapter lays the groundwork with theoretical concepts and constructs, establishing the context for the upcoming chapters on **WCD** radiometric and geometric uncertainties.
- **Chapter 3: A Likelihood-based Triangulation Method for Uncertainties in Through-Water Depth Mapping** - Exploring the precision of **WCD** estimates from airborne imagery, this chapter introduces a novel likelihood-based approach for through-water photogrammetry. It underscores the importance of accurately quantifying uncertainties, particularly those arising from sensor pose, and demonstrates the effectiveness of the likelihood ratio statistic under challenging conditions.
- **Chapter 4: Likelihood based inference for bathymetric uncertainties in semi-analytical models** This chapter delves into the complexities of radiometric **WCD** inference in Semi-Analytical models. It critically examines the limitations of first-order inference and paves the way for more sophisticated approaches. By introducing profile likelihood adjustments, it offers insights into robust uncertainty evaluation, particularly in scenarios where traditional methods fall short.
- **Conclusion and Perspectives** - This chapter synthesizes the research insights, evaluating the hypothesis against the findings and discussing the practical implications for coastal monitoring and hydrography. It also acknowledges the study’s limitations and outlines avenues for future work, emphasizing the potential of the likelihood-based framework to enhance **WCD** estimation from spectral imagery and support sustainable marine management.

Collectively, the chapters encapsulate a dual-faceted approach, synergizing the empirical precision of geometric methods with the analytical strengths of radiometric models. This unified

approach aligns with the hypothesis that leveraging a likelihood-based inferential framework enhances our understanding of **WCD** uncertainties in spectral products as well as the ability to quantify them accurately.

Chapter 1

Spectral Imagery Analysis in Coastal Monitoring

In this chapter, we delve into the complex domain of spectral imagery analysis for coastal monitoring, with a specific focus on WCD estimation. Building upon the foundational understanding of the solar spectrum’s interaction with Earth’s atmosphere, we explore the multifaceted nature of spectral data. This exploration encompasses the analysis of spectral resolution categories (HS and MS), sensor array types, and varying data acquisition platforms. We then transition to a comparative analysis of both radiometric and geometric approaches for WCD estimation. This analysis underscores the distinctive methodologies encompassing empirical models and RT methods, as well as addressing the unique challenges posed by multiview 3D reconstruction methods in coastal terrains. By providing a detailed overview of these diverse aspects, the chapter aims to present a general picture of the current technological advancements and the challenges inherent in spectral imagery analysis within the context of coastal environmental monitoring. This sets the stage for a deeper understanding of how these technologies and methodologies can be harnessed for effective uncertainties management in coastal monitoring.

1 Spectral imagery characteristics

Before we dive into the nuanced analysis of spectral imagery, it’s essential to start at the very beginning with the sun—our primary natural source of illumination. The sun bathes our planet in light, spanning a spectrum that includes Ultra Violet (UV), visible, and IR wavelengths. Understanding solar spectral irradiance, which measures the sun’s power over these various wavelengths, and its counterpart at sea level, is fundamental for interpreting how we perceive and measure our environment. These concepts are not just academic; they have real-world implications for how we capture and analyze data about our coastal waters,

particularly when estimating WCD.

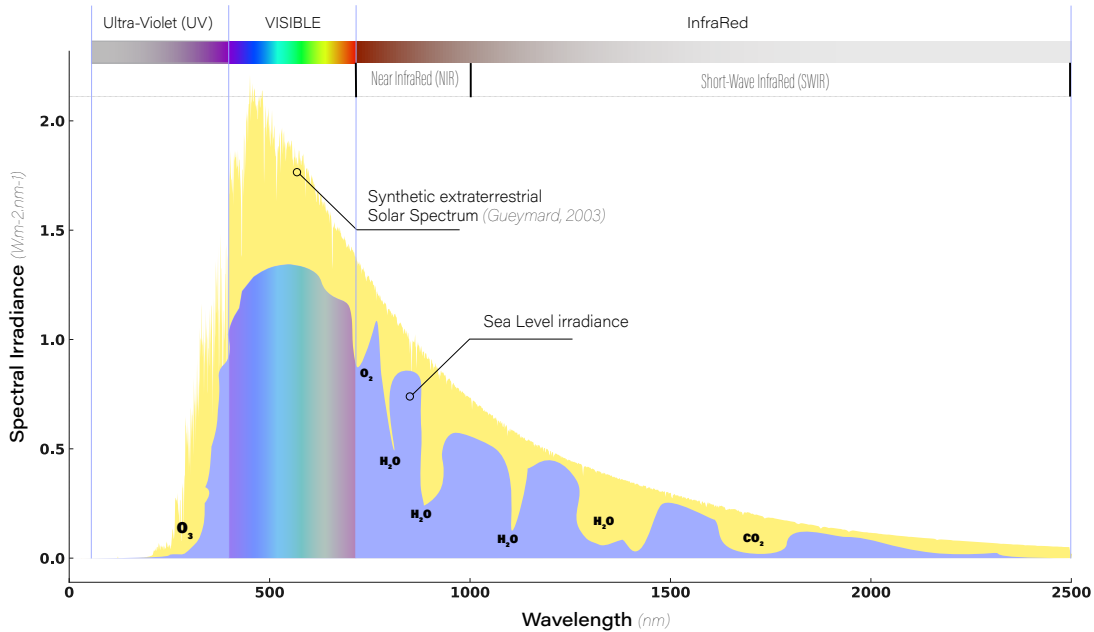


Figure 1.1 – The solar spectrum showcasing the difference between the synthetic extraterrestrial solar spectrum (yellow) and the sea level solar irradiance (melrose), with absorption bands due to atmospheric gases such as O_3 , O_2 , H_2O , and CO_2 .

The figure 1.1 serve as visual anchors for these concepts, illustrating the solar spectrum’s journey from extraterrestrial origins to its interaction with Earth’s atmosphere, which filters and modulates this spectrum in complex ways. For instance, the visible spectrum is critically important for radiometric and geometric analyses in coastal water radiative transfer, providing us with a vivid example of how irradiance is not just absorbed but also reflected by different materials.

Focusing on spectral imagery as primary data for environmental parameters inference, its characteristics significantly varies based on the sensing platform, sensor type as well as the environmental factors such as those associated with coastal shallow waters in our research. This section elaborates an overview of spectral data characteristics, emphasizing the nature of the information we anticipate encountering in radiometric and geometric analyses for WCD inference in coastal shallow waters.

The efficacy of passive remote sensing, particularly in coastal domain applications, is heavily influenced by its spatial, spectral, radiometric, and temporal resolutions. Spatial resolution, which is the pixel size of the imagery, is critical for detailed observations. Spectral resolution refers to the ability of a sensor to define wavelength intervals in frequency bands, crucial for distinguishing different materials or features. Radiometric resolution determines the sensor’s capability to differentiate between various intensities of radiation, which is vital for accurately

interpreting surface features. Temporal resolution, the frequency with which a satellite revisits the same location, affects the ability to monitor changes over time.

1.1 MS and HS resolutions

As irradiance from the sun strikes the Earth's surface, it interacts with various elements, giving rise to the spectral signature of the environment. Reflectance, a key quantity in this interaction, encapsulates the environmental optical properties and becomes encoded in the light that is reflected off objects. This reflected light carries the signature of the surface, which can vary significantly based on a multitude of factors, including but not limited to environmental conditions such as the angle of incidence, surface roughness, and inherent optical properties of the materials present.

This leads us to consider the observer or sensor itself. The human eye, for instance, interprets the light through a complex interplay of rods and cones, translating it into what we perceive as color and brightness. The Commission Internationale de l'Éclairage (CIE) color space, shown in the figure 1.2, is a quantification of the human visual response to different wavelengths, encapsulating the trichromatic nature of our vision. The figure 1.2 also offers an integrated view of spectral data analysis in environmental monitoring combining Sentinel 2 MultiSpectral Instrument (MSI) bands, hyperspectral Full Width at Half Maximum (FWHM) sampling, and the reflectance profiles of different environmental surfaces like snow, water, sand, and vegetation.

Sentinel 2 MSI represents the multispectral approach, capturing data in broad and disconnected wavelength bands to balance spatial and spectral details. Hyperspectral sensors, on the other hand, provide a more detailed wavelength sampling, capturing finer variations in surface reflectance. In the realm of optical remote sensing, multispectral sensors have been foundational, paving the way for various applications including ocean color studies and Satellite Derived Bathymetry (SDB). Sensors like Sentinel 2 and WorldView 2, typically with less than 20 wavelength bands, have been instrumental in broad applications ranging from crop mapping and land cover classification to chlorophyll mapping and SDB. These sensors often prioritize spatial resolution and optimal design targeting specific channels for resolving environmental features. This made them suitable for large-scale environmental monitoring despite their limited spectral resolution.

The advent of hyperspectral sensors marked a significant advancement in remote sensing capabilities. While hyperspectral sensors such as the Hyperion on Earth Observing-1 are less common in satellite imagery, they can provide fine spectral resolution in the range of 100-360 wavelength bands. This allows for the detection of minute variations in the electromagnetic spectrum, which is particularly beneficial in identifying specific chemicals, minerals, and de-

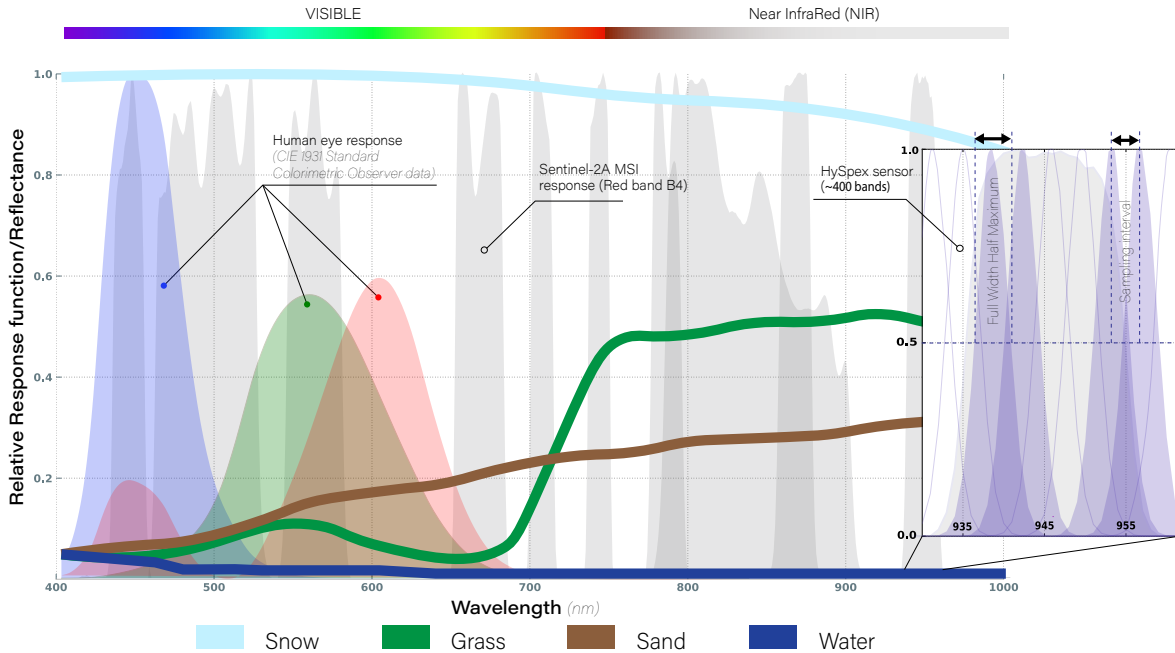


Figure 1.2 – This figure presents an overlay of spectral response functions and reflectance values across the visible to Near InfraRed (NIR) spectrum. It includes the human eye response (red-green-blue) based on the CIE 1931 Standard Colorimetric Observer data, Sentinel-2A MSI bands (grey), and the detailed hyperspectral sensor coverage with approximately 400 bands (melrose). Additionally, the figure illustrates typical reflectance signatures of common surfaces (snow, water, sand, and vegetation), extracted from [16] for a comparative analysis of natural features in remote sensing applications.

tailed vegetation characteristics. In coastal water analysis, hyperspectral sensors excel due to their ability to capture detailed spectral signatures, especially in the Visible Near InfraRed (VNIR) range. This makes them more adept for in-depth coastal studies, complementing the broader applications of multispectral sensors.

1.2 Sensor arrays

In passive optical sensing, we encounter various sensor array types, each with its unique mechanism of capturing light—from frame sensors that mimic the pinhole camera model to more advanced pushbroom sensors that scan the Earth line by line [17]. The sensing mechanism, along with the spectral resolution, dictates the fidelity and granularity of the data captured.

Frame sensors (e.g. CCD and CMOS arrays, Dove-R Dove-C CubeSats) capture a complete image in a single shot, making them ideal for detailed imagery of smaller areas, though they typically have lower spectral resolution. Pushbroom sensors (e.g. ESA’s Sentinel-2, MAXAR’s WorldView 2), with a linear array of detectors, capture the Earth’s surface strip by

strip, offering a balance between spatial and spectral resolution, thus well-suited for medium to large-scale mapping and environmental monitoring. Whisk broom sensors (e.g. NASA’s MODIS, Landsat 7), scanning line by line using a rotating mirror, provide high spectral resolution but also require more agility and are prone to failure in the long-term such as in the case of Landsat 7.

These sensor array types are employed in both multispectral and hyperspectral imaging, affecting their spatial and spectral resolutions. Sensor limitations such as noise and sensitivity issues can impact the quality of the data across all platforms, with varying degrees of influence based on the sensor technology. In the context of coastal monitoring, pushbroom sensors, have become the mainstay in satellite imagery due to their effective balance of resolution and coverage. However, the accelerated evolution in sensor technology, with developments in mixed sensors combining different types of sensors, or incorporating other technologies like LiDAR, is continuously reshaping the landscape of remote sensing. These advancements, while maintaining the core principles of optical sensing, are paving the way for more sophisticated environmental monitoring, potentially making current classifications and preferences in sensor types quickly outdated.

1.3 Acquisition Platform Classification

The range or altitude for vertical flights, at which surveying is conducted is a major factor in the final imagery characteristics. Optical remote sensing surveys can be classified based on the altitude of the data acquisition platform: satellite imagery from hundreds of kilometers above sea-level, medium-altitude data from drones or aircraft flying at altitudes from 100 meters to 2 kilometers, to close-altitude observations from boat-mounted or splash drones skimming the water’s surface.

Here, we classify surveying platforms based on the altitude at which spectral imagery is acquired as follows: high-altitude (satellite $\sim 400 - 800km$), medium-altitude (airborne $\sim 1 - 2km$ and drone $\sim 100m$), and close-altitude (below 5 meters altitude). Each platform has its unique attributes which shape the geometric, spectral, radiometric, and temporal qualities of the data they acquire.

Satellite imagery characteristics For coastal domain applications, where dynamic processes require frequent and detailed observations, the choice of the satellite and its corresponding orbit is critical. Table 1.1 provides an overview of various satellite classes, their typical altitudes, and resolutions pertinent to coastal remote sensing. Lower earth orbit satellites, such as those in polar and sun-synchronous orbits, are particularly relevant due to their ability to provide high-resolution data with relatively frequent revisit times. The atmospheric content, including aerosols, water vapor, and cloud cover, significantly impacts the quality

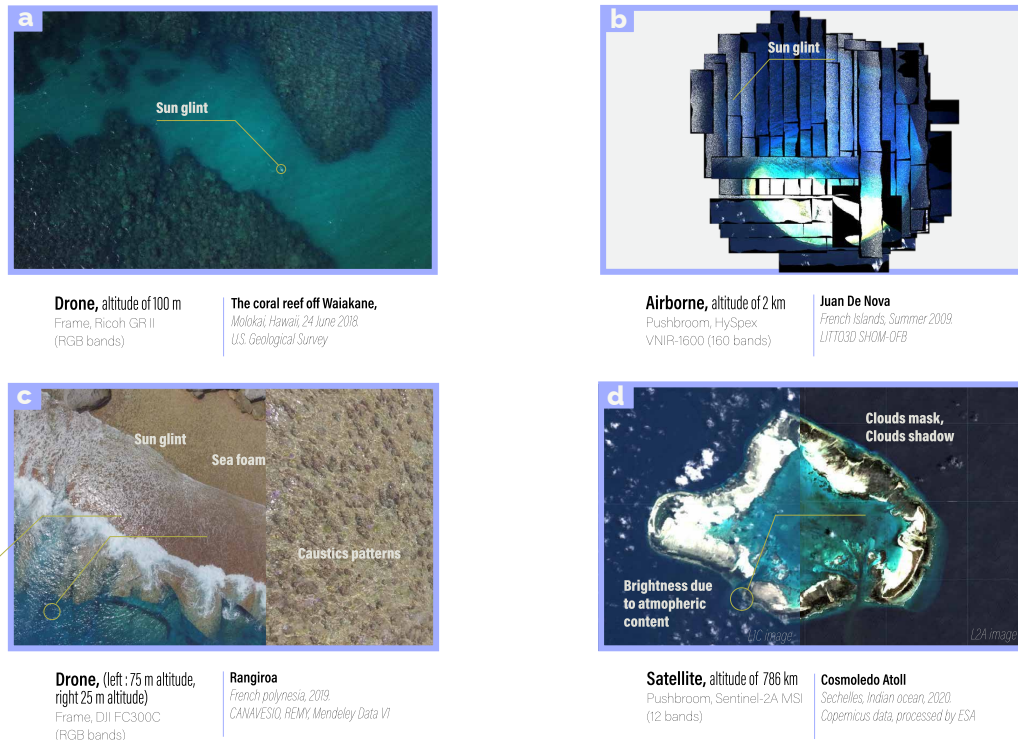


Figure 1.3 – A comparative display of remote sensing images from varying altitudes and platforms. **a:** Drone image at 100m altitude showing sun glint on the water near the coral reef off Waikane, Molokai, Hawaii. **b:** Airborne image at 2km altitude over Juan De Nova, French Islands, with visible sun glint and cloud shadows. **c:** A closer view from a drone at a variable altitude capturing sun glint, sea foam, and caustics patterns near Rangiroa, French Polynesia. **d:** Satellite image from Sentinel-2A MSI at 786km altitude over Cosmoledo Atoll, Seychelles, showing brightness variations due to atmospheric content and clouds.

of satellite imagery. Cloud cover, in particular, is a major concern as it can lead to data loss or reduced quality in coastal regions. To address these challenges, rigorous georeferencing, radiometric, and atmospheric corrections are often essential to ensure the accuracy and reliability of satellite data.

Medium-altitude imagery characteristics Airborne sensors such as drones and airplanes provide a more flexible and controlled approach to data acquisition compared to satellites. In particular, aerial drones offer highly detailed data capture capability allowing to map the spatial heterogeneity, structural complexity, and temporally dynamic nature of coasts [18]. However, their spatial and temporal scalability is lower due to higher operational costs and limited flight endurance, and they are also sensitive to weather conditions, including rain, wind, and cloud cover. The image quality from drones can be influenced by factors like platform stability and altitude, with higher altitudes increasing the atmospheric content in images, which may obscure data from water columns. Additionally, drones are less impacted

Class	Configuration						
	satellite	type	spatial resolution (m)	number of bands	Altitude (km)	frequency (days)	stereo products
Low Earth Orbit (LEO)	Landsat 7	W	15-30	8	705	16	No
	Landsat 8	P	15-100	11	705	16	No
	Sentinel-2	P	10-60	13	786	5	No
	WorldView-2	P	0.46	8	617	1-3	Yes
	WorldView-3	P	0.31	29	617	1-3	Yes
	Pleiades	P	0.5	5	694	1	Yes
	QuickBird	P	0.6	4	450	1-3.5	Yes
	Hyperion	P	30	220	705	16	No
	Polar Orbit	MODIS(Terra)	W	250-1000	36	705	1-2
MODIS(Aqua)		W	250-1000	36	705	1-2	No
Sun Synchronous Orbit (SSO)	NOAA-20(JPSS-1)	W	375	22	824	1	No
CubeSats	PlanetScope (Doves)	F	3-5	4-8	400-500	1	No

Table 1.1 – Satellite Platforms for Coastal Monitoring: The table summarizes key satellites, their resolutions, band counts, altitudes, and stereo-imaging capabilities. "P", "W" and "F" refer to pushbroom, whiskbroom and frame sensors, respectively.

by high-altitude atmospheric elements like aerosols and water vapor compared to satellites, but they still face challenges related to local weather conditions and visibility.

Close-Altitude Imagery characteristics Close-Altitude coastal waters imagery, using platforms like low-altitude drones flights [19], boat mounted cameras [20] and splash drones, provides a unique perspective for a detailed mapping of coastal and marine waters. These methods are particularly useful for acquiring high-resolution imagery in areas that are challenging for satellites and conventional airborne imagery, such as shallow waters, nearshore environments, and complex coastal terrains. Boat-mounted cameras can offer high-resolution images which can be ideal for detailed studies of coastal features and marine life. Splash drones, designed to operate in marine environments, can capture both aerial and water-level imagery, providing valuable data for bathymetric surveys and habitat mapping providing a detailed monitoring of coral reefs. However, these close-altitude surveys are limited in their coverage area and are impacted by local water and weather conditions, requiring careful planning and execution to gather quality data.

These different spectral imagery altitudes exhibit distinct radiometric and geometric characteristics, having an influence on their analysis and application as illustrated in Figure 1.3. While satellite data is characterized by comprehensive coverage and consistent radiometric and geometric processing and validation standards, such as those seen in Sentinel-2 level products, medium and close-altitude data offers more detailed local coverage but with different characteristics based on the equipment and environmental factors. The choice between these platforms depends on the scale of the area to be monitored, the level of detail required, and the specific environmental conditions of the area. In satellite imagery, the adjacency effect, where the signal in a pixel is contaminated by radiation scattered from neighboring pixels, can be significant, especially for large area coverage. Sun glint, a common issue in satellite and drone imagery, appears as homogenous bright patches caused by sunlight reflecting off the water surface [21]. Its impact can be minimized, with more control in airborne imagery by adjusting the flight direction relative to the sun and is less pronounced in close-altitude imagery due to the proximity and angle of capture. However, medium and close altitude imagery can exhibit second-order effects of sun glint, such as noisy patterns resulting from wave surface fluctuations [22] (See Figure 1.3). Close-altitude imaging can encounter optical caustics (refraction patterns of bright and dark regions) and sea foam either contaminating or obscuring water column reflectance [23]. These surface effects can obscure the underlying features and are a unique challenge for coastal water imaging.

2 Radiometric WCD estimation

This section focuses on the estimation of WCD in coastal areas. It compares different methods used in this field, mainly the empirical models and RT approaches. Empirical approaches are straightforward and rely on existing data correlations, while RT approaches involve detailed simulations of light interaction with water [5]. Each approach has its unique strengths enhancing our understanding of the complexities of spectral imagery analysis in coastal environments.

2.1 Empirical approaches

Empirical approaches for shallow water WCD estimation use various models, from linear regressions to advanced machine learning algorithms. The principle is to establish a relationship $z = f(\mathbf{y})$, where z is the estimated WCD, and \mathbf{y} represents radiance data or reflectance measurements from remote sensing imagery.

- **Linear and Advanced Regression Models:** These models, exemplified by [6] and [24], use linear regression techniques to correlate reflectance data with water depth. For example, Stumpf’s two-band ratio model considers bottom albedo variability for improved performance in diverse coastal environments.
- **Machine Learning Algorithms:** Recent developments include machine learning models like support machine vectors [25; 26], random forests [27] and deep neural networks [28; 29], offering nuanced depth estimations. These models are also calibrated using ground truth data from acoustic or LiDAR soundings.

Empirical approaches are computationally efficient and easily deployable, especially for large datasets. However, they require current in-situ depth measurements which can be expensive and are site-specific, limiting their transferability across different locations and times.

2.2 Radiative transfer approaches

RT approaches focus on physically modeling light’s RT through the water column, modeling sea surface reflectance based on environmental conditions. Mainly, the physics of RT within the water column depends on its constituent such as phytoplankton pigments, Color Dissolved Organic Matter (CDOM), and Suspended Particulate Matter (SPM) as illustrated in Figure 1.4.

- **Look-Up Table (LUT) Methods:** These methods involve forward modeling of the Radiative Transfer Equation (RTE), using tools like Hydrolight. The LUT is populated

with reflectances for various environmental parameter combinations, and a similarity criterion is used to find the best match [30; 31]. LUT are computationally efficient for real-time applications once they are generated, but can be limited by their predefined parameter spaces and discrete mappings. Also the inversion process often ensures some form of enforced one-to-one mapping which may lead to misleading conclusions on model’s reliability.

- **SA Models:** These models approximate the RTE with non-linear equations. They consider a handful of parameters related to water constituents absorption and scattering, bottom reflectivity, and depth. The models decompose underwater remote sensing reflectance and bottom contributions and are often optimized using iterative algorithms like Levenberg-Marquardt [32; 15]. Such iterative optimization methods are flexible and can capture complex relationships, but while generally fast, they risk converging to local minima especially in shallow waters SA models.

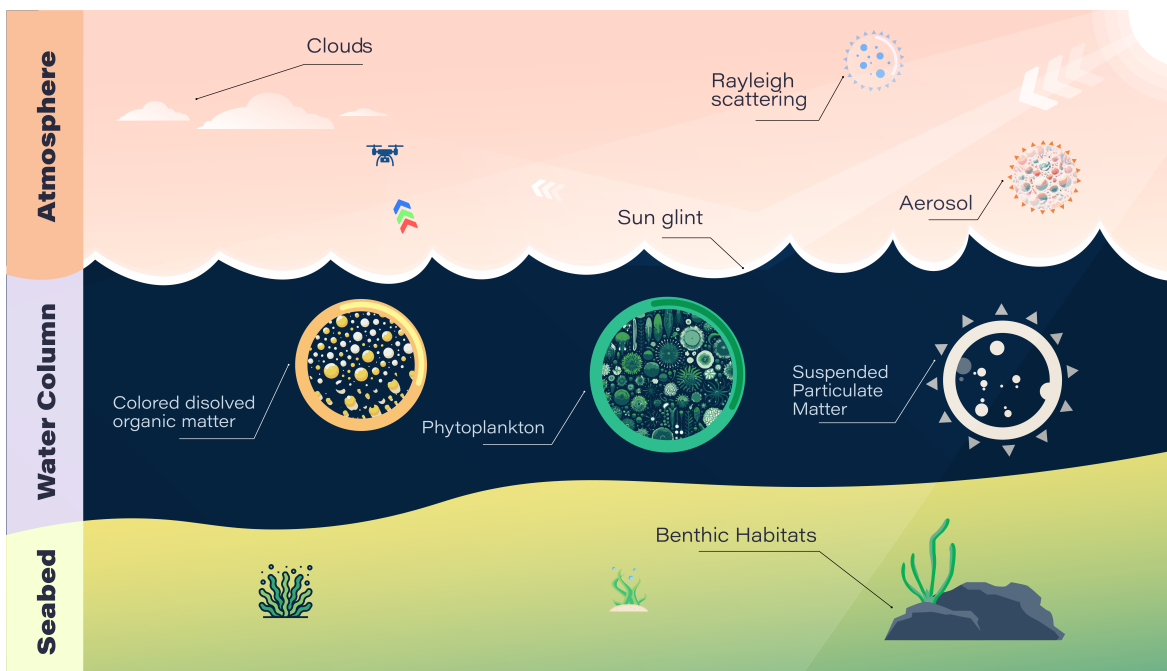


Figure 1.4 – Generic view of different factors of light radiative transfer in coastal waters remote sensing

Beyond the diversity of RT approaches, they are essentially driven by forward modeling and employ numerical inversion techniques to directly solve the RTE approximations. In the realm of RT approaches, the pursuit of precision extends beyond the physical modeling of light’s interaction with the water column. It delves into the quantification of these interactions through meticulous radiometric data calibration and the estimation of Remote Sensing Reflectance (R_{rs}). These quantitative aspects form the cornerstone of RT modeling, allowing for a more accurate interpretation of water column properties.

2.3 Calibration and Atmospheric Correction in RT approaches

The process of accurate RT modeling is twofold. First, it begins with the radiometric data calibration, ensuring that the raw sensor measurements are transformed into a reliable representation of at-sensor radiance. This step is fundamental in correcting any discrepancies caused by sensor anomalies or atmospheric interferences. The calibrated data thus becomes a refined input, primed for subsequent analytical processes.

Second, the focus shifts to the critical estimation of R_{rs} , a quantity that isolates the water column’s optical properties signal from other factors such as atmospheric content and sun glint. This step is essential in RT approaches, as it filters out confounding factors, rendering a clear view of the underwater environment. The accuracy of R_{rs} estimation is heavily influenced by the sensor’s spectral characteristics and the effectiveness of atmospheric correction methods. Together, these quantitative aspects lay the groundwork for a comprehensive and accurate understanding of the aquatic environment through RT modeling.

Radiometric data calibration Radiometric calibration in remote sensing involves establishing correct radiometric models, which include various components such as the linear relationship between the Digital Numbers (DN) and radiance, response functions, integration time sensitivity, and other sensor-specific characteristics. This comprehensive process ensures that the sensor’s output is an accurate and reliable representation of the observed radiance.

Two principal methods are employed for the radiometric calibration of spectral imagers: laboratory calibration [33; 34; 35] and vicarious calibration (i.e. based on ground-based measurements of surface reflectance) [36; 37; 38; 39]. Laboratory calibration, conducted under controlled conditions, is fundamental for initial sensor calibration, setting a baseline for accuracy. However, it might not fully capture operational variables like temperature changes and atmospheric disturbances [39]. Vicarious calibration, on the other hand, involves using ground truth reflectance from known, stable sites to validate and adjust the sensor’s performance in real-world conditions. While effective, its accuracy can be influenced by environmental factors, making it less efficient in dynamically changing environments such as coastal regions [37]. Moreover, in-orbit or in-flight calibration, typical in scientific satellites like Sentinel-2 and MODIS, combines onboard laboratory-grade checks with vicarious adjustments, offering continuous calibration throughout the mission [40; 41].

The sensor type significantly impacts the calibration process, with each sensor presenting distinct challenges. Whiskbroom sensors, adopted in earlier Landsat missions, have a single detector scanning the Earth’s surface line by line, simplifying their calibration which is usually achieved through a combination of laboratory methods and periodic field checks [42]. Pushbroom sensors, central to contemporary hyperspectral and multispectral systems, have

high pixel density and multiple spectral channels, necessitating a more elaborate calibration regime. This involves both pre-flight laboratory calibration for baseline establishment and on-going vicarious calibrations to accommodate in-flight variations and environmental impacts. Calibration of these sensors requires meticulous and joint attention to geometric, radiometric and spectral characteristics in order to maintain consistent data quality across the sensor’s Field Of View (FoV). Frame sensors, often found in commercial cameras repurposed for scientific use, face unique calibration challenges. Capturing entire scenes in one go, these sensors can exhibit spatial non-uniformities (vignetting effect) and varying sensitivity across the array. Their calibration thus includes laboratory methods to define initial radiometric properties and field-based adjustments to address spatial discrepancies and accurately represent the sensor’s dynamic range [39].

In summary, radiometric calibration is a vital component in achieving reliable and accurate spectral data, especially in scientific research and coastal environmental monitoring. The calibration strategy must be tailored to the sensor’s design, data acquisition methodology, and the specific demands of the remote sensing application to ensure data integrity and applicability.

Remote Sensing Reflectance Following the rigorous process of radiometric data calibration, the focus shifts towards the crucial aspect of Remote Sensing Reflectance (R_{rs}), a key quantity in coastal remote sensing. This transition underscores the importance of isolating water column optical properties for accurate WCD estimation. As we delve into R_{rs} , we encounter the challenges of Atmospheric Correction (AC) and sun glint removal, both integral to refining the quality of data obtained from various spectral sensors and platforms.

AC is essential in transforming at-sensor radiance into meaningful geophysical information by removing atmospheric influences. The effectiveness of AC is particularly influenced by the sensor’s spectral and radiometric properties, as detailed earlier in the chapter. High-altitude platforms like satellites require more complex AC due to their extended atmospheric path [43; 44], whereas lower-altitude platforms like drones encounter relatively weaker atmospheric signal. Similarly, the spectral resolution of the sensor plays a crucial role in distinguishing and correcting atmospheric effects [43; 44]. Also, incorporating an analysis of aerosol properties in the littoral zone is pivotal, as these particles significantly influence atmospheric correction accuracy by altering light scattering and absorption dynamics. This consideration is essential for refining R_{rs} measurements and, by extension, coastal water column depth estimations.

Sun glint, the specular reflection of sun light off the water surface, presents a unique challenge, especially evident in imagery from medium and high-altitude platforms. Its impact varies based on the sensor’s spatial resolution and the platform’s viewing geometry [8; 22]. High-resolution sensors and oblique viewing angles can amplify sun glint effects, necessitating

sophisticated correction algorithms [8; 22]. These algorithms, tailored to the sensor type and platform altitude, aim to mitigate sun glint to reliably extract R_{rs} , a pivotal metric that embodies the interaction of sunlight with the water column [45; 43].

While the focus of RT approaches is primarily on quantitative analysis, it is noteworthy that the high-quality data obtained through these methods can be beneficial for empirical modeling as well. Empirical models, traditionally reliant on more direct radiance measurements, could potentially leverage the refined outputs of R_{rs} and calibrated radiance for more accurate WCD estimations. However, it is crucial to consider the inherent challenges in this integration. The accuracy and applicability of R_{rs} within empirical models are dependent on the precision of atmospheric correction algorithms, which may vary in different coastal settings and under varying environmental conditions. This variability introduces a degree of uncertainty and necessitates a cautious approach. By acknowledging these constraints, researchers can explore the synergistic potential of quantitative RT data in enhancing empirical models, while remaining vigilant about the limitations and context-specific applicability.

3 Geometric WCD estimation

This section focuses on the geometric estimation methods of the WCD in through water environments focusing on coastal areas. Geometric estimation is particularly advantageous in shallow waters with sufficient texture for pairing overlapping images features, providing an additional avenue for bathymetric mapping in coastal waters. Similar to the land context, the analysis begins with feature detection and matching across images, establishing homologous points and using their coordinates for 3D triangulation. However, it presents unique challenges due to the interaction of light with the air-water boundary. This interaction results in refraction, which causes systematic bias in depth estimation, making the water column appear shallower [46; 47; 48]. This issue is exacerbated in dynamic coastal environments and low altitude imagery, where water surface disturbances, time-lag effects in imaging water surface features [49], and caustics [23] further complicate the analysis. In the forthcoming sections, we will first approach the terrestrial context to present the traditional geometric estimation methods. This initial discussion will lay the groundwork for understanding the standard processes involved in 3D space reconstruction using overlapping images in land-based scenarios. Following this, we will pivot to the methods specifically adapted for through water contexts, with a focus on coastal areas. Here, we will highlight the key differences and challenges that distinguish the aquatic environment from terrestrial settings.

3.1 3D reconstruction in land photogrammetry

In the field of photogrammetry, various methodologies are employed to achieve 3D reconstruction, each offering unique capabilities and applications. Mainly, 3D reconstruction can be achieved either via rigorous approaches based on MVS and SfM pipelines or approximate modeling on the basis of Rational Polynomial Functions (RPF). This multi-view framework brings its strengths to the table, catering to a wide array of applications from detailed archaeological documentation to dynamic urban mapping.

Rigorous methods SfM-MVS fundamentally leverage the same mathematical principles of collinearity and intersection for determining the 3D coordinates of points in the scene. The collinearity principle simply states that the sensor optical center, the image pixel coordinates and the object coordinates lie on the same line. The intersection principle states that the homologous rays incident on the camera’s focal plane intersect at the matched feature point. The collinearity equations establish a relationship between the object point coordinates \mathbf{x}_f , and the image coordinates \mathbf{x}_p as follows:

$$\mathbf{x}_p = f(\mathbf{x}_f, \boldsymbol{\theta}_{eo}, \boldsymbol{\theta}_{io}) \quad (1.1)$$

where f represents the functional form of these equations and the objective is to minimize the error between the observed and the modeled image coordinates. $\boldsymbol{\theta}_{eo}$ and $\boldsymbol{\theta}_{io}$ represent the exterior and the interior orientation parameters, respectively. This model can be purposed for a variety of tasks including camera calibration, spatial intersection (i.e. triangulation of matched feature points) and spatial resection (i.e. estimation of camera position and orientation). It is important to note that this generalized representation of these equations is often formulated for pinhole model cameras. This hinders the ability to generalize the triangulation to more sophisticated camera models such as pushbroom sensors. While pushbroom sensors can be approximated as a linear pinhole cameras, this approximation may not be accurate for taking into account the pixel/band variability characterizing these sensors [34].

Approximate methods Rational Polynomial Coefficients (RPC) parametrize RPF, which offer a mathematical alternative to the collinearity equations by establishing a mapping between image and object coordinate spaces [9]. These RPC encapsulate essential parameters that represent both the camera’s interior orientation (like focal length and principal point coordinates) and its exterior orientation (including position and attitude), thereby enabling the conversion of image coordinates into real-world geographical locations without requiring a detailed sensor model or precise exterior orientation information. Commonly employed in pushbroom satellite imagery, these coefficients provided by manufacturers effectively replace

the need for a geometric model of the sensor, facilitating the processing and analysis of images from these platforms.

First-order **RPC** are structurally equivalent to collinearity equations and can yield similar performance [50]. However, **RPC** can suffer from issues such as overparameterization and singularities, which can lead to uncontrolled inaccuracies [9]. These problems are compounded by the fact that **RPC** are often derived from **GCP** that may not comprehensively cover the entire image area. **GCP** themselves carry their own uncertainties, contributing to the approximate nature of the **RPC**. These shortcomings can contribute to artificial local distortions in the **RPC** model. Therefore, while **RPC** provide a practical solution for transforming image coordinates to geographic coordinates, their reliance on polynomial approximations and **GCP** introduces a level of approximation that must be carefully managed, especially in precision-critical applications.

3.2 3D reconstruction in through water photogrammetry

In order to address the challenges of 3D reconstruction in coastal waters, several methods have been developed, mainly in order to accommodate the refraction geometric effect. There are two main factors to consider in the refraction effect: the refractive index ratio which dictates how the homologous rays are bent at the air-water boundary, and the normal axis to the water surface. The current extent in coastal applications in through water photogrammetry is the first factor assuming a flat water surface. The existing methods can be broadly classified into two categories: corrective and strict/ray tracing approaches. Corrective approaches aim to implicitly compensate for the refraction effect, while ray tracing approaches strictly model the trajectory of the homologous rays in the 3D space [51].

Corrective approaches Corrective approaches rely on adapting land photogrammetric techniques such as **SfM-MVS** and **RPC** approximate modeling to the through water context. In coastal water studies, **SfM-MVS** methods have been often applied in airborne studies [52; 53; 20] through collinearity based modeling, while **RPC** approximate modeling has been extensively employed in satellite bathymetric studies [48; 54; 55; 56].

Inherent biases in the **RPCs** can typically be corrected with additional **GCP** on land; however, in coastal water areas, the main bias arises from refraction at the water interface whereas collecting **GCP** in coastal areas can be cumbersome and unreliable [10]. Correcting this bias requires assumptions about the position of the water interface and an understanding of the refractive properties of water, adding another layer of complexity to the use of **RPC** in these environments. In **RPC** approaches, the refraction correction is often applied a posteriori to the derivation of a **Digital Surface Model (DSM)**. Different criteria led to diverse formulations of the refraction terms which can be applied on either **RPC** [48; 55]. The derivation of these

correction terms is usually based on Snell’s law of refraction, a constant refractive index and a flat water surface assumption. The correction is commonly applied on the apparent depths (i.e. **WCD** without compensation of the refraction) updated with a scaling factor in order to take into account the refraction effect.

In collinearity-based approaches (i.e. SfM-MVS), compensating the refraction effect has been addressed either in the image space [57; 19] or the object space [58; 47]. Arguably, the rationale for these methods is rooted in adapting the multi-media problem to fit the methodologies of existing one-medium (air) photogrammetry, encompassing both mathematical and computational aspects. [59] proposed a modification of the collinearity equations where a vertical scaling factor is to be determined for each homologous ray. It is known from the first analytical works on two-media photogrammetry [46] that the refraction can be compensated either by introducing radial shift terms on image coordinates or by adjusting the focal length. [57] proposed to resolve the refraction at the image level by adjusting the focal distance for each point based on prior estimations of the air-water ratio as developed in [19]. In corrective approaches, implicitly compensating for refraction renders the physical interpretability of the results more challenging as the refraction effect is not explicitly accounted for. Besides the assumption of a flat water surface, these methods are explicitly conceived for scenarios where the camera is vertically oriented to the surface [51; 60]. This suggests their sub-optimality when drone imagery, usually characterized by low stability, is being used to create a 3D model of the seabed.

Corrective approaches, while simple to implement, are subject to the flat **WAI** assumption and are limited by their reliance on ancillary knowledge of the **WAI** position or in-situ depth measurements.

Ray tracing approaches Ray tracing methods strictly model the geometric path of the homologous rays in the 3D space for an arbitrary number of parallel refractive interfaces [60; 61]. [60] demonstrated the ability of ray tracing methods to estimate exterior and interior orientation parameter, planar surfaces parameters and refractive indices simultaneously. This makes ray tracing methods advantageous for extracting more environmental information compared to the conventional methods. Ray tracing methods can be computationally demanding and they are less flexible to be adapted to the different optical sensor models. While the sensor interior orientation and its exterior orientation are explicitly modeled, the pinhole model is often a hard-coded assumption in these approaches. [51] have recently proposed a ray tracing method which provides the ability to decouple the interior orientation. This study showed that the corrective methods accuracy decreases in comparison to the ray tracing by about 10% in perfect vertical imaging conditions and by about 50 % in oblique imaging conditions (10 °). However, these findings are obtained in specific laboratory conditions and do not necessarily apply to coastal waters surveys.

All the previously discussed methods are developed under the flat interface assumption in order to enable analytical developments. This assumption can be valid for calm waters and high altitude imagery where the amplitude water surface fluctuations is negligible compared to the altitude of the sensor. In wavy scenarios, the distortions induced by water surface fluctuations will be absorbed in the reconstructed seabed model. [62] have analytically studied the impact of a sinusoidal wave field on the object coordinate, and emphasized that wave induced errors are more pronounced (1 m) for relatively deep waters (10 meters), high altitude airborne flights (1500 m) and non simultaneous imagery. [63] developed a probabilistic approach taking into account random refractive distortions in the through water 3D reconstruction. However, the development in this method is specific to still camera acquisition mode and does not address dynamic platforms for mapping coastal areas. Ray tracing methods, while diverging from traditional methods, can be easily narrowed further for the simpler through water problem with two-media. Their flexibility allow to include other sensor models beyond the central projection constraint in the pinhole model. Notably, the application of these strict modeling approaches is often validated in controlled experiments and has not been investigated for coastal imagery datasets in bathymetric studies, which consist essentially in approximate modeling and refraction compensation approaches.

Chapter conclusion

In conclusion, the field of shallow water **WCD** estimation is evolving rapidly with the integration of advanced technologies and methodologies. Advancements in sensor technology and algorithm development continue to open new possibilities for improving quality of optically-derived bathymetry in shallow waters. These innovations are not only refining existing models but are also paving the way for novel applications and methodologies in the field. As such, the future of shallow water **WCD** radiometric and geometric analysis appears to be geared towards more sophisticated, accurate, and versatile techniques, capable of addressing the complex and dynamic nature of coastal and inland water bodies.

This initial discussion sets the stage for understanding the inherent characteristics of spectral imagery data and their implications for **WCD** inference. These characteristics inform about the different challenges in environmental parameters analysis from spectral imagery, particularly the **WCD** in coastal shallow waters mapping. In addressing these challenges, advanced correction techniques and modeling approaches have been tailored for limiting uncertainties and ensuring better quality in coastal environments imagery.

However, more efforts are needed to converge to a unified approach for integrating these distinct methodologies to effectively handle the technological characteristics of the survey equipment (optical sensor, platform stability) and the dynamic nature of coastal waters,

ensuring a comprehensive management of coastal remote sensing environmental products such as the WCD uncertainties. Subsequently, we delve into the principles of statistical inference, focusing on how these data insights are transformed into a rigorous statistical framework. While this thesis does not directly analyze specific datasets to test our hypothesis, the chosen statistical modeling approach is designed to anticipate the type of data we expect to encounter, differentiating between the model and the noise processes inherent in the data. For a more detailed exploration of data challenges in both geometric and radiometric contexts, readers are encouraged to refer to the respective chapters 3 and 4.

Chapter 2

Statistical Inference for Uncertainties in Environmental Parameters Analysis

In this chapter, we delve into a nuanced exploration of the methodologies and theoretical concepts integral to uncertainty estimation in the context of environmental monitoring and remote sensing. To provide a cohesive and practice-focused narrative, we use **WCD** as a pivotal reference point, illustrating how data characteristics transition into robust statistical inferences and supporting the arguments for each uncertainty framework. This exposition is tailored to be a reference for researchers and practitioners seeking to apply statistical inference methods in their work, irrespective of the specific environmental parameter under study, such as **WCD** in our research.

The narrative transitions into a detailed exploration of various statistical frameworks, such as the variance-covariance framework and the likelihood-based inference framework, each contributing a unique lens through which uncertainties can be understood and quantified. While the variance-covariance framework for uncertainties can be independently addressed, we have intentionally formulated it under the lens of statistical inference. This approach is not only for coherence in mathematical notations but also to position it relative to other frameworks in terms of its implicit assumptions and practical extent, providing an understanding of its interplay with other inferential methods.

A significant focus of this chapter is dedicated to the concept of inference in the presence of nuisance parameters and profile likelihood-based inference, an extension of the likelihood framework which can benefit from recent advances in asymptotic theory [64; 65; 66]. This section aims to illuminate the nuances between interest and nuisance parameters, highlighting its relevance and applicability in various scenarios. The choice to weave the narrative around the central theme of **WCD** is intentional, designed to establish a natural and logical pathway to

this theoretical framework. Focusing the inference on a specific interest parameter effectively encapsulates many estimation challenges in remote sensing, including our research where **WCD** is the interest parameter.

Structured progressively through theoretical notions of statistical inference, this chapter is designed to establish a firm theoretical base that informs and enhances the application-specific discussions in the subsequent chapters. Its content is intended to resonate beyond the confines of **WCD** analysis, serving as a valuable resource for a broad spectrum of applications in remote sensing and environmental monitoring. While this thesis does not directly analyze specific datasets to test our hypothesis, the chosen statistical modeling approach is designed to anticipate the type of data we expect to encounter, differentiating between the model and the noise processes inherent in the data. For a more detailed exploration of data challenges in both geometric and radiometric contexts, readers are encouraged to refer to the respective chapters on 3 and 4.

1 Theoretical foundations

Statistical inference in remote sensing, particularly in radiative transfer and photogrammetry, often adopts parametric approaches, focusing on describing data through measurable or implicit parameters. However, it can also take non-parametric or semi-parametric forms, depending on the context and data characteristics [67; 68]. In the domain of radiative transfer modeling and photogrammetry, we primarily consider parametric approaches, aligning with the semi-analytical models in shallow waters for radiometric analysis [14] and rigorous modeling in geometric analyses [46; 59]. This approach enables a comprehensive understanding of radiometric and geometric data, facilitating the translation of these insights into quantifiable knowledge about certain parameters such as **WCD** in our research.

This translation is a core aspect of statistical inference, enabling the drawing of conclusions about unknown parameters from observed data. In this study, parameters $\boldsymbol{\theta}$ include **WCD** and other entities with physical interpretations, integral to semi-analytical models in radiometric analysis and rigorous modeling in geometric analysis. Considering a parametric approach for **WCD** inference, the main objective is to derive conclusions about the values of unknown parameters $\boldsymbol{\theta} = (\theta_1, \theta_2, \dots, \theta_p)$ of a model or measurement system, given observed data $\mathbf{y} = (y_1, y_2, \dots, y_n)$. After outlining the characteristics and challenges associated with the anticipated data in the previous chapter, it is insightful to acknowledge how the general scheme of statistical inference applies in **WCD** estimation.

Conducting statistical inference starts with defining the data generating process which mainly involves two key steps:

1. **Data Characterization:** We begin by characterizing the observed data \mathbf{y} from which WCD can be inferred. This step encompasses understanding the data’s generating process, quality, and potential sources of error. In radiometric inference, these data can be the end-products of R_{rs} or Top Of Atmosphere (TOA) reflectance. In geometric inference, considerations may include the sensor’s attitude (exterior orientation) or the supplied RPC.
2. **Model Specification:** This involves defining the statistical model parameters θ , which represent aspects of a statistical distribution, often designated to describe the mean of the statistical model such as the combination of WCD, water Inherent Optical Properties (IOP), and seabed properties for describing the R_{rs} in SA approaches¹. Formally, this denotes that the random variable Y follows a probability distribution P , which is parameterized by the model parameters θ .

With the data and parameters defined, we proceed to the inference phase, which consists of:

1. **Point Estimation:** The objective here is to derive point estimates for θ using estimators like Least Square (LS), Maximum Likelihood Estimator (MLE), or Maximum A Posteriori (MAP).
2. **Range Estimation:** We establish range estimates to understand the variability and uncertainty in parameter estimates. This includes constructing Mean Squared Error (MSE), variance-covariance analysis and the evaluation of Confidence Intervals (CI).

This structured approach, from data and parameter definition to inferential methods application is crucial for accurately quantifying uncertainties in WCD estimation. It provides a framework adaptable to the varied complexities in environmental monitoring.

1.1 Main inference perspectives

In the realm of statistical inference for environmental analysis, particularly for WCD, two main perspectives dominate: Bayesian and frequentist approaches. Bayesian methods, rooted in Bayes’ theorem, update prior knowledge about parameters, represented as probability distributions, with new evidence from observed data. This approach is encapsulated by the formula $P(\theta|\mathbf{y}) \propto P(\mathbf{y}|\theta) \cdot P(\theta)$, where $P(\theta|\mathbf{y})$ is the posterior probability of the parameters θ given data \mathbf{y} , $P(\mathbf{y}|\theta)$ is the likelihood of observing \mathbf{y} under θ , and $P(\theta)$ is the prior probability of θ . Within Bayesian analysis, the MAP estimator is used to identify parameter values that maximize the posterior distribution. Bayes factors and posterior distributions are employed to derive credible intervals for uncertainty quantification in Bayesian statistics. Although

1. Theoretically, θ encompasses various aspects of a distribution, such as location and dispersion parameters. Traditional analysis assumes noise factors are known, simplifying the focus on primary modeling parameters.

Bayesian methods offer valuable insights, especially in contexts with well-established priors, they may face challenges in dynamic environments like coastal zones, where prior information can be limited, constantly outdated or non-existent.

Conversely, frequentist approaches, which focus on the long-run frequency properties of estimators, are characterized by the direct analysis of observed data without incorporating prior beliefs. Central to this approach is the concept of parameter estimation using techniques like the LS and MLE, where parameters $\tilde{\theta}$ are estimated from the observed data \mathbf{y} . The frequentist perspective is exemplified by estimators such as $\hat{\theta} = \arg \max_{\theta} P(\mathbf{y}|\theta)$, where $\hat{\theta}$ is the value that maximizes the likelihood of the observed data. This approach is particularly relevant for WCD analysis, where direct analytical computations, such as variance-covariance propagation, offer a valuable tool for uncertainty quantification. Additionally, bootstrapping which is based on resampling from the observed data can also be viewed as a frequentist approach for approximating the statistical distribution of LS and MLE estimators² [69].

In this chapter, while acknowledging the merits of both frequentist and Bayesian methodologies, we predominantly focus on frequentist approaches other than bootstrapping, as they offer practical advantages in handling the complexities and variabilities inherent in environmental data. Although effective and versatile, bootstrapping can be computationally intensive and may fail to provide a reliable approximation of the underlying distribution, leading to inaccurate inferences. The computational implementation of Bayesian methods often involves sophisticated techniques like Markov Chain Monte Carlo (MCMC), which, while pivotal in approximating the posterior distribution $P(\theta|\mathbf{y})$, may not scale efficiently for deriving uncertainties at a pixel-level. The choice of frequentist methods such as the LS and MLE aligns with the widely accepted Guide to the expression of Uncertainty in Measurement (GUM) methodology, the nature of our data and the analytical goals of our study, providing a solid framework for uncertainties and efficiency in handling high volumes spectral data.

1.2 Uncertainty and inference metrics

In the field of remote sensing, especially when delving into complex processes like radiative transfer modeling and photogrammetry, statistical inference plays a crucial role in making sense of data. A fundamental aspect often overlooked in this process is the clear differentiation between the concepts of uncertainty and the range metrics used in statistical inference, such as MSE and frequentist CI.

Uncertainty, in a broad sense, encompasses all forms of unknowns in measurement or estima-

2. Bootstrapping is typically used for analyzing actual data when the underlying distribution is unknown, leveraging the sample's empirical distribution to estimate statistical properties. Conversely, Monte Carlo simulations are applied in scenarios where the model is known, using random sampling from specified distributions to explore theoretical outcomes or simulate complex systems.

tion. It arises from various sources, including model specification, measurement errors, and inherent data variability. In statistical inference, metrics like MSE and CI are tools to gauge this uncertainty, revealing insights into the estimator’s precision (variability) and accuracy (systematic deviation from the true value) as illustrated in Figure 2.1.

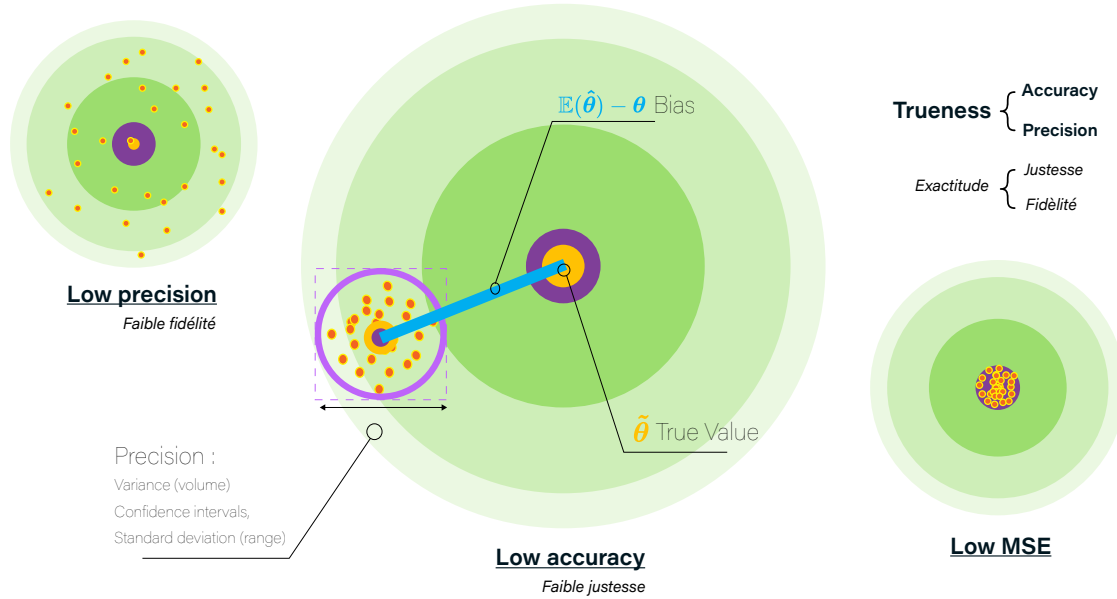


Figure 2.1 – A graphical representation of statistical measurement concepts, illustrating precision, accuracy, trueness (low MSE) with French translation in italics. The first panel shows a scatter with low precision, indicating a wide spread of data points around the target. The second panel demonstrates low accuracy with a significant bias from the true value. The third panel illustrates trueness as a combination of accuracy and precision, characterized with tightly clustered estimations around the true value.

However, there’s a common misconception in relying solely on these inference metrics to assess uncertainty. While CI, for example, are vital for quantifying the precision of an estimator, they don’t fully capture the totality of uncertainty, especially when the estimator is biased. This is particularly relevant in remote sensing applications, where often, the analysis is based on single-sample estimates, like the inversion of a single spectrum per pixel or triangulating two homologous rays for a feature point. In such scenarios, even a well-specified model can lead to biased estimators due to the limited sample size. This bias, if not accounted for, can render confidence intervals misleading, as they might not accurately represent the true range within which the parameter lies³. Therefore, a rigorous evaluation of uncertainty should consider not just the precision (as captured by CI) but also the accuracy, which involves understanding and adjusting for any potential bias in the estimators.

3. The systematic deviation induced by bias in an estimator results in skewed CI. If an estimator consistently overestimates or underestimates a parameter, the resulting CI, although precise, may not accurately encompass the true parameter value. This misalignment leads to intervals that give a false sense of accuracy, as they are skewed either above or below the true value due to the bias. Therefore, it is crucial to account for and correct bias in estimators to ensure that CI accurately represent the uncertainty around the estimated parameter.

This exploration of statistical inference and its broader relation to uncertainty as a concept in metrology sets the stage for upcoming sections, each dedicated to a specific statistical framework. We will first explore the variance-covariance framework which provides precision of estimates, followed by an in-depth look at the likelihood-based inference frameworks centered around the MLE and its statistical tests asymptotic properties. These sections explore the application of statistical inference theory to the practical challenges of quantifying environmental parameters uncertainty.

2 Variance-covariance framework

Building upon the foundations of statistical inference outlined earlier, particularly in the realms of radiative transfer and photogrammetry, we delve into the variance-covariance framework. This framework plays a pivotal role in quantifying the uncertainty of parameters estimated from observational data, especially in parametric models that are central to our study.

This section provides a mathematical exposition of how this framework is applied to determine the uncertainties in parameters $\boldsymbol{\theta}$ based on observed data \mathbf{y} . While most of studies based on the GUM approach [70] commonly present uncertainty quantification in a direct form, relating inputs to outputs as detailed in the annex section (referenced in Section 1), this work explores the inverse perspective, demonstrating the progression of uncertainty propagation from observed data to the estimation of parameters within the variance-covariance framework.

In this context, consider the additive Gaussian errors model, a cornerstone in the domain of statistical inference for remote sensing:

$$\mathbf{y} = \boldsymbol{\eta}(\boldsymbol{\theta}) + \boldsymbol{\epsilon} \quad (2.1)$$

where $\boldsymbol{\epsilon}$ denotes measurement noise, and $\boldsymbol{\eta}(\boldsymbol{\theta})$ represents the function mapping the parameters $\boldsymbol{\theta}$ to the observed data \mathbf{y} . The heart of commonly adopted analysis lies in the LS estimator, $\hat{\boldsymbol{\theta}}$, designed to minimize a cost function that acknowledges the noise in the data:

$$\hat{\boldsymbol{\theta}} = \arg \min_{\boldsymbol{\theta}} \left\{ \frac{1}{2} (\mathbf{y} - \boldsymbol{\eta}(\boldsymbol{\theta}))^T \boldsymbol{\Sigma}_{\mathbf{y}}^{-1} (\mathbf{y} - \boldsymbol{\eta}(\boldsymbol{\theta})) \right\} \quad (2.2)$$

Here, $\boldsymbol{\Sigma}_{\mathbf{y}}^{-1}$ represents the inverse of the variance-covariance matrix of the noise, ensuring that our estimation process robustly accounts for uncertainties in measurements. The variance-covariance matrix of the estimated parameters $\hat{\boldsymbol{\theta}}$, denoted as $\boldsymbol{\Sigma}_{\hat{\boldsymbol{\theta}}}$, is central to our discussion. It can be approximated using a first-order Taylor series expansion of $\boldsymbol{\eta}$ around $\hat{\boldsymbol{\theta}}$ (see Appendix section 1.1), and is given by:

$$\boldsymbol{\Sigma}_{\hat{\boldsymbol{\theta}}} \approx (\mathbf{J}^T \boldsymbol{\Sigma}_{\mathbf{y}}^{-1} \mathbf{J})^{-1} \quad (2.3)$$

where \mathbf{J} is the Jacobian matrix of partial derivatives of $\boldsymbol{\eta}$ with respect to $\boldsymbol{\theta}$. This approximation becomes an equality if the model is linear.

Figure 2.2 illustrates the geometric interpretation of the variance-covariance matrix in the parameter estimation process. The visualization offers an intuitive understanding of how the confidence regions encapsulate the uncertainty in the estimates of $\boldsymbol{\theta}$, corresponding to the precision of our model in the context of observational data \mathbf{y} .

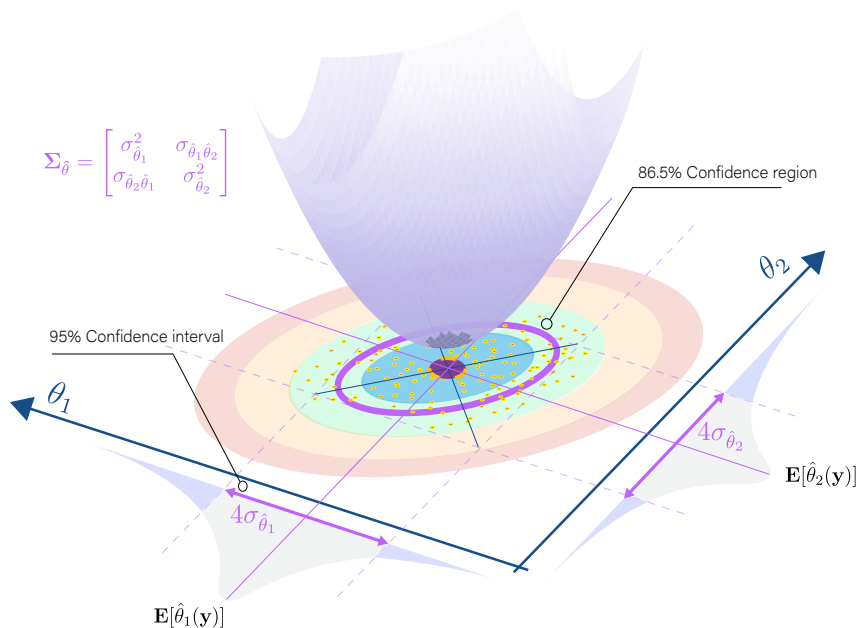


Figure 2.2 – This figure visually represents the least squares estimation process within the variance-covariance framework. The curved surface depicts a cost function realization for a linear measurement model. The center of the ellipses marks the expected values $E[\hat{\boldsymbol{\theta}}(\mathbf{y})]$, with the surrounding ellipses (in purple) representing the 86.5% confidence regions based on the variance-covariance matrix $\Sigma_{\hat{\boldsymbol{\theta}}}$. The intervals delineated as $4\sigma_{\hat{\theta}_1}$ and $4\sigma_{\hat{\theta}_2}$, measure the 95% CI of parameters θ_1 and θ_2 , respectively.

This exploration into the variance-covariance framework and the LS estimator emphasizes the intricate interplay between parameter estimation, uncertainty quantification, and the underlying assumptions of statistical models.

Implications for WCD uncertainty

In the context of WCD estimation, this framework quantifies the uncertainty in the WCD parameter derived from either radiometric or geometric data. For instance, in radiometric WCD inference, $\boldsymbol{\theta}$ could involve the parameters defining water and seabed optical properties, or atmospheric conditions that influence the observed R_{rs} . Similarly, in geometric analysis, $\boldsymbol{\theta}$

might include aspects such as sensor orientation or environmental factors affecting line-of-sight measurements.

The LS estimator is optimal under specific conditions, such as when the error terms follow a normal distribution. It is notably sensitive to outliers, as the squared residuals can disproportionately impact the estimation. This lack of robustness requires caution, especially in remote sensing applications where anomalies are common. Moreover, it is important to note that the variance-covariance framework relies on the assumption of local linearity based on the validity of the linear approximation provided by the Taylor series expansion. This may limit its applicability in scenarios where the model or data exhibit significant non-linearities, potentially leading to misevaluation of the true uncertainty in the estimated parameters.

While the variance-covariance framework provides a systematic and efficient approach to estimating the uncertainty in parameters, its application in complex scenarios like radiometric WCD estimation requires careful consideration of its assumptions and limitations [8]. The framework’s tendency to simplify complex relationships and potentially underrepresent uncertainties must be considered when evaluating the reliability and accuracy of WCD estimates derived on the basis of radiometric and geometric analysis of spectral imagery data.

In the following sections, more sophisticated approaches, particularly those based on likelihood-based inference, are explored to address some of these limitations, offering a more robust and comprehensive description of uncertainties in WCD inference from spectral imagery.

3 Likelihood-based inference framework

The data generating process, guided by specific probability distributions, sets the stage for our likelihood-based inference. These distributions are crucial as they capture the randomness and uncertainties present in the observed data. The core of likelihood-based inference lies in the likelihood function which evaluates the parameters likelihood given the observed data, linking theoretical distributions to empirical evidence. The likelihood function, denoted as $L(\boldsymbol{\theta}; \mathbf{y})$, considers the observed data \mathbf{y} as fixed and evaluates the likelihood of the parameters $\boldsymbol{\theta}$ given \mathbf{y} . Most of statistical distributions are mathematical constructions with convolved exponential and products. As such, we often work with the log-likelihood defined as $\ell(\boldsymbol{\theta}; \mathbf{y}) = \ln(L(\boldsymbol{\theta}; \mathbf{y}))$ for analytical comfort. For a given data set \mathbf{y} , the MLE $\hat{\boldsymbol{\theta}}$ can be computed by maximizing the log-likelihood function:

$$\hat{\boldsymbol{\theta}} = \arg \max_{\boldsymbol{\theta}} \ell(\boldsymbol{\theta}; \mathbf{y}) \tag{2.4}$$

The MLE provide the most likely values for $\boldsymbol{\theta}$. The well-known asymptotic properties of the MLE $\hat{\boldsymbol{\theta}}$ are encapsulated in the following convergence in distribution:

$$\sqrt{n}(\hat{\boldsymbol{\theta}} - \tilde{\boldsymbol{\theta}}) \xrightarrow{d} \mathcal{N}(0_{\mathbb{R}^p}, \mathbf{i}(\tilde{\boldsymbol{\theta}})^{-1}) \quad (2.5)$$

where the Expected Fisher Information Matrix (EFIM) is defined as:

$$\mathbf{i}(\boldsymbol{\theta}) = \mathbb{E}[\mathbf{j}(\boldsymbol{\theta}, \mathbf{y})], \quad \mathbf{j}(\boldsymbol{\theta}, \mathbf{y}) = -\frac{\partial^2 \ell(\boldsymbol{\theta}; \mathbf{y})}{\partial \boldsymbol{\theta}^2} \quad (2.6)$$

As the sample size n approaches infinity, the MLE $\hat{\boldsymbol{\theta}}$ becomes an unbiased estimator of the true parameter $\tilde{\boldsymbol{\theta}}$, as indicated by the term $\sqrt{n}(\hat{\boldsymbol{\theta}} - \tilde{\boldsymbol{\theta}})$. In this context, the Cramér-Rao lower bound is relevant [71; 72], as it establishes that the variance of any unbiased estimator cannot be lower than the inverse of the Fisher Information Matrix. Therefore, as the MLE's variance approaches this inverse, particularly in large samples, it becomes a minimum-variance unbiased estimator. The rate of convergence is $\mathcal{O}(n^{-1/2})$, implying that the accuracy of the MLE improves at the rate of $n^{-1/2}$ as the sample size increases. Notably, Observed Fisher Information Matrix (OFIM) (Figure 2.3) given by \mathbf{j} can be used as a practical substitute for \mathbf{i} in finite samples [73].

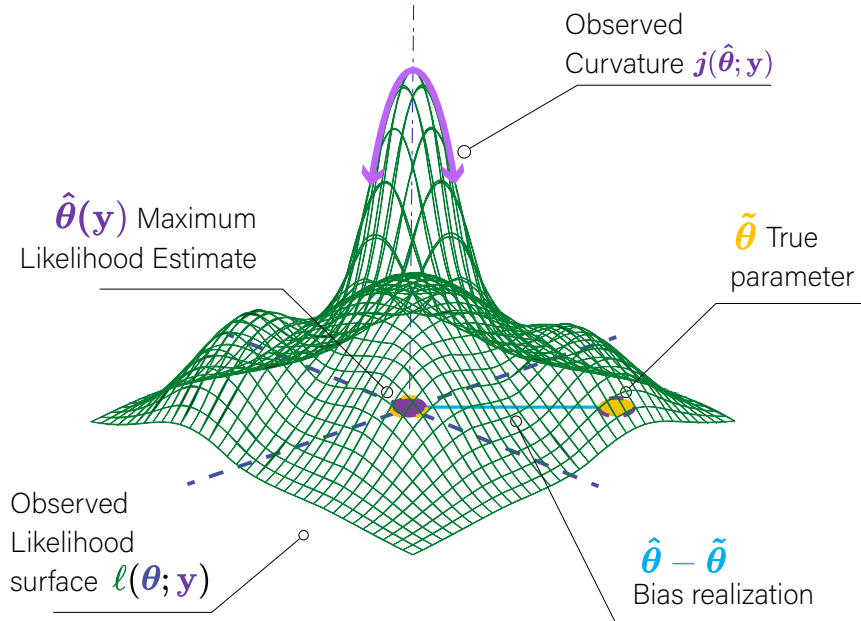


Figure 2.3 – Geometrical interpretation of Fisher Information: This figure illustrates a likelihood surface for a two-dimensional parameter space. It highlights the MLE Bias and shows the observed curvature, which is indicative of the OFIM. The EFIM can be interpreted as the average curvature over multiple data realizations \mathbf{y} .

Within the likelihood-based inference framework, a notable connection to the variance-covariance framework emerges, particularly under Gaussian error assumptions [74]. In such scenarios, the MLE is the LS estimator and the Expected Fisher Information Matrix ($\mathbf{i}(\boldsymbol{\theta})$) is equal to the

inverse of the variance-covariance matrix ($\Sigma_{\hat{\theta}}$) of the parameter estimates as defined in Equation 2.3 (see Appendix section 1.1). This equivalence underscores the comprehensiveness of the likelihood-based approach, incorporating the essential aspects of the variance-covariance framework, especially in the precision evaluation of MLE under common Gaussian error models.

4 Profile likelihood-based inference

In the previous sections, we explored different frameworks for quantifying uncertainties in general. Building upon these foundations, this section extends these concepts to the specific context of WCD uncertainties as a parameter of interest. We will delve into different aspects of inference under the presence of nuisance parameters. These mainly evolve around the profile likelihood and include first-order inference, higher-order inference, and the examination of their practical aspects. This framework is not only compatible with the previously discussed methodologies but also innovates in addressing WCD uncertainties in two distinct inferential contexts: radiometric and geometric inference. The upcoming subsections will demonstrate how this framework can be applied effectively, ensuring a unified and robust approach to quantify WCD estimation under different inferential contexts.

4.1 Nuisance in radiometric and geometric inference

Our focus spans across both radiometric and geometric inference, addressing the complexities inherent in each. Interest parameters, crucial for our estimation efforts, are those quantities we aim to derive from the data. These parameters, be it in the context of remote sensing or metrology, are the focal points of our inference. Conversely, nuisance parameters, though not the primary target of our estimation, play a vital role in the integrity of our models, influencing the data in ways that cannot be overlooked.

In radiometric inference, such as optical remote sensing, nuisance parameters include the water IOP and the seabed submodels parameters, as well as factors like sensor calibration or atmospheric correction elements, crucial for accurate WCD estimation. In geometric inference for through-water photogrammetry, nuisance parameters include sensor-specific factors such as calibration offsets and alignment errors, as well as acquisition-specific issues like refraction-induced distortions, and systematic errors related to motion or environmental conditions, all of which must be modeled to ensure accurate 3D reconstruction. These parameters, although not the primary focus, are essential for correcting systematic biases and enhancing model accuracy. Formally, the underlying data parameter, θ , is hence decomposed into $\theta = (\psi, \omega)$, where ψ is the scalar parameter of interest and ω represents the vector of nuisance parameters.

This bifurcation is especially pertinent in our study of WCD, where we aim to infer a scalar quantity amidst a plethora of influencing factors.

This unified approach, applicable across different modeling strategies for the nuisance component, ensures that our methodology for WCD uncertainties is adaptable and robust. In the specific context of through-water stereo-photogrammetry, we consider the WAI height as an additional parameters which, once accounted for, allows for a more accurate and representative uncertainty estimation of WCD. Thus, this framework not only accommodates the nuances of both radiometric and geometric inference but also offers a cohesive and comprehensive strategy for addressing WCD uncertainties in these varied yet interconnected domains.

Similar to the full parameter likelihood-based inference, the estimation of $\boldsymbol{\theta} = (\psi, \boldsymbol{\omega})$ follows the principles of MLE. In this context, the MLE of $\boldsymbol{\theta}$ is simultaneously the MLE of both the interest parameter ψ and the nuisance parameters $\boldsymbol{\omega}$. This is mathematically represented by the equation:

$$\hat{\boldsymbol{\theta}} = (\hat{\psi}, \hat{\boldsymbol{\omega}}) = \arg \max_{\psi, \boldsymbol{\omega}} \ell(\psi, \boldsymbol{\omega}; \mathbf{y}) \quad (2.7)$$

In this equation, $\hat{\boldsymbol{\theta}}$ is the vector of estimated parameters where $\hat{\psi}$ and $\hat{\boldsymbol{\omega}}$ are the estimates that maximize the likelihood function $\ell(\psi, \boldsymbol{\omega}; \mathbf{y})$ given the observed data \mathbf{y} . The maximization of the likelihood function with respect to both ψ and $\boldsymbol{\omega}$ ensures that the estimates are the most likely values for these parameters given the data.

This forms the basis for the subsequent profile likelihood approach where the focus shifts to the parameter of interest ψ , while effectively handling the nuisance parameters $\boldsymbol{\omega}$.

4.2 First-order inference

In the domain of first-order inference of an interest parameter, we employ profile likelihood and associated statistical tests as pivotal tools for deriving and evaluating CI for WCD in both radiometric and geometric analysis. This approach facilitates the extraction of meaningful insights from complex datasets, uncertainty included, balancing the precision and computational feasibility essential in environmental monitoring and remote sensing applications.

4.2.1 Profile likelihood

The concept of profile likelihood plays a critical role in statistical inference, particularly when focusing on a parameter of interest ψ while accounting for nuisance parameters. It serves as a powerful tool for practical identifiability [75; 76; 77; 78], offering insights into the parameter space that might be obscured in a full likelihood analysis.

The profile likelihood of the parameter of interest ψ is defined as:

$$\ell_p(\psi; \mathbf{y}) = \max_{\omega} \ell(\psi, \omega; \mathbf{y}) = \ell(\psi, \hat{\omega}_\psi; \mathbf{y}) \quad (2.8)$$

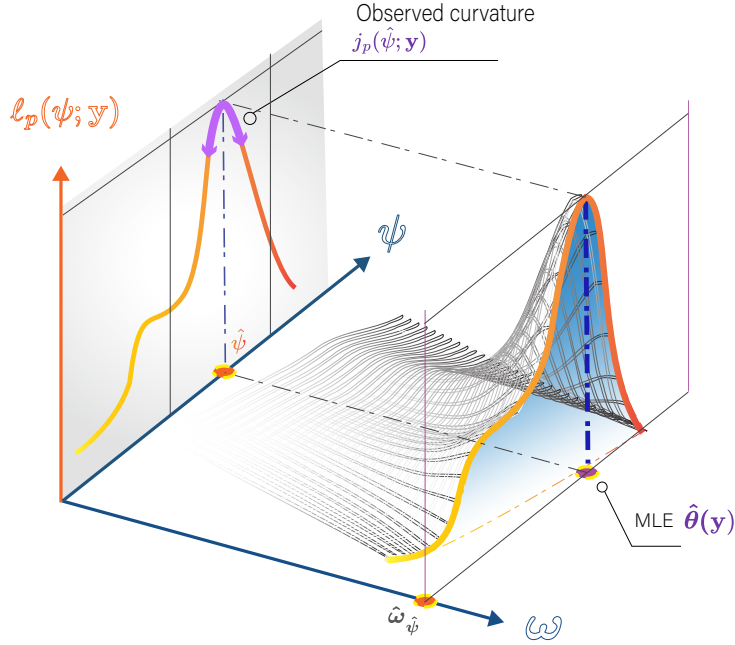


Figure 2.4 – Geometrical illustration of profile Likelihood: This figure illustrates a profile likelihood surface for a two-dimensional parameter space.

In essence, the profile likelihood $\ell_p(\psi; \mathbf{y})$ simplifies the likelihood function by focusing on ψ and adjusting the nuisance parameters ω accordingly. This is achieved by maximizing the likelihood with respect to the nuisance parameter, resulting in the constrained maximum likelihood $\hat{\omega}_\psi$ for each value of ψ (see Figure 2.4).

4.2.2 First-order statistical tests

For a scalar parameter of interest ψ , first-order inference can be performed based on the following test statistics [79]:

$$r(\psi; \mathbf{y}) = \text{sign}(\hat{\psi} - \psi) \sqrt{2(\ell_p(\hat{\psi}; \mathbf{y}) - \ell(\psi; \mathbf{y}))}, \quad (2.9)$$

$$t_o(\psi; \mathbf{y}) = j_p(\hat{\psi}; \mathbf{y})^{-1/2}(\hat{\psi} - \psi), \quad (2.10)$$

$$t_e(\psi; \mathbf{y}) = i_p(\hat{\psi})^{-1/2}(\hat{\psi} - \psi), \quad (2.11)$$

$$s(\psi; \mathbf{y}) = j_p(\hat{\psi}; \mathbf{y})^{1/2} \frac{\partial \ell_p(\psi; \mathbf{y})}{\partial \psi} \quad (2.12)$$

Here, r is the signed likelihood ratio statistic, t_o and t_e are the Wald test statistics using observed and expected information respectively, and s is the score statistic. $j_p(\hat{\psi}; \mathbf{y})$ and $i_p(\hat{\psi})$ are the observed and expected information of ψ at the MLE, given by:

$$j_p(\hat{\psi}; \mathbf{y}) = -\frac{\partial^2 \ell_p(\hat{\psi}; \mathbf{y})}{\partial \psi^2}, \quad (2.13)$$

$$i_p(\hat{\psi}) = \mathbb{E}[j_p(\hat{\psi}; \mathbf{y})] \quad (2.14)$$

Under certain regularity conditions, the main results of first-order inference can be summarized as follows:

$$st(\tilde{\psi}; \mathbf{y}) \xrightarrow{O(n^{-1/2})} \mathcal{N}(0, 1) \quad \text{for } st \in \{r, t_o, t_e, s\}. \quad (2.15)$$

This stipulates that under the null hypothesis (i.e. at the true value $\tilde{\psi}$), all these test statistics asymptotically follow a standard normal distribution. Importantly, the speed of convergence to this limiting distribution is of order $O(n^{-1/2})$, which is characteristic of first-order methods. These test statistics can be used to derive CI as will be described in Section 4.3.

4.3 Evaluation of Confidence Intervals performance

Building upon the first-order inference methods discussed earlier, our research central focus is the evaluation of the performance of CI for WCD derived from Semi-Analytical (SA) models in radiometric analysis and through water stereo-triangulation geometric analysis. Specifically, we focus on the concept of coverage probability to assess the reliability of these intervals. Coverage probability is defined as the frequency with which the true value of the parameter of interest, ψ , falls within the estimated CI $\mathcal{A}(\mathbf{y})$. Mathematically, coverage probability is expressed as:

$$P(\tilde{\psi} \in \mathcal{A}(\mathbf{y})) = 1 - \alpha \quad (2.16)$$

Here, α represents the significance level, commonly set at 0.05 for a 95% confidence level.

To construct these CI, we employ the first-order test statistics introduced in Equation 2.15. The CI based on these tests can be derived as follows:

$$\text{For } r : \psi \in \{\psi : |r(\psi; \mathbf{y})| \leq z_{\alpha/2}\} \quad (2.17)$$

$$\text{For } t_o : \psi \in \left\{ \hat{\psi} \pm z_{\alpha/2} \sqrt{j_p(\psi; \mathbf{y})} \right\} \quad (2.18)$$

$$\text{For } t_e : \psi \in \left\{ \hat{\psi} \pm z_{\alpha/2} \sqrt{i_p(\psi)} \right\} \quad (2.19)$$

$$\text{For } s : \psi \in \{\psi : |s(\psi; \mathbf{y})| \leq z_{\alpha/2}\} \quad (2.20)$$

Here, $z_{\alpha/2}$ is the critical value corresponding to the $\alpha/2$ tail of a standard normal distribution, generally approximated as 1.96 for a 95% confidence level.

In order to empirically validate the coverage probability of CI, we use Monte Carlo simulations to generate sample data \mathbf{y} from the actual parameter values $\tilde{\boldsymbol{\theta}}$. Specifically, we calculate the observed test statistic for each sample \mathbf{y} at the true $\tilde{\psi}$ value under the null hypothesis. An observed test statistic's absolute value greater than $z_{\alpha/2} = 1.96$ would indicate that the null hypothesis can be rejected at the 95% confidence level (see Figure 2.5). This Monte Carlo-based evaluation is particularly useful for the r test statistic, which often requires numerical methods to determine the confidence intervals due to its reliance on the profile likelihood. Wald tests calculations can be directly performed at the MLE while the score can be obtained directly from the log-likelihood derivative.

As highlighted in Figure 2.5, Wald tests t_o and t_e are linear slopes by construction, which yield symmetric CI around the MLE $\hat{\psi}$. On the other hand, r and s effectively capture the asymmetric behavior which can arise in non linear setups⁴.

In the realm of first-order inference for WCD analysis in remote sensing, especially in radiometric and geometric contexts, the use of profile likelihood remains notably scarce, despite its longstanding presence as a statistical tool. To our knowledge, the explicit application of profile likelihood in remote sensing studies, particularly those investigating WCD, is almost non-existent.

However, it's important to highlight that the use of the Expected Fisher Information and Wald tests, particularly under Gaussian errors, is effectively equivalent to variance-covariance propagation. It is also worth mentioning that j_p (resp. i_p) are equivalent to the diagonal elements at ψ blocks of the observed (resp. expected) information matrices traditionally computed in multidimensional inference on $\boldsymbol{\theta}$, the full parameter set (See Appendix section 2). Furthermore, it should be emphasized that scalar ψ test statistics are in harmony with established multidimensional inference techniques. In those broader contexts, the test statistics converge to a chi-squared distribution, where the degrees of freedom match the dimensionality of the

4. Nonlinear setups manifest in the profile likelihood as divergence from the parabolic behavior associated to quadratic cost functions in linear models.

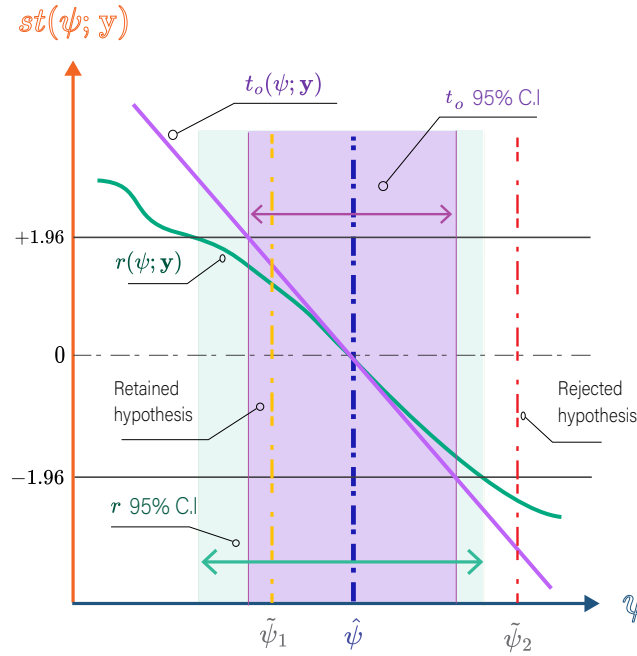


Figure 2.5 – First-order statistical tests and hypothesis testing: The red (resp. yellow) line indicates a case of (resp. non) rejection of the null hypothesis ψ (Type I error) which should theoretically occur 5% of the time on the long run, depending on the statistical test performance. The r curve, depicted for a small sample scenario, is expected to exhibit a linearly decreasing trend analogous to Wald tests with increasing sample size.

interest parameter. This ensures that focusing on a scalar parameter ψ does not deviate from traditional multidimensional inference methods.

These equivalences subtly implies an implicit use of profile likelihood concepts through Wald tests, making the profile likelihood framework more extensive with the likelihood ratio and the score as additional tools as well as applicable for quantifying uncertainties. Consequently, this framework can be comprehensively placed under the umbrella of profile likelihood, underscoring its broader relevance and untapped potential in remote sensing and environmental analysis.

5 Higher-order asymptotic inference

Several practical considerations arise in our research on WCD inference from spectral imagery with radiometric and geometric methods. In real-world applications, the true parameter values $\tilde{\theta}$ are unknown and substituted by their MLE with precision evaluations through variance-covariance or CI, which is a valid inference if the bias is tolerable under the analyzed sample size. In practical applications, the validity of this approximation and what consti-

tutes a "sufficient" sample size n become especially relevant when considering the presence of nuisance components. The sample size constraint intensifies the role of nuisance parameters, which may deplete a significant amount of the information required for precise inference of the primary parameter of interest.

To address these complex issues, first-order inference methods which further generalizes the asymptotic property of the MLE (Equation 2.5) for an interest parameter based on the profile likelihood were improved based on higher-order asymptotic theory's adjustments [64; 65; 66; 80; 81]. While a comprehensive exploration of higher-order asymptotic theory falls outside the purview of this study, this section aims to highlight the key advancements in this field and their practical implications. For further theoretical insight, the reader is referred to a comprehensive review in [82], while [66] provides an accessible description of these advanced methods in practice.

5.1 Sufficiency and ancillarity

Central to later advancements is the concept of sufficiency, about a parameter from the data, and the concept of ancillary statistic which is a function of data which holds no information on the parameter. The data \mathbf{y} can be conceptually summarized by the MLE and an appropriate ancillary statistic, and fixing the latter ensures that the former is sufficient. Such arguments form the essence of conditional inference.

Definition: Sufficiency

A statistic is said to be sufficient for a parameter if it captures all the information in the sample about that parameter. Formally, a statistic $T(\mathbf{y})$ is sufficient for a parameter θ if the conditional distribution of the sample data \mathbf{y} , given $T(\mathbf{y})$, does not depend on θ .

Definition: Ancillarity

An ancillary statistic is a statistic whose distribution does not depend on the parameter being estimated. It provides no information about the parameter itself.

While notions of sufficiency and ancillarity are often introduced with academic examples⁵,

5. In a Gaussian distribution with known variance, the sample mean is sufficient for the population mean, while the sample range is ancillary, indicating data spread without affecting the population mean estimation.

their abstraction is best illustrated through tangible examples such as in [73]. This leads us to the intriguing proposition in conditional inference: while estimating confidence intervals for WCD, it is argued that one should condition on this ancillary statistic. The rationale behind this approach is to enhance the sufficiency of the remaining data. By holding fixed the ancillary statistic, we focus the inferential process on the subset of data that is most informative for WCD.

Beyond ancillarity and sufficiency, conditional inference guides many methodological choices in remote sensing and other fields where the goal is to isolate the effect of chosen variables from others and assess their uncertainties. Whether in geometric refinements or radiometric calibration, the objective is that subsequent analyses can be conditioned on the assumption that these corrections have been conducted. By concentrating on subsets or transformations of data that are independent of extraneous parameters, researchers can ensure that the integrity of their inference is maintained by focusing solely on the essential informational content of the data. This approach not only streamlines the computational process but also potentially increases the robustness of the results by reducing overfitting and the propagation of uncertainty from irrelevant processes.

5.2 Modified likelihood ratio

Building on these concepts, [64] introduced the p^* formula, a third-order $O(n^{-3/2})$ approximation of the MLE, representing a significant leap in this field. This formula laid the groundwork for the modified likelihood ratio statistic r^* allowing for more accurate inference and hypothesis testing. In the presence of nuisance parameters, r^* can be expressed as follows [82]:

$$r^* = r + \frac{1}{r} \log(C^{-1}) + \frac{1}{r} \log(u/r), \quad (2.21)$$

where r^* is the signed root of the likelihood ratio test, a third order likelihood ratio for deriving confidence intervals with better coverage and more accurate hypothesis testing. While the preference for the 'non-modified' likelihood ratio over other first-order statistical tests in small samples is primarily informed by empirical evidence, Barndorff-Nielsen argues that the natural emergence of r in higher-order inference methods provides theoretical support for this inclination. Without delving into the specifics of terms C and u , they both involve sample space derivatives which necessitate the definition of an ancillary statistic. Essentially, these are derivatives of the likelihood with respect to the observed data values, with the ancillary statistic held fixed. The term involving C in the modified likelihood ratio r^* is recognized as the nuisance adjustment, while the term with u is referred to as the information adjustment. As noted by [66] and [82], in practical applications, the nuisance adjustment often predominates, underscoring the significant impact of nuisance parameters on influencing the precision of first-order inference methods.

The derivation of third order likelihood ratio r^* is hindered by the challenges of obtaining sample space derivatives and finding appropriate ancillary statistics in non-textbook statistical models. In order to make higher-order accessible for practical applications, approximation to C and u were proposed as second-order adjustments by subsequent researchers to address these difficulties. [65] and [80] provided empirical approximations for the modifications, while [81] tailored adjustments for nonlinear regression models with single replica samples. These methods, exceeding the first-order accuracy, are pivotal in improving the convergence rate of likelihood ratio statistics to its theoretical distribution.

5.3 Profile likelihood adjustments

The profile likelihood is a form of pseudolikelihood. Unlike a genuine likelihood, it does not necessarily satisfy Bartlett's identities, which are given by:

$$\mathbb{E} \left[\frac{\partial \ell(\boldsymbol{\theta}; \mathbf{y})}{\partial \boldsymbol{\theta}} \right] = 0, \quad \mathbb{E} \left[-\frac{\partial^2 \ell(\boldsymbol{\theta}; \mathbf{y})}{\partial \boldsymbol{\theta}^2} \right] = \mathbb{E} \left[\left(\frac{\partial \ell(\boldsymbol{\theta}; \mathbf{y})}{\partial \boldsymbol{\theta}} \right) \left(\frac{\partial \ell(\boldsymbol{\theta}; \mathbf{y})}{\partial \boldsymbol{\theta}} \right)^T \right] \quad (2.22)$$

The profile likelihood is primarily a first-order tool, where its first derivative is typically of order $O(1)$, and the corresponding expected product also follows a first-order behavior [83; 84]. Researchers have focused on modifying the profile likelihood itself rather than the likelihood ratio [84; 83]. These adjustments aim to make the profile likelihood behave more like a "true" likelihood by satisfying Bartlett's identity and reducing its first-order bias, operating at an order of $O(n^{-1})$. The modified likelihood ratio r^* led straightforwardly to the modified profile likelihood $\ell_m(\psi; \mathbf{y})$ [64]:

$$\ell_m(\psi; y) = \ell_p(\psi; \mathbf{y}) + \log(C^{-1}) \quad (2.23)$$

Empirical adjustments allowing to avoid the derivation of the ancillary and the sample space derivatives followed in subsequent works [84; 83]. [83] established equivalent profile adjustments from a novel perspective, essentially related to the elimination of nuisance parameter space and with less reliance on conditional inference arguments.

The integration of higher-order methods into statistical practice has brought us closer to the ideal of extracting maximum information from data. The interplay of ancillarity, sufficiency, and higher-order adjustments has catalyzed the development of more nuanced inferential procedures, particularly in complex models fraught with large nuisance parameters. It is noteworthy that the application of these advanced methods remains relatively rare in applied research, with limited instances primarily in fields like biology. Their presence in remote sensing studies is particularly scarce. This restricted adoption may be due to the sophisticated

prerequisites of these methods, as well as the prevailing belief in the sufficiency and reliability of first-order inference methods, especially in studies relying on large sample sizes where first-order methods are typically robust. This gap underscores a potential area for future exploration and application in the field of remote sensing.

6 Practical aspects of likelihood based inference

The field of statistical analysis offers a variety of tools for likelihood-based inference, each with its own strengths and challenges that influence the precision of the results obtained. While Wald, likelihood ratio, and score tests are considered equivalent in large samples, numerous studies have demonstrated that their performance varies significantly under small sample conditions and depending on the inferential problem. These variations can be critical when the model form is misspecified or when dealing with complex data structures, such as those found in the follow-up studies extending beyond the field of remote sensing [85; 86; 69; 87; 88].

[86] explored the impact of model misspecification on CI performance, finding that, while likelihood ratio and score intervals remained robust, Wald intervals showed considerable variability depending on the information matrix used—EFIM or OFIM—and whether restrictions were applied in MLE estimations. This study underscores the need for careful selection of test statistics in practical applications, particularly when handling models prone to misspecification. Further comparative studies, such as those by [85] and [87], have focused on the performance of the inverses of the EFIM and OFIM, which relate directly to the Wald tests t_e and t_o . [85] found that under certain conditions, the inverse EFIM demonstrated superior MSE performance over the inverse OFIM in estimating the MLE covariance, challenging the conventional preference for the OFIM in statistical practice. [87]’s research supported these findings, highlighting the precision of confidence intervals derived from the EFIM in scenarios involving common statistical models.

On the operational side, likelihood-based inference often encounters challenges such as boundary problems where parameters fall on the edges of the parameter space, leading to convergence issues and unstable estimates as discussed in [89]. Singular points within the likelihood surface can further complicate the estimation process, as they represent flat regions where traditional asymptotic theory does not hold, undermining the reliability of first-order statistical tests. In particular, the EFIM and the OFIM can become singular either due to parameters redundancy or non-identifiability, or due to insufficient information in the data [89]. Addressing the issue of a singular Fisher Information Matrix, researchers have proposed alternative approaches like the pseudoinverse of the Fisher matrix or by reformulating the problem as an unconstrained quadratic maximization, thus providing robust solutions for estimation problems with singular information matrices [90; 91].

Higher-order adjustments are built upon the first-order inference as a foundation layer, and therefore are subject to the same operational limitations. In particular, practical application of r^* is essentially challenging due to the difficulty of obtaining sample space derivatives as stated by several authors. This is because holding an ancillary statistic fixed is a task that can be either computationally intensive or analytically intractable. If they can be derived under specific assumptions on the statistical model, approximations to these adjustments such as those proposed in [84; 80; 83] can be determined analytically, making them readily obtainable once the profile likelihood results are produced. The allure of these methods lies in their ability to offer more accurate inferential results (CI) than traditional first-order methods. However, this precision comes at the cost of increased computational complexity and stringent assumptions that may not always align with the real-world data or model specifications.

Given these complexities and challenges in likelihood-based inference—from the varying performance of different tests under small sample conditions to the issues with boundary problems, singular points, and the intricacies of higher-order adjustments—practitioners must carefully consider the specific characteristics of their data and models when selecting and implementing statistical methods.

Chapter conclusion

In this chapter, we've established a robust foundation in statistical inference, particularly tailored for WCD uncertainties evaluation. The focus has been on the profile likelihood framework, a method adept at navigating the intricate uncertainties inherent in remotely sensing environmental data, especially those influenced by nuisance parameters.

Our exploration of first-order statistical tests (Wald, score, and likelihood ratio) has revealed their distinct applications and strengths in estimating uncertainties in WCD analysis. This understanding paves the way for the more advanced higher-order asymptotic inference methods, which promise greater precision in uncertainty quantification but require careful application due to their complexity.

The upcoming chapters are designed to extend this theoretical groundwork into practical applications. Chapter 3 shifts the focus to through-water photogrammetry, introducing a novel, likelihood-based approach for WCD geometric estimation. This chapter underscores the critical need for precise uncertainty quantification in challenging scenarios, such as those involving complex sensor dynamics. Chapter 4 will apply these refined statistical tools in Semi-Analytical models for radiometric WCD inference, tackling the unique challenges of small sample sizes and low signal-to-noise ratios. The aim is to demonstrate how higher-order adjustments can significantly improve the accuracy in estimating uncertainties in these models.

Overall, this chapter sets the stage for the next chapters, which will showcase the application of these comprehensive statistical methods in practical environmental analysis scenarios, with a strong emphasis on effectively managing and quantifying uncertainties.

Chapter 3

A Likelihood-based Triangulation Method for Uncertainties in Through Water Depth Mapping

The chapter delves into the unique challenges of stereo-triangulation uncertainties in coastal environments, proposing a systematic and rigorous framework for their evaluation. It introduces an innovative likelihood-based method, specifically tailored to address the inherent complexities of water refraction and camera pose (i.e. position and orientation) uncertainties that hinder current stereo-photogrammetry approaches. A notable innovation of this method is its application to well-characterized optical camera geometries, making it particularly suitable for surveys using pushbroom cameras.

The chapter begins with a review of the methods for uncertainties evaluation in the through water photogrammetry. The associated challenges, such as the dynamic nature of water surfaces and the lack of reliable ground-truth data limiting camera poses quality are also addressed. It then described the proposed likelihood-based triangulation method, designed to navigate and mitigate these coastal-specific challenges. The theoretical foundation of this method, which encompasses triangulation estimation and uncertainty evaluation within a comprehensive likelihood framework, is detailed. This is complemented by a series of robust Monte Carlo simulations, which serve to validate the method's efficacy in assessing uncertainty, with a particular focus on analyzing the coverage probability of CI for the WCD.

Through this research, the chapter seeks to make a significant contribution to the field of coastal remote sensing, offering a more precise and reliable tool for the inference of WCD and WAI height. This work not only addresses a critical gap in coastal stereo-photogrammetry but also opens up new avenues for environmental monitoring and coastal zone management. The chapter material has been used to build a paper which has been submitted to the MDPI Journal Remote Sensing [92]. It is currently in the second round of revision with major

corrections. This research paper is authored by Mohamed Ali Ghannami as the principal author, and co-authored by Sylvie Daniel and Isabelle Quidu as co-directors and Guillaume Sicot as co-supervisor of this Ph.D.

1 Methods for uncertainty evaluation in through water photogrammetry

In this section, we aim to review the existing literature on WCD geometric inference focusing on uncertainty evaluation approaches in the through water photogrammetry context. It is worth noting that within this emergent field, few studies have specifically addressed uncertainty evaluation, as the mainstream focus is on empirical validation against reference data. Arguably, this is often because the novelty of the proposed methods in this literature domain is confined to adapting conventional land photogrammetric approaches to the through water context. From chapter 2, we have seen that inference is the joint process of deriving the estimation as well as its associated uncertainty, i.e. LS estimator with variance-covariance or MLE with first-order statistical tests. As such, although uncertainty evaluation methods are seldom addressed, the literature analysis will also be expanded to include theoretical extensions of the estimation process proposed in existing through water photogrammetry works.

In the approximate modeling of RPC, commonly used in satellite pushbroom datasets, triangulation is directly performed using coefficients provided for each stereo-pair image. [93] have applied variance-covariance propagation to the RPC to derive the uncertainty of the object coordinates and provided comparison to the physical model uncertainties. While this is a theoretically sound use of the RPC uncertainties, in the through water context, the refraction post-correction needs to be considered potentially requiring further uncertainty modeling assumptions. Although modeling RPC approximately has been shown to efficiently capture the physical model [50], this approach imposes significant limitations regarding uncertainties. RPC as a substitution of the physical model do not allow a partitioning of the uncertainty sources between the optical camera model and the exterior orientation and hence a clear uncertainty budget analysis. Furthermore, the uncertainty in RPC used for propagation is essentially derived from GCP, which are challenging, or even impossible, to obtain in coastal areas, thus hindering rigorous uncertainty evaluation.

In SfM-MVS approaches, variance-covariance propagation with the associated LS estimator is a well-established procedure among practitioners for deriving uncertainties estimates when minimizing reprojection errors. This is traditionnally performed through the collinearity equations forming the basis of modeling frame imagery. [94] have studied the uncertainty of the object coordinates by propagating uncertainties of both the exterior and the interior orientations in direct-georeferencing applications. [53] provided a detailed procedure for uncertainty

evaluation for stereo-camera reconstructions based on [70] guidelines, which are rooted in the variance-covariance approach. Although this approach is rigorously established, it faces limitations in the context of various adaptations proposed for through water imagery [59; 57]. For instance, variance-covariance is not straightforwardly applicable through the augmented collinearity version presented in [59] or after obtaining refraction-free images as proposed in [57]. This is because LS criteria are not explicitly defined in the optimal refraction solution, derived through iterative processes subject to predefined thresholds. Moreover, the evaluated uncertainty in these adapted approaches may not fully capture the additional errors introduced by the refraction correction process, similar to approximate modeling. Importantly, the lack of physical interpretability in these methods hinders the ability to efficiently extract meaningful insights from the uncertainty budget.

Ray tracing methods in multimedia optics [46; 61; 60; 51], which explicitly model refraction, may offer a more rigorous avenue for through water triangulation and its associated geometric uncertainties. However, there is little concern with statistical modeling and uncertainty evaluation in these studies as thoroughly conducted for LiDAR surveying in [95]. Recent studies [51; 96] advocates for optimizing the cost function in the object space rather than image space. In the context of land photogrammetry, [96] demonstrates that the midpoint between the lines of sight outperforms the minimization of reprojection errors when there is uncertainty on the camera's pose. In the multimedia optics context, [51] shows that the minimization of the cost function in the object space produces comparable, if not superior, accuracy compared to traditional methods. Clearly, optimizing over the object space rather than the focal plane allows to properly take into account the exterior orientation uncertainties in the triangulation, which favors this approach for deriving accurate WCD uncertainties. When inferring homologous points' positions, the exterior orientation measured by inertial cameras should be considered independently from modeling the observed image coordinates. In [94]'s study, the exterior orientation uncertainties are propagated at the optimal solution with no indication or recommendation to derive this solution under the consideration of these uncertainties. Considering that the exterior orientation is systematically refined in land photogrammetry using GCP and its role in the object coordinates uncertainty [96; 53], its accuracy becomes critical for evaluating WCD uncertainty in the through water context. This challenge is further pronounced for pushbroom cameras surveys, the most adopted technology for hyperspectral imagery, since the exterior orientation is unique to each linear footprint.

In the context of bathymetric mapping, the uncertainty evaluation is often limited to the empirical validation. The outlined limitations and challenges in existing 3D reconstruction methods underscore the need for a novel inferential approach that allows both triangulation and uncertainty evaluation, particularly in the context of coastal environments. Overall, the inability to access GCP for accurate camera pose estimation, the diversity of camera technologies and the complexities introduced by the air-water interface necessitate advancements

in modeling techniques. Our proposed methodology, detailed in the following section, addresses these challenges by introducing a likelihood-based triangulation method tailored for the unique conditions encountered in coastal area surveys. In the continuity of ray tracing approaches, our triangulation method is adapted to the 3D reconstruction of coastal seabeds considering a flat surface. We demonstrate the ability to precisely estimate the position of the water interface and its uncertainty, explicitly modeled in our proposed rigorous modeling approach. Through the likelihood framework developed in chapter 2, this method aims to provide a more accurate and reliable framework for evaluating uncertainties in the geometric WCD inferences under strict geometric modeling of the triangulation problem.

2 Methodology

This section presents the methodology used to infer the positions of homologous points in through water photogrammetry focusing on the evaluation of WCD uncertainties. We first present the positional likelihood for land context in the absence for water interface before deriving the refracted likelihood for the through water context. The likelihood-based approach to infer the position of homologous points in 3D space which are observed from different positions is described in section 2.2.

2.1 Approach and rationale

In order to establish an uncertainty budget where we can distinguish between the different sources of errors, we considered a strict modeling approach. Geometric modeling through collinearity equations is based on the critical assumption that the homologous rays from the camera to the object intersect at the matched feature point. In the through water context, this is only valid in unlikely trivial viewing geometries where the baseline is coplanar with the homologous rays [46]. Our approach for airborne coastal surveys is centered on probabilistic modeling of the camera pose, particularly focusing on the line of sight from the camera optical center to the feature point. Probabilistic modeling offers a solution by considering the camera’s pose and addressing uncertainties in a 3D space, as opposed to traditional methods focusing on reprojection errors. Unlike projective methods, we do not attribute uncertainty to reprojection errors and seek to represent triangulation uncertainty in the 3D space. Given that high-end cameras, in particular pushbroom cameras, often have a well-characterized and fixed interior orientation, our approach considers this aspect as fixed. In our application of the likelihood-based inference in the through water context, the observed data consists in measured camera poses, including camera positions denoted as \mathbf{x}_s and the corresponding attitudes which can be considered under different mathematical representations. Figure 3.1 shows the

geometric parameters involved in our through water triangulation modeling approach. The likelihood function in our approach is formulated as:

$$L(\mathbf{v}_f(\mathbf{x}_s, \mathbf{x}_f); \mathbf{y} | \hat{\mathbf{v}}_s) \quad (3.1)$$

Here, \mathbf{y} is the data vector representing the measured camera pose and \mathbf{v}_s represents a unit vector bundle that characterizes the camera's interior orientation, varying for different bands and capturing more complex geometric models inherent in pushbroom cameras. An estimation $\hat{\mathbf{v}}_s$ of the camera's interior orientation can be obtained from geometric laboratory calibrations. Our study focuses on the probabilistic representation of the camera's pose, effectively dealing with the varying conditions and complexities encountered in coastal surveys. In our model, the line-of-sight \mathbf{v}_f is a function of \mathbf{x}_f , the feature point position and the camera position \mathbf{x}_s . We consider a true camera pose that corresponds to the true geometric ray coinciding with the matched feature point. By addressing camera pose uncertainty, our aim is to determine the likelihood of the feature point \mathbf{x}_f lying within a probabilistic representation of these errors in the 3D space.

2.2 Pose probabilistic modeling

The parameter $\boldsymbol{\theta}$ describing a homologous point viewed from two camera locations include the parameters $\{h, [x_f]_x, [x_f]_y, [x_f]_z\}$ where h is the interface height and $[x_f]_x, [x_f]_y, [x_f]_z$ are the homologous point cartesian coordinates. $\boldsymbol{\theta}$ also include the cameras positions denoted \mathbf{x}_{s_i} for a camera i , but these will be considered as nuisance parameters in this study. For the WCD uncertainty evaluation, we consider the simpler problem where h is known and fixed whereas the primary parameter of interest is the WCD, *i.e.* $h - [x_f]_z$. Additionally, we consider the case where the WAI height is not known and a systematic parameter related to the WAI height h is to be inferred from the camera pose observations.

In order to model the camera pose errors in a navigation system, it is common to use probabilistic modeling techniques. We use Gaussian errors for the camera's position as they are closely related to the euclidean distance which is appropriate for cartesian coordinates. Specifically, we assume that the errors in the camera position follow a multivariate Gaussian distribution given by:

$$p(\mathbf{x}_s; \mathbf{x}_s, \boldsymbol{\Sigma}_s) = \frac{1}{\sqrt{(2\pi)^3 |\boldsymbol{\Sigma}_s|}} \exp\left(-\frac{1}{2}(\mathbf{x}_s - \mathbf{x}_s)^T \boldsymbol{\Sigma}_s^{-1} (\mathbf{x}_s - \mathbf{x}_s)\right) \quad (3.2)$$

Here, \mathbf{x}_s is the measured position vector of the camera and \mathbf{x}_s and $\boldsymbol{\Sigma}_s$ are parameters of the camera position and its variance-covariance matrix, respectively. For the attitude model-

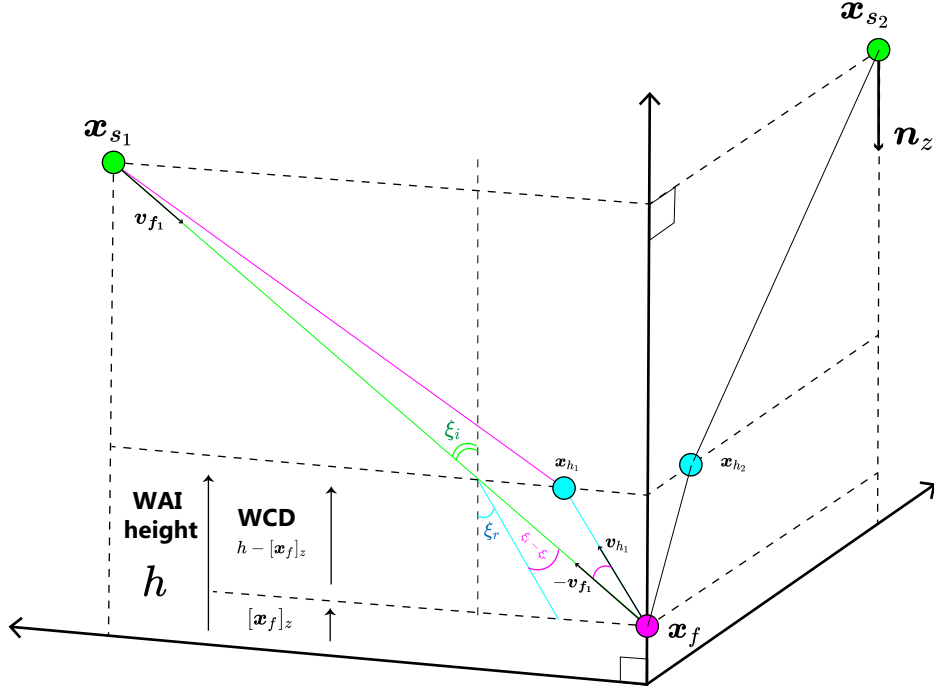


Figure 3.1 – Geometric representation of refraction for a homologous point \mathbf{x}_f and two incident rays at a planar surface determined by the WAI height. $\mathbf{x}_{s_k}, \mathbf{v}_{f_k}, \mathbf{x}_{h_k}$ and \mathbf{v}_{h_k} stand for the position, line-of-sight in the absence of refraction, the incidence point and the backward line-of-sight in the presence of refraction for the camera k , respectively. Refraction geometry is shown for camera 1 where ξ_i is the incidence angle and ξ_r is the refracted angle while \mathbf{n}_z is the nadir vector.

ing, there are various mathematical tools to represent a rotation, including rotation matrices, Euler angles, unit quaternions, Rodriguez vectors and rotors [97]. Euler angles are the popular standard for reporting inertial cameras attitude performance in terms of accuracy and precision. However, it's important to note that the relationship between Euler angles and lines of sight is not straightforward. Multiple combinations of Euler angles can represent the same line of sight. This means that for any given line of sight, there can be several different sets of Euler angles that describe it. This many-to-one relationship is important because likelihood theory typically assumes a unique maximum. Quaternions are often preferred due to their desirable mathematical properties avoiding the problems associated with Euler angles, such as the gimbal lock and discontinuities at certain angles, allowing smooth rotation interpolation. Unit quaternions ensure continuous rotations and provide a compact and straightforward way to define the minimum rotation quaternion from a reference vector representing camera interior geometry \mathbf{v}_s (represented as the nadir vector in Figure 3.2), for each line-of-sight $\mathbf{v}_f = \frac{\mathbf{x}_f - \mathbf{x}_s}{\|\mathbf{x}_f - \mathbf{x}_s\|}$ to the feature point position. The correspondence between unit quaternions and the minimum rotation lines-of-sight is unique up to sign meaning that negating a quaternion would not affect the associated rotation. The unit quaternion \mathbf{q}_f which represents the camera attitude associated to the line-of-sight \mathbf{v}_f can be defined as:

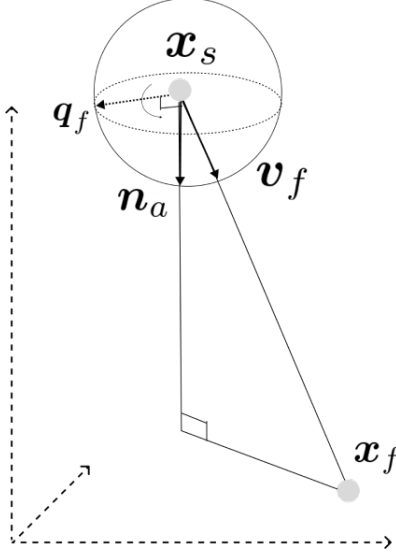


Figure 3.2 – Illustration of the quaternion q_f which defines the orientation of the camera towards the homologous point x_f .

$$q_w = |\mathbf{v}_s||\mathbf{v}_f| + \mathbf{v}_s \cdot \mathbf{v}_f \quad (3.3)$$

$$\begin{bmatrix} q_x & q_y & q_z \end{bmatrix} = \mathbf{v}_s \times \mathbf{v}_f \quad (3.4)$$

$$\mathbf{q}_f = \frac{1}{\sqrt{q_x^2 + q_y^2 + q_z^2 + q_w^2}} \begin{bmatrix} q_x & q_y & q_z & q_w \end{bmatrix} \quad (3.5)$$

$|\mathbf{v}_s|$ and $|\mathbf{v}_f|$ are the magnitudes of the rotated vector \mathbf{v}_s and the true line-of-sight direction vector \mathbf{v}_f , respectively and $\mathbf{v}_s \cdot \mathbf{v}_f$ is the dot product of both vectors. $\mathbf{v}_s \times \mathbf{v}_f$ is the cross product yielding a vector that is perpendicular to both input vectors, which represents quaternion components q_x , q_y , and q_z as the axis rotation component (See Figure 3.2). \mathbf{q}_f is normalized to have unit magnitude.

When discussing uncertainties in quaternion-based attitude modeling, Gaussian errors are often considered. These are initially represented in Euler angle space with a covariance matrix transformed to quaternion space. The direct application of Gaussian errors, however, encounters limitations due to the unit quaternion's nature lying in a finite space. Unit quaternions are four-dimensional constructs used to represent three-dimensional rotations. Their distinct feature, particularly the unit norm, renders the Gaussian distribution approach less effective. This unit norm characteristic of quaternions dictates that they reside on the surface of a hypersphere in four dimensions, a concept not fully embraced by Gaussian distributions. Consequently, the Bingham distribution is employed to more aptly model quaternion uncertainties. This distribution is more appropriate, as it naturally incorporates the unit quaternion's hyperspherical constraint adeptly accommodating uncertainties in quaternion-

based attitude modeling. The density function of the Bingham distribution for quaternion uncertainties is given by:

$$f_Q(\mathbf{q}; \mathbf{M}, \mathbf{C}) = \frac{1}{F(\mathbf{C})} \exp(\mathbf{q}^T \mathbf{M} \mathbf{C} \mathbf{M}^T \mathbf{q}) \quad (3.6)$$

Here, \mathbf{q} is the random attitude measurement as the quaternion that represents the observed orientation of the camera. In the Bingham distribution, $\mathbf{M} \in \mathbb{R}^{4 \times 4}$ is an orthogonal matrix and \mathbf{C} is a diagonal matrix of size 4×4 representing the orientation and concentration parameters, respectively. The structure of the Bingham distribution, characterized by matrices \mathbf{M} and \mathbf{C} with \mathbf{C} having a zero diagonal element, mirrors the nature of a Gaussian distribution with zero mean. The inverse covariance matrix in this context, $\Sigma^{-1} = \mathbf{M} \mathbf{C} \mathbf{M}^T$, is effectively a rank-three matrix. This mirrors the unit norm constraint on unit quaternions, suitably representing attitude uncertainties on the three-dimensional surface of the unit quaternion hypersphere.

The concentration parameter \mathbf{C} determines the spread or the shape of the distribution, whereas the orientation parameter \mathbf{M} represents the location of the distribution, also called the orientation. The diagonal elements of the concentration matrix ($C_1 \leq C_2 \leq C_3 \leq C_4 = 0$) control the degree of anisotropy of the distribution. Due to the constraint of unit norm on the quaternions, one of the diagonal concentration values must be zero. The fourth diagonal element C_4 is chosen while other conventions may use the first element. An isotropic distribution has equal concentration along all three axes of rotation, resulting in a uniform distribution of orientations $C_1 = C_2 = C_3$ (see Figure 3.3). In an anisotropic distribution, the diagonal elements of \mathbf{C} are not equal, and the distribution is stretched along one or more axes of rotation. $F(\mathbf{C})$ is a normalization constant that depends on the concentration of the density.

The orientation matrix \mathbf{M} , is directly related to the line-of-sight \mathbf{v}_f of the homologous point position \mathbf{x}_f . This is because its last column is determined by the quaternion \mathbf{q}_f representative of the line-of-sight \mathbf{v}_f . However, \mathbf{M} also controls the directions of the uncertainty shape on the 3D sphere through its first three columns. As a consequence, for a given line-of-sight \mathbf{v}_f , there exists an infinite set of orientation matrices that fulfills a maximum density at the line-of-sight \mathbf{v}_f with variable uncertainty shapes. The construction of an arbitrary orientation matrix \mathbf{M}_f for a given line-of-sight \mathbf{v}_f can be achieved by setting the last column as \mathbf{q}_f and adding its orthogonal complement, either by singular value decomposition of $\mathbf{q}_f \mathbf{q}_f^T$ or Gram-schmidt procedure. When the distribution concentration is isotropic, the approach of associating a line-of-sight to an arbitrary orientation matrix is valid because a uniform concentration C is not impacted by \mathbf{v}_f . In practice however, the attitude is provided as Euler angles and the uncertainty is often anisotropic due to the discrepancy in the INS performance between roll/pitch and yaw uncertainty. In such cases, the concentration matrix parameter \mathbf{C} is also

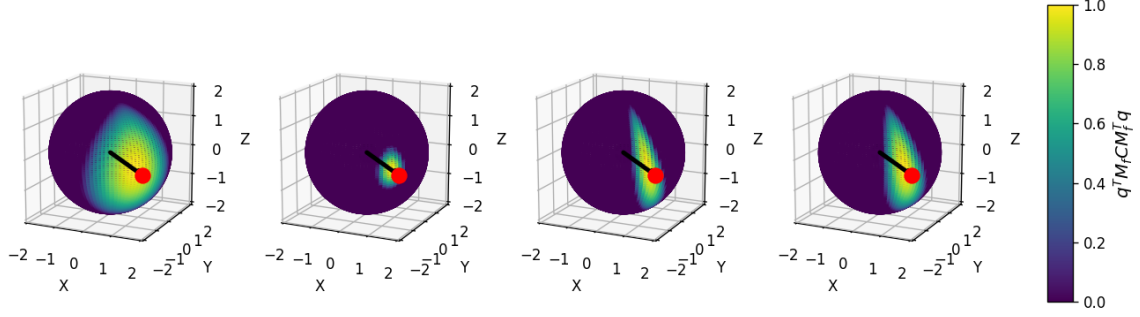


Figure 3.3 – Illustration of the Bingham concentration parameter influence. The right, middle and left spherical plots correspond to $C_1 = C_2 = C_3 = -10^8$, $C_1 = C_2 = C_3 = -10^9$, $C_1 = C_2 = 100 C_3 = -10^9$ and $C_1 = 50 C_2 = 100 C_3 = -10^9$ respectively. The black vector along with the red dot represent the true line-of-sight $\tilde{\mathbf{v}}_f$ which corresponds to the matrix \mathbf{M}_f in the Bingham distribution and the true homologous point $\tilde{\mathbf{x}}_f$ respectively. The spherical heatmap represents the non-normalized Bingham log-density: $\mathbf{q}^T \mathbf{M}_f \mathbf{C} \mathbf{M}_f^T \mathbf{q}$ mapped to the interval $[0, 1]$ for the three concentration cases.

linked to the position of \mathbf{v}_f on the sphere as it should be representative of the INS attitude uncertainty in terms of the Euler convention at the rotated vector \mathbf{v}_f . Hence, modeling the Euler attitude uncertainty can be achieved by finding the orientation matrix $\mathbf{M}_f = \mathbf{M}(\mathbf{v}_f, \Sigma_{\mathbf{a}})$ and the concentration $\mathbf{C}_f = \mathbf{C}(\mathbf{v}_f, \Sigma_{\mathbf{a}})$ that corresponds to the line-of-sight \mathbf{v}_f based on sampling from the covariance matrix $\Sigma_{\mathbf{a}}$ which describes the Eulerian attitude noise. The determination of \mathbf{M}_f , \mathbf{C}_f , and $F(\mathbf{C}_f)$ is conducted by Maximum Likelihood Estimation as prescribed in [98]. Hence we can write the attitude probability density in terms of the Euler angles convention:

$$f_Q(\mathbf{q}; \mathbf{v}_f | \Sigma_{\mathbf{a}}) = \frac{1}{F(\mathbf{C}_f)} \exp(\mathbf{q}^T \mathbf{M}_f \mathbf{C}_f \mathbf{M}_f^T \mathbf{q}) \quad (3.7)$$

Where \mathbf{M}_f and \mathbf{C}_f are the orientation and the concentration matrices associated to the line-of-sight \mathbf{v}_f and $\Sigma_{\mathbf{a}}$ is the Eulerian attitude covariance matrix.

2.3 Geometric likelihood

The principle of MLE based on the positional and refracted likelihood is used to estimate the homologous position. Using the probabilistic modeling we presented, the geometric likelihood functions can be constructed following two stages. First we consider the attitude likelihood related only to the camera's attitude uncertainty encoded in the Bingham parameters. Second, the positional likelihood can be derived by adding the contribution of the camera's position noise encoded in the variance-covariance matrix Σ_s . Based on these, the refracted likelihood for submerged homologous points considering a true average WAI height is derived under the Snell's law of refraction.

2.3.1 Positional likelihood

In general, the likelihood can be defined as the probability of the data as a function of the model parameters. Any point in the real world 3D space can be theoretically associated to a probability given a distribution on the measured camera pose. In this study, the camera pose is defined by its position, \mathbf{x}_s , which is modeled using a multivariate Gaussian distribution and its attitude \mathbf{q} , which is modeled using Bingham distribution. For an observed camera pose we can associate the joint log-likelihood $l_{att} + l_s$ where l_{att} is the log-likelihood for the attitude component and l_s is the camera position log-likelihood. A random camera attitude is associated to the rotation defined by the observed quaternion \mathbf{q} and parameterized by the line-of-sight \mathbf{v}_f . The log-likelihood for camera attitude is then given by:

$$\begin{aligned} l_{att}(\mathbf{v}_f | \Sigma_{\mathbf{a}}; \mathbf{q}) &= \ln(f_Q(\mathbf{q}; \mathbf{v}_f | \Sigma_{\mathbf{a}})) \\ &= \mathbf{q}^T \mathbf{M}_f \mathbf{C}_f \mathbf{M}_f^T \mathbf{q} - \ln F(\mathbf{C}_f) \end{aligned} \quad (3.8)$$

This formulation of l_{att} poses computational challenges and lacks smoothness in the likelihood estimation. In order to approximate the log-likelihood $l_{att}(\mathbf{v}_f | \Sigma_{\mathbf{a}}; \mathbf{q})$, which represents the likelihood of camera attitude, we introduce a practical approximation. Let $\mathbf{a}(\mathbf{q}) = (a_1, a_2, a_3)$ represent the Euler angles corresponding to the observed quaternion \mathbf{q} and $\mathbf{a}_f = (a_{f1}, a_{f2}, a_{f3})$ describe the orientation of Euler angles corresponding to the line-of-sight \mathbf{v}_f . Given that we constrained the Bingham parameters by the Eulerian covariance matrix at the attitude \mathbf{a}_f , we can write the following approximation:

$$l_{att}(\mathbf{v}_f | \Sigma_{\mathbf{a}}; \mathbf{q}) \approx -\frac{1}{2}(\mathbf{q}_f^T \mathbf{M}_a \mathbf{C}_a \mathbf{M}_a^T \mathbf{q}_f) + \text{Constant} \quad (3.9)$$

Where the couple $(\mathbf{a}(\mathbf{q}), \Sigma_{\mathbf{a}})$ is represented in terms of an orientation matrix $\mathbf{M}_a = \mathbf{M}(\mathbf{a}(\mathbf{q}), \Sigma_{\mathbf{a}})$ and a concentration matrix $\mathbf{C}_a = \mathbf{C}(\mathbf{a}(\mathbf{q}), \Sigma_{\mathbf{a}})$. The Constant term in this equation represents all parts of the log-likelihood that do not depend on the line-of-sight \mathbf{v}_f . This includes normalization factors and any terms that remain fixed when \mathbf{v}_f varies. While theoretically demonstrating this approximation is out of the scope of this paper, its validity has been verified through numerical analysis. This approximation allows a fast and smooth computation of the likelihood by encoding the line-of-sight in \mathbf{q}_f instead of the Bingham distribution parameters $\mathbf{M}_f, \mathbf{C}_f$.

The parameters \mathbf{x}_f and \mathbf{x}_s , defining the homologous point and camera positions respectively, jointly define the line-of-sight \mathbf{v}_f allowing to define the attitude likelihood as follows:

$$l_{att}(\mathbf{x}_f, \mathbf{x}_s | \Sigma_{\mathbf{a}}; \mathbf{q}) = l_{att}(\mathbf{v}_f | \Sigma_{\mathbf{a}}; \mathbf{q}) \quad (3.10)$$

If we consider the camera position log-likelihood $l_s(\mathbf{x}_s; \mathbf{x}_s, \Sigma_s) = -\frac{1}{2}(\mathbf{x}_s - \mathbf{x}_s)^T \Sigma_s^{-1}(\mathbf{x}_s - \mathbf{x}_s)$, the positional likelihood comprising of camera position and the homologous point location can be written as:

$$l(\mathbf{x}_f, \mathbf{x}_s \mid \Sigma_a; \mathbf{q}, \mathbf{x}_s, \Sigma_s) = l_{att}(\mathbf{x}_f, \mathbf{x}_s \mid \Sigma_a; \mathbf{q}) + l_s(\mathbf{x}_s; \mathbf{x}_s, \Sigma_s) \quad (3.11)$$

Note that in the positional likelihood definition, the camera location \mathbf{x}_s parameterizes the attitude likelihood jointly with \mathbf{x}_f . Assuming N independent observed lines-of-sight for a given homologous point, the multi-view positional likelihood for a homologous point which is detected in N images can be written as:

$$l(\mathbf{x}_f, \mathbf{x}_s \mid \Sigma_a; \mathbf{q}, \mathbf{x}_s, \Sigma_s) = \sum_{k=1}^N l(\mathbf{x}_f, \mathbf{x}_{s_k} \mid \Sigma_{a_k}; \mathbf{q}_k, \mathbf{x}_{s_k}, \Sigma_{s_k}) \quad (3.12)$$

2.3.2 Refracted likelihood

Let h be the true height of the WAI above the sea floor. If the homologous point is not submerged *i.e.* $[\mathbf{x}_f]_z > h$ where $[\mathbf{x}_f]_z$ is the homologous point vertical coordinate, then the previously described positional likelihood applies. However, if $[\mathbf{x}_f]_z < h$, the line-of-sight must be refracted, and the ray must be traced back from the feature point \mathbf{x}_f to the camera position \mathbf{x}_s to obtain the corresponding quaternion probability density. The refraction of the ray changes its orientation, and therefore the orientation of the quaternion density, leading to a new orientation distribution which corresponds to the refracted ray incidence point \mathbf{x}_h on the water surface. Hence, to compute the refracted likelihood, we calculate the intersection point \mathbf{x}_h of the ray from \mathbf{x}_f to \mathbf{x}_s with the WAI horizontal surface (see Figure 3.1 for camera 1). Using the Snell's law, the refracted angle can be computed as $\xi_r = \sin^{-1}\left\{\left(\frac{n_{\text{water}}}{n_{\text{air}}}\right) \sin(\xi_i)\right\}$ where ξ_i is the incidence angle in the absence of refraction, whereas n_{water} and n_{air} are the refraction indices of water and air respectively. The incidence point \mathbf{x}_h on the horizontal WAI surface is calculated as follows:

$$\mathbf{q}_{ref}(\mathbf{x}_f, \mathbf{x}_s) = \left[\sin\left(\frac{\xi_i - \xi_r}{2}\right) \cdot (\mathbf{v}_f \times \mathbf{n}_z) \quad \cos\left(\frac{\xi_i - \xi_r}{2}\right) \right] \quad (3.13)$$

$$\mathbf{v}_h(h, \mathbf{x}_f, \mathbf{x}_s) = R(\mathbf{q}_{ref}) \cdot (-\mathbf{v}_f) \quad (3.14)$$

$$\mathbf{x}_h(h, \mathbf{x}_f, \mathbf{x}_s) = \left[[\mathbf{x}_f]_x + \left(\frac{h - [\mathbf{x}_f]_z}{[\mathbf{v}_h]_z}\right) [\mathbf{v}_h]_x \quad [\mathbf{x}_f]_y + \left(\frac{h - [\mathbf{x}_f]_z}{[\mathbf{v}_h]_z}\right) [\mathbf{v}_h]_y \quad h \right] \quad (3.15)$$

where \mathbf{n}_z is the nadir vector, $\mathbf{q}_{ref}(\mathbf{x}_f, \mathbf{x}_s)$ is the quaternion representing the inverse orientation transformation required to align the opposite of $\mathbf{v}_f(\mathbf{x}_f, \mathbf{x}_s)$ with the direction of the incidence and $R(\mathbf{q}_{ref})$ is the corresponding rotation matrix. This quaternion is obtained by simply considering the angle $\xi_i - \xi_r$ necessary for aligning the opposite of \mathbf{v}_f with the incidence point \mathbf{x}_h as well as the rotation axis $\mathbf{v}_f \times \mathbf{n}_z$ (see Figure 3.1). $\mathbf{v}_h(h, \mathbf{x}_f, \mathbf{x}_s)$ represents the backward

line-of-sight in the presence of refraction, *i.e.* the transformed viewing vector accounting for the WAI height h . This vector is obtained by applying the quaternion \mathbf{q}_{ref} rotation to the opposite of \mathbf{v}_f . The equation $\mathbf{x}_h(h, \mathbf{x}_f, \mathbf{x}_s)$ computes the incidence point on the surface by combining the starting point \mathbf{x}_s with the scaled transformed viewing vector \mathbf{v}_h . The refracted likelihood which models the effect of the refraction below the WAI can then be expressed as:

$$l_{ref}(h, \mathbf{x}_f, \mathbf{x}_s \mid \Sigma_{\mathbf{a}}; \mathbf{q}) = \begin{cases} l_{att}(\mathbf{x}_f, \mathbf{x}_s \mid \Sigma_{\mathbf{a}}; \mathbf{q}) & \text{if } [\mathbf{x}_f]_z > h \\ l_{att}(\mathbf{x}_h, \mathbf{x}_s \mid \Sigma_{\mathbf{a}}; \mathbf{q}) & \text{if } [\mathbf{x}_f]_z \leq h \end{cases} \quad (3.16)$$

The full refracted likelihood that takes into account the camera position uncertainty can be written as:

$$l(h, \mathbf{x}_f, \mathbf{x}_s; \mathbf{q}, \Sigma_{\mathbf{a}}, \mathbf{x}_s, \Sigma_s) = l_{ref}(h, \mathbf{x}_f, \mathbf{x}_s \mid \Sigma_{\mathbf{a}}; \mathbf{q}) + l_s(\mathbf{x}_s; \mathbf{x}_s, \Sigma_s) \quad (3.17)$$

To calculate the refracted likelihood for a given value of \mathbf{x}_f , we use the profile likelihood, as described in the positional likelihood section. Profiling the likelihood can also be used to infer the parameter h representing the WAI height given multiple camera pose observations and multiple homologous points. With the same assumptions as in the one medium likelihood, we define the multi-view multi-point likelihood function.

$$l(h, \mathbf{x}_f, \mathbf{x}_s \mid \Sigma_{\mathbf{a}}; \mathbf{q}, \mathbf{x}_s, \Sigma_s) = \sum_{p=1}^M \sum_{k=1}^N l(h, \mathbf{x}_f^p, \mathbf{x}_{s_k}^p \mid \Sigma_{\mathbf{a}_k}^p; \mathbf{q}_k^p, \mathbf{x}_{s_k}^p, \Sigma_{s_k}^p) \quad (3.18)$$

Where indices p and k iterate over M images (camera poses) and N homologous points respectively. In this likelihood definition we assume that the water surface is at the same height h for all the homologous points and camera poses observation involved in the stereo-photogrammetric WCD problem.

For the inference of WCD, we utilized the Trust Region optimizer available in the SciPy library, a choice motivated by its efficiency in handling problems of relatively small scale. On the other hand, when inferring the WAI height, where the nuisance parameter space is significantly larger, we opted for the Adam optimizer, a gradient-based method known for its robustness in dealing with high-dimensional problems.

3 Results

In this section, we present an overview of the main results obtained from our probabilistic modeling and likelihood-based inference approach. The results are partitioned into two main

sections: WCD inference and WAI height inference. Each section focuses on different aspects of the inference process and presents the corresponding findings and evaluations.

3.1 Experimental setup

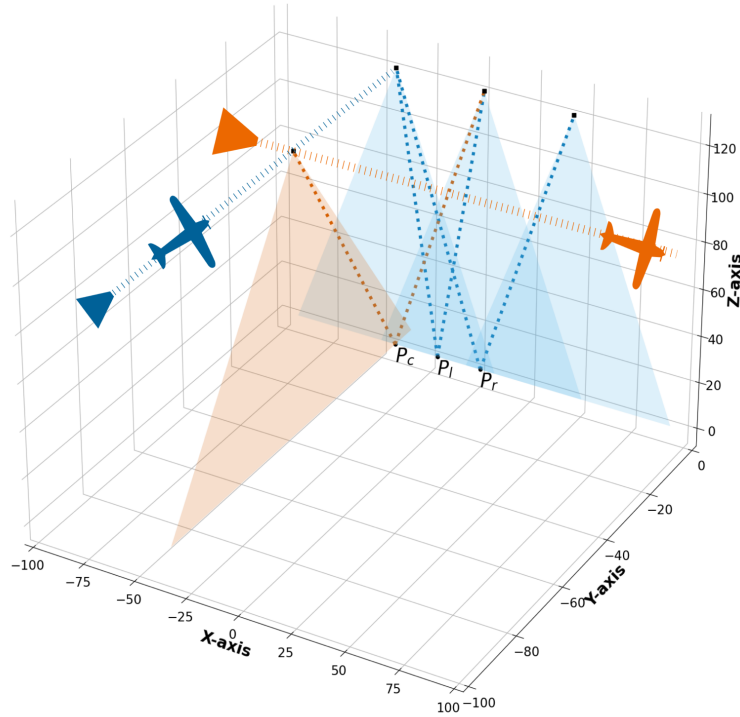


Figure 3.4 – Geometric configurations for drone scenario for a FoV of 48° and an overlapping of 60%.

The experimental setup for this study is designed to evaluate the performance of the proposed method for pushbroom camera acquisition under various flight scenarios, encompassing both airborne and drone operations. The airborne scenario simulates an altitude of 2000 meters, reflecting typical conditions for aircraft-based remote sensing missions, while the drone scenario simulates a lower altitude of 120 meters, indicative of low-altitude drone surveys.

Figure 3.4 illustrates the camera positions (black squares) and their respective scanned FoV (blue and orange triangles) for the drone scenario. We use a FoV of 48° , a relatively extreme value to challenge our approach. To ensure comparability and consistency, the same base-height ratio determined for along-flight directions (determined by the 60% overlap constraint) is transposed to the single across-flight trajectory used for the P_c scenario. This setup maintains a consistent geometric configuration across different orientations.

In the experimental setup, various viewing geometries were simulated to evaluate the performance of the proposed method. Table 3.1 presents these viewing geometries which are

Table 3.1 – Base-Height ratios for homologous points for both drone and airborne scenarios

Homologous Point	Base-Height Ratio (B/H)	Viewing Scenario
P_c	0.36	Crossing lines
P_l	0.36	Parallel lines
P_r	0.72	Parallel lines

Table 3.2 – Experimental setup classes with camera pose noise metrics in terms of standard deviation. The position noise corresponds to standard deviations combined for the planar and vertical precisions. The attitude noise is expressed as roll/pitch-yaw where the first value is associated to both roll and pitch precisions while the second value is related to the yaw precision.

Camera pose quality	Position noise	Attitude noise	
		Pitch/Roll	Heading
Fair	.5 m	.1°	1°
Good	0.05 m	.01°	0.1°
Excellent	0.05 m	0.01°	0.01°

determined by homologous points P_r , P_l and P_c . Table 3.2 presents the simulated INS classes defining camera pose quality metrics in terms of standard deviation.

Each experiment class represents a different level of camera pose quality. Both for the drone and the airborne experiments, three levels of camera pose quality were considered: "Fair", "Good", and "Excellent". The positional accuracy ranges from .5 meters for the Fair class to 0.05 meters for the "Good" and "Excellent" classes. In our simulations, the precision of the camera's attitude is modeled with distinct values for roll/pitch and yaw . Specifically, for the 'Fair' class, we use 0.1 degrees for roll/pitch precision and 1 degree for yaw precision. For the 'Good' class, the precision is set at 0.01 degrees for roll/pitch and 0.1 degrees for yaw . Lastly, the 'Excellent' class is characterized by a uniform precision of 0.01 degrees for both roll/pitch and yaw .

To assess the robustness and reliability of the proposed methodology, we perform Monte Carlo simulations by generating synthetic datasets around a true parameter value. A true attitude value of $\tilde{\mathbf{a}} = (0, 0, 0)$ and a fixed covariance matrix $\Sigma_{\mathbf{a}}$ were considered for the attitude while the true camera positions were simply set to the simulated locations. These simulations involve generating a large number of synthetic data sets represented by random orientation and concentration matrices $\mathbf{M}_a, \mathbf{C}_a$, as well as random camera positions \mathbf{x}_s , each with different levels of noise. The results of the simulations are used to evaluate the performance of the methodology and to analyze both the WCD and WAI height uncertainties in terms of 95% CI under different conditions.

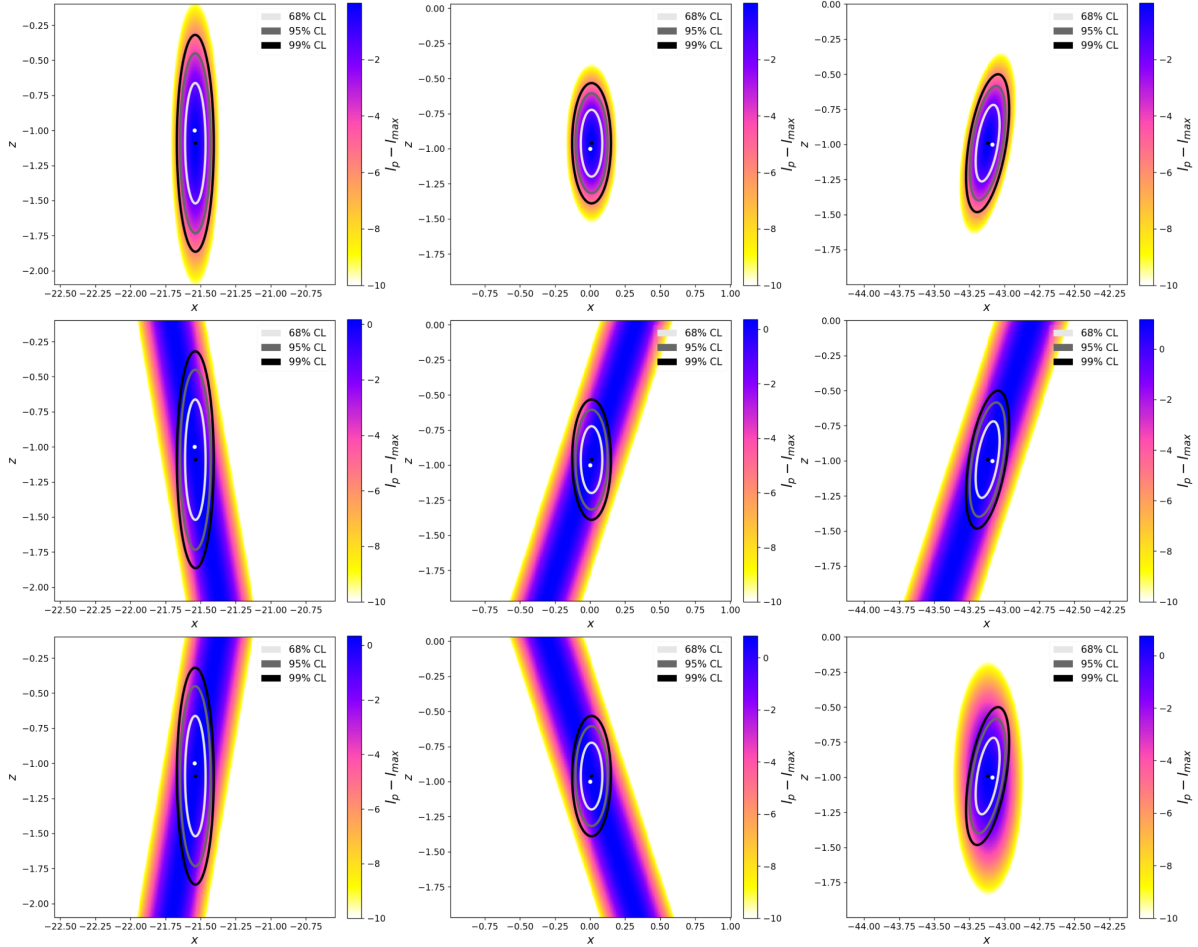


Figure 3.5 – Normalized profile likelihood $l_p(\mathbf{x}_f; \mathbf{y}) - l_p(\hat{\mathbf{x}}_f; \mathbf{y})$ (noted with $l_p - l_{max}$ as a shortcut) surfaces for the drone case and a "Excellent" INS with confidence regions using the multidimensional likelihood ratio statistic for the parameter \mathbf{x}_f . The first row displays the combined profile likelihood, representing the sum of the likelihoods from both left (second row) and right camera (third row) perspectives. Left, middle and right columns are for points P_l , P_r , P_c respectively. The white dot represents the true homologous position $\hat{\mathbf{x}}_f$, while the black dot represents the maximum likelihood estimate $\hat{\mathbf{x}}_f$.

3.2 Water Column Depth inference

In this section, we consider the WCD inference in the through water context, assuming that the water air interface height is known and fixed at $h = 0$.

3.2.1 Water Column Depth Uncertainties

Figure 3.5 provides a graphical representation of the normalized profile likelihood surfaces for the three points: P_l , P_r , and P_c , specifically for the drone case. Each plot corresponds to a

planar cut along the yz -plane of the 3D multi-view likelihood profiled along the interest parameter x_f , displaying the confidence regions obtained using the multidimensional likelihood ratio statistic with a degree of freedom of 3. We observe that the uncertainties for P_l are generally higher compared to P_r and P_c with a factor of 2 between P_l and P_r uncertainties. In the one-medium photogrammetry, as it is known, the vertical uncertainty is proportional to the base height ratio. Additionally, the point P_c , which is viewed by perpendicular lines, exhibits non vertical uncertainty ellipses mainly because the line-of-sights are not co-planar as suggested by the difference in camera contribution to the 3D likelihood in the yz -plane as highlighted by Figure 3.5 for point P_c . Analyzing the uncertainty ellipses within the experiment classes present in Table 3.2, our results indicate that the WCD uncertainty shape is not heavily influenced by the depth factor.

Focusing on the WCD as a parameter of interest, we can further examine its uncertainties based on t_o statistic using Monte Carlo simulations (as shown in Figure 3.6). The plot in Figure 3.6 provides a comparative analysis of the WCD uncertainty in terms of 95% CI widths along with error bars representing the standard deviation of these intervals.

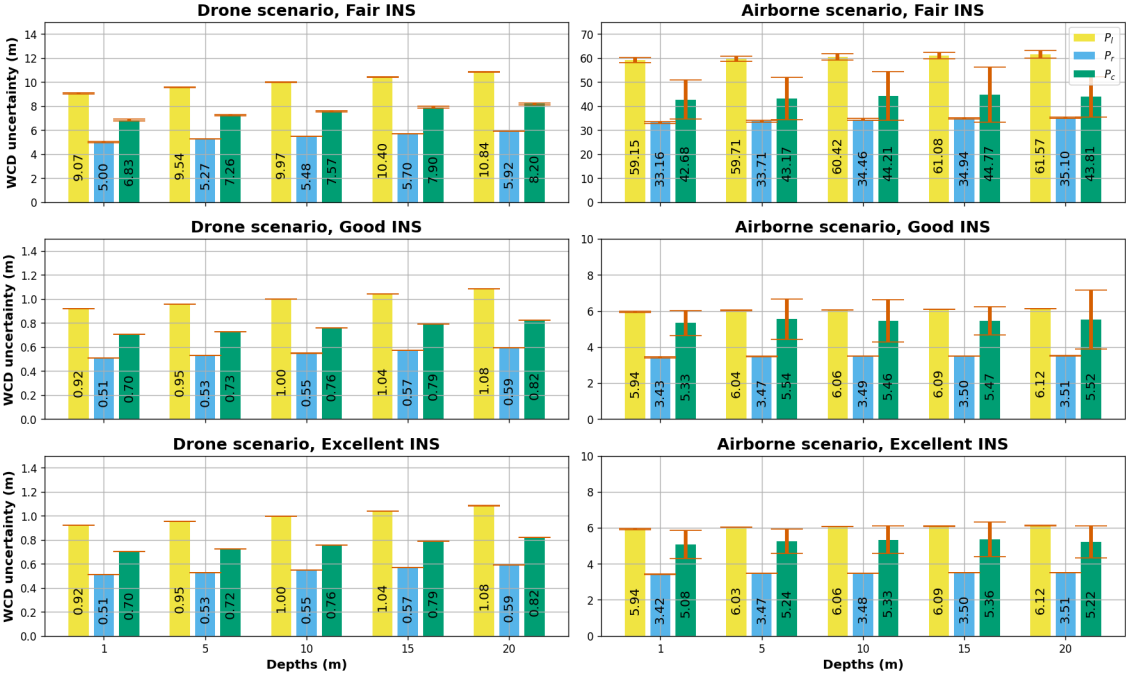


Figure 3.6 – WCD uncertainties based on 95% confidence intervals ($\pm 2\sigma$) reported by the Observed Fisher Information test statistic t_o for different scenarios (namely different viewing configurations P_l , P_r , P_c , different INS classes, different depths).

Overall, the impact of depth on the uncertainty of WCD is less significant than the other viewing geometries. However, there is a slight increase in uncertainty as the depth increases especially in the drone scenario, with 15% uncertainty increase from 1 meter to 20 meters depth vs 3% uncertainty increase in the airborne scenarios. This is mainly due to the fact that

base height ratio decreases as the depth of the simulated homologous point increases, which generates an elongation of uncertainty ellipses. In terms of camera pose quality, both the "Excellent" INS and "Good" INS scenarios demonstrate relatively low and similar uncertainty values (50 cm to 1 m in the drone case and 3 m to 6m in the airborne case), with similar trends observed across different points. This indicates that increasing yaw precision does not necessarily lead to a more precise WCD estimation given the defined viewing geometries. Yaw rotation has a minimal effect on vectors which are close to the nadir suggesting that the interior orientation vectors \mathbf{v}_s are not influenced by yaw precision even with a high FoV and for large base height ratio points. On the other hand, the "Fair" INS class exhibits larger WCD uncertainties (factor of 10) with higher variability in the obtained WCD uncertainty. The airborne observations generally result in larger confidence regions and higher WCD uncertainties compared to the drone scenario. An increased distance for the homologous rays results in an increased dilution of the attitude uncertainty and therefore larger uncertainties are to be expected for higher flight altitudes.

Our results suggest that uncertainties in the airborne scenario are approximately six times greater than those in the drone scenario, despite a flight altitude ratio of 16:1 (2000 m for airborne versus 120 m for drone). Crucially, our study maintains consistent key parameters such as base-height ratio, FoV, and image overlap across both scenarios. In a purely geometric interpretation without probabilistic modeling, one might expect uncertainties to scale proportionally with flight altitude. In this regard, our findings indicate a statistical reduction in vertical uncertainty due to the intersection of two lines of sight, which is indicated in Figure 3.5 by the intersection likelihood compared to the single line-of-sight likelihood. We hypothesize that this effect increases with the altitude elucidating why increased distances in the airborne scenario do not linearly translate into increased uncertainty, highlighting the influence of probabilistic modeling in the variability of vertical uncertainties between different flight altitudes.

Regarding the viewing geometry influence, WCD uncertainties for both drone and airborne scenarios follow a similar order (increasing from P_r to P_c to P_l) and show comparable patterns of variability. Interestingly, the uncertainties for point P_c (viewed by cross lines) exhibit high variability, especially in the airborne flight and the "Fair" INS case. In such a scenario, this increased variability of the uncertainty estimates for point P_c can be attributed to the unique interplay between its viewing geometry and the anisotropic attitude noise with low concentration in the "Fair" INS case. The viewing geometry of P_c inherently results in intersecting lines-of-sight but the sampled lines-of-sight, in the "Fair" INS class and high altitude airborne flight, results in greater variability in the positional likelihood near the MLE. This, coupled with the effect of refraction, can account for this pronounced variability in the WCD uncertainty estimates for P_c viewing geometry.

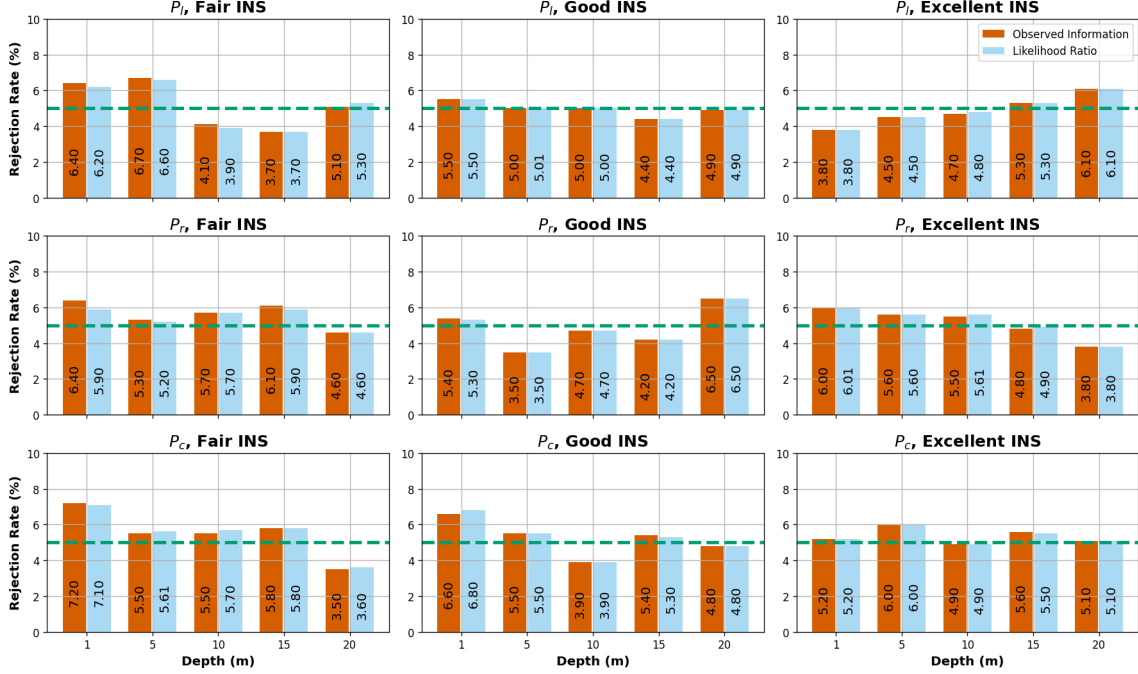


Figure 3.7 – Drone scenarios: rejection rates of the t_o Wald statistic (Observed Fisher Information) and the signed likelihood ratio statistic r . The x-axis represents different simulated depths, while the y-axis represents the rejection rate percentage based on a confidence level of 95%. The green dashed horizontal line indicates the 5% rejection rate threshold.

3.2.2 Evaluation of uncertainty metrics

In this section, we present the results of our likelihood-based inference approach for estimating the WCD uncertainty using the t_o and r test statistics. The rejection rates of the null hypothesis (True parameter value) were calculated through Monte Carlo simulations, employing a significance threshold of $\alpha = 0.05$.

Figure 3.7 displays the rejection rates for various combinations of INS performances, depths, and viewing geometries in the drone scenarios. The statistical tests revealed a strong correlation among the samples, with rejection rates consistently aligning closely with the theoretical rejection rate of 5%, ranging from 3.5% to 7.0%. These findings indicate that both the t_o and r test statistics are appropriate for estimating 95% CI for the WCD parameter. The observed correlation suggests that the WCD uncertainties are symmetric in the drone scenarios. Although the expected Fisher information was not investigated in this study, the low variability of the uncertainties in most cases (orange error bars in Figure 3.6), indicates that it would have yielded similar results and performance to the Observed Fisher Information.

For the airborne scenarios, we observed a similar performance of the test statistics, except for point P_c , which showed distinct rejection rates, as illustrated in Figure 3.8.

Specifically, for the "Fair" INS scenario, the rejection rates for the t_o test statistic exceeded

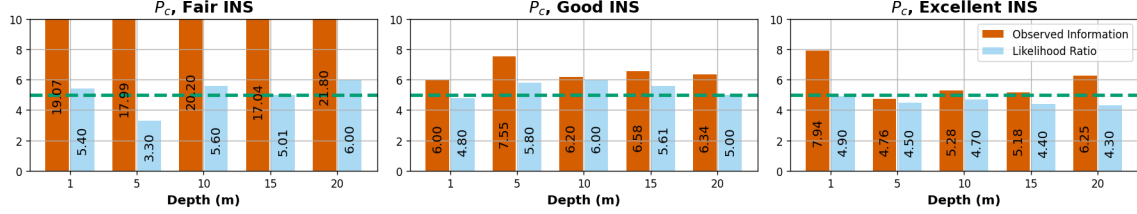


Figure 3.8 – Airborne scenarios: rejection rates of the t_o Wald statistic (Observed Fisher Information) and the signed likelihood ratio statistic r . The x-axis represents different depths, while the y-axis represents the rejection rate percentage based on a confidence level of 95%. The green dashed horizontal line indicates the 5% rejection rate threshold.

15% at point P_c , while the r statistic demonstrated relatively consistent rejection rates across different depths (3.5%-7%). Given the WCD uncertainty results of P_c , highlighted in the previous section, we can infer that the higher variability in the WCD uncertainty estimates for P_c in the previous subsection is consistent with the observed rejection rates. These findings suggest that the t_o -based CI may lead to an overestimation of WCD uncertainty in high altitude scenarios. This is particularly the case for viewing geometries similar to P_c with a 19% rejection rate for the most noisy attitude scenario. On the other hand, the r statistic showed greater effectiveness in estimating the WCD uncertainties in this particular case (P_c and airborne "Fair" INS).

In summary, the evaluation of uncertainty metrics through rejection rate analysis provides valuable insights into the reliability of uncertainty estimation methods for both the drone and airborne cases. Both scenarios exhibit reasonably consistent performance, except under extreme attitude noise and non-parallel lines viewing geometries.

3.3 Water Air Interface height inference

In our experimental setup, we sought to present the profile likelihood of h under multi-point and multi-view likelihood scenarios. To begin with, we need to clarify the conditions under which the WAI height is inferable from camera poses. Primarily, when the lines-of-sight are derived from parallel lines (*i.e.* P_l or P_r viewing geometry), or have equal incidence angles (*i.e.* P_c viewing geometry), the the lines-of-sight having the maximum likelihood will always intersect, irrespective of the value of WAI height. In these cases, the parameter h cannot be inferred because it has no influence on the likelihood. In contrast, when the lines-of-sight are non-coplanar with the baseline [46], then the lines-of-sight having the maximum likelihood will not intersect unless they are refracted under an optimal value of the WAI height parameter. This distinct viewing geometry can be readily obtained by introducing different incidence angles in the simulated lines-of-sight, allowing for the inference of the parameter h through the profile likelihood analysis. Either translating the same points (P_c , P_l and P_r) or introducing different flight altitudes provide viewing geometries with different incidence

angles. In our setup, points P_l , P_r and P_c are translated along both x and y dimensions, with different offsets δ_x and δ_y respectively. For drone simulations, $\delta_x = 5m$ and $\delta_y = 10m$, whereas for the airborne scenarios, these offsets are scaled by the altitude ratio. Applying these adjustments, we use the likelihood 3.18 for the WAI height parameter h inference with a WAI height true value of $\tilde{h} = 0$, for varying sample sizes, namely 1, 10, 100, 1000, 10000. Each sample refers to a couple of measured camera poses for a single homologous point given the refraction at \tilde{h} . This means that for n samples, the parameter is of dimension $9 * n + 1$ (1 for h , $3n$ for \mathbf{x}_f and $6n$ for \mathbf{x}_s).

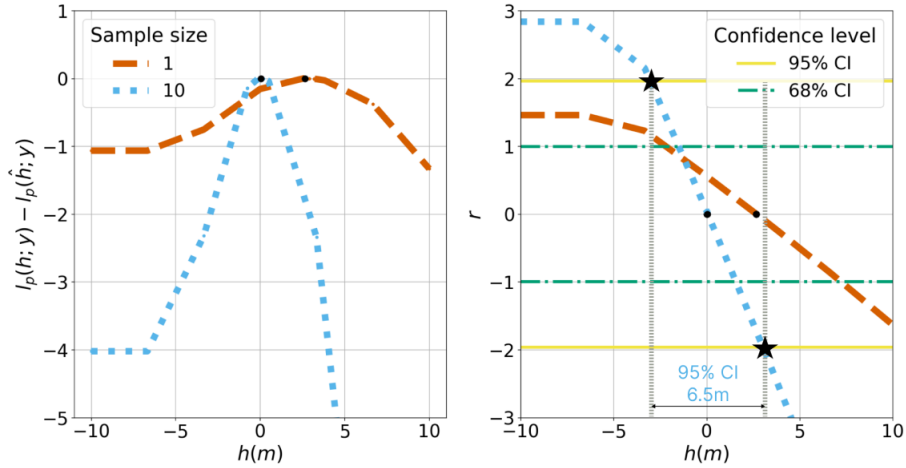


Figure 3.9 – Drone and "Excellent" INS scenario: WAI height inference based on Likelihood profiling for 1 and 10 samples. The graphic on the left represents the normalized profile likelihood on the y-axis according to the WAI height on the x-axis. The graphic on the right represents the r statistic on the y-axis according to the WAI height on the x-axis. The black points correspond to the WAI height MLE \hat{h} . Additionally, on the right side, the 95% CI for 10 samples are indicated as the width between the intersections (marked by black stars) of the r statistic curve and the 95% confidence critical values ± 1.96 .

Figure 3.9 shows on the left side WAI height normalized profile likelihood obtained for the translated point P_c , at a depth of 5 meters and for two sample sizes: 1 and 10. The associated r statistic is presented on the right side of the figure with the CI for two levels, namely 95% and 68%. According to the profile involving only one sample, (orange profile), two non-intersecting lines-of-sight can provide an optimal value for the WAI height parameter h . For both 1 sample and 10 samples profiles, we observe a typical asymmetry in the profile which is characterized by a flatness on the left side (below 5 meters depth). This pattern can be mainly attributed to the fact that when the WAI is relatively below the WCD for a given homologous point, the positional likelihood should not decrease with the WAI height since there is no refraction above the WAI. The r statistic, affected by this flatness, successfully captures this asymmetry, which results in a non-identifiable 95% lower bound of CI for the 1 sample inference although we could delineate 68% CI. On the other hand, 10 samples provided sufficient statistical information for delineating both 95% bounds for the WAI height h . However, based on the r 95% CI, the achieved precision of approximately 6.5 m for 10 samples is notably high.

Therefore, it would be valuable to explore the possible improvement in WAI uncertainty when larger sample sizes are taken into account.

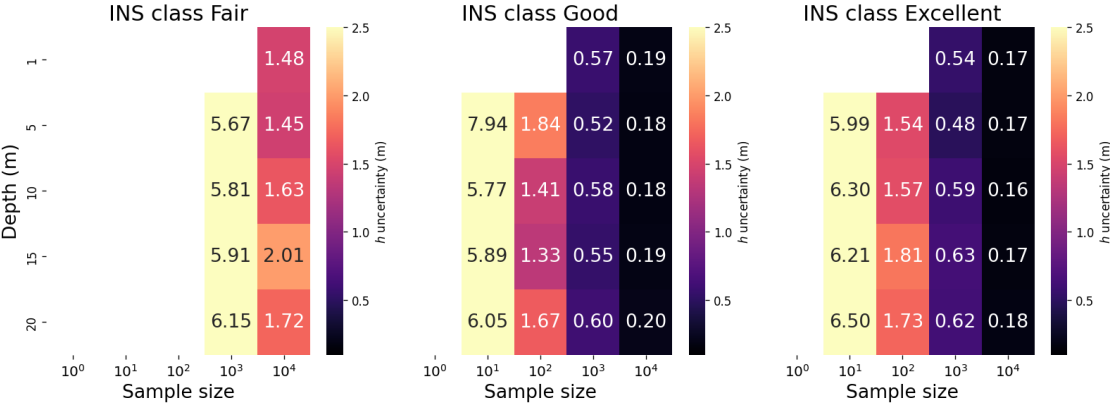


Figure 3.10 – Drone, P_c scenarios, WAI height uncertainty across different INS classes as reported r statistic CI. Missing bins indicate non identifiable 95% CI.

Figure 3.10 presents heatmaps of WAI height uncertainties, determined by r CI for point P_c across different INS classes for the drone scenario. These heatmaps account for a variety of depths and sample sizes. As the sample sizes increased, so did the statistical information, leading to more precise profile likelihoods and subsequently, smaller uncertainties in the WAI height. Interestingly, a trend of uncertainty decreasing by a factor between 3 and $\sqrt{10}$ has been noted. This pattern, where uncertainty contracts in relation to the square root of the sample size (\sqrt{n}), echoes the square-root law common in Gaussian errors and is linked to the Central Limit Theorem’s principle of sample averages approaching a normal distribution as the sample size expands, leading to decreased uncertainty. Analogously to the WCD inference, the "Good" and "Excellent" INS demonstrated similar performances. Intriguingly, the depth has no major impact on the WAI uncertainties except for the observed lag of the 1 meter depth scenario with sample size compared to other depths. This insinuates that the task of WAI inference tends to be more difficult when it relies on observations taken at depths near the WAI surface.

In Figure 3.11, we display the depth-averaged WAI uncertainties, together with their corresponding standard deviations, spanning viewing geometries, INS classes and sample sizes, for both drone and airborne settings. It’s often the case that the variability of WAI uncertainty with depth, as indicated by error bars, is more pronounced in difficult scenarios (10 samples). For the WAI height inference, the viewing geometry P_c showed the best performance overall, suggesting that cross lines are strongly relevant in pushbroom acquisitions if one is interested in inferring the WAI height. It is particularly noteworthy that the achieved WAI height 95% CI of 17 cm and 19 cm for 'Excellent' and 'Good' quality INS, respectively, closely aligns with the GNSS precision of 5 cm, when considering a substantial sample size of 10,000. This suggests that with relatively small high resolution data sets, drone-based acquisitions can

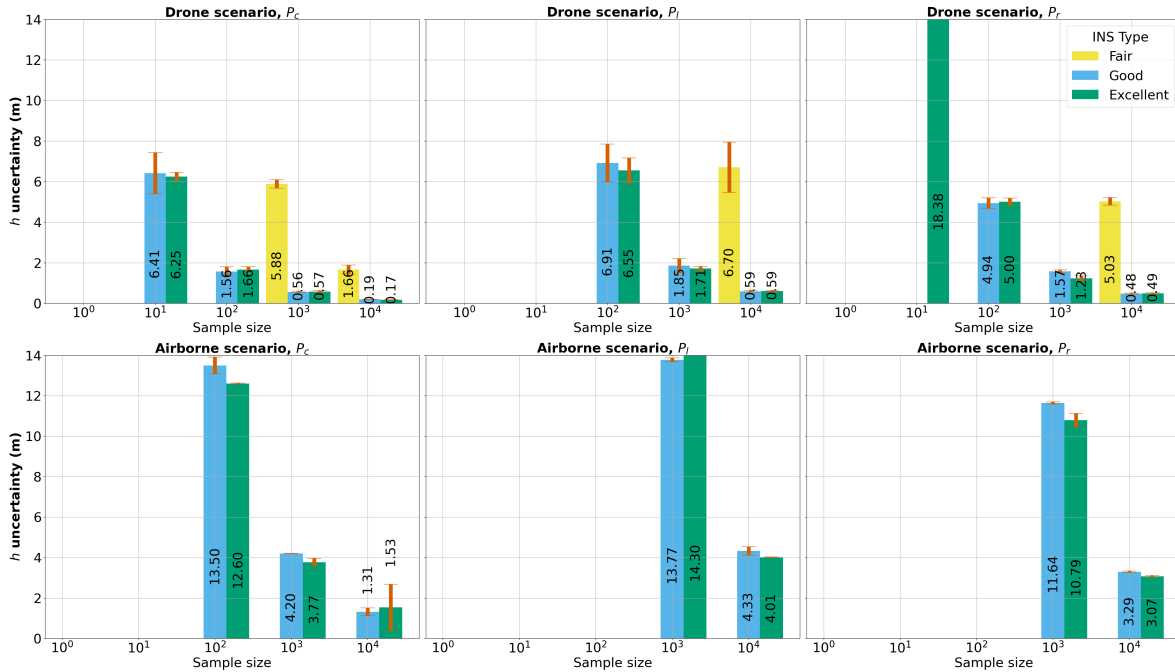


Figure 3.11 – Depth averaged WAI height uncertainty across Different INS types and sample sizes for each point as reported by r statistic CI. Missing bars correspond to non identifiable 95% CI for all the averaged depths. The numerical values displayed on each bar correspond to the depth-averaged WAI height visually represented. The error bars represent the standard deviation of WAI height uncertainty across the different depths.

provide significantly accurate estimations of the WAI height in optically clear shallow waters with a textured seabed. Furthermore, considering the decline in uncertainties by a factor of \sqrt{n} with increasing sample size, even with the "Fair" INS quality, we extrapolate that drone flights could achieve a WAI height precision of 16 cm given a sample size of about 1 million. Although 1 million matched homologous points may seem substantial for a single survey of pushbroom imagery in coastal areas, given constraints like water clarity and a textured seabed, such a number of points is easily attainable with high-resolution frame video imagery under optimal conditions. This emphasizes the efficiency of drone-based acquisitions even with less-than-ideal INS quality, given an adequately large data set of paired homologous points.

In contrast, airborne measurements yield a higher degree of uncertainty in WAI estimation with no successful inference for the "Fair" INS. Similarly to the WCD inference results, this is largely attributed to the increased operational altitude that intensifies optical distortion and viewing geometry variability due to a more distant and extensive footprint. Despite these challenges, airborne measurements with high quality INS achieve a metric precision for a 10,000 sample size, allowing to extrapolate a centimeter precision level for a 1 million sample size.

4 Discussion

The proposed study highlights the significant role of the camera pose quality on the WCD uncertainty. The "Excellent" INS class, typically deemed a high standard in hydrography, did not achieve satisfactory WCD precision (around 2 m) for airborne flights. This discrepancy underlines the advantages of drone-based surveys operating at lower altitudes with high quality camera pose measurements, which provided high WCD precisions, specifically around 50 cm for high base height ratios like P_r . According to IHO standards [12], this precision level falls within the 'Order 1a' requirements without taking account of depth influence. However, the inherent limitations of higher base-height ratios and low flight altitudes, such as reduced and inefficient coverage, need to be considered. In contrast, for points P_l and P_c , the uncertainty ranged between .7-1m, meeting the requirements of the 'Order 2'. Furthermore, we state that combining frame and pushbroom imagery could further improve camera pose quality for high altitude flights. Indeed, our geometric likelihood approach enables through water photogrammetry bundle adjustment, presenting the opportunity to utilize frame imagery and decrease camera pose uncertainty. While our study provides key insights into camera pose uncertainties in through water photogrammetry, it is important to note a limitation in our experimental design concerning multi-view geometry principles. Specifically, our experiments did not accommodate the principle of utilizing overlaps in both across and along flight directions, a common approach in multi-view geometry to augment camera pose samples and reduce uncertainty in triangulation. Our focus was on maintaining a uniform analysis across two camera poses in order to directly compare the effects of stereo geometry. This approach is also appropriate given that pushbroom studies often rely on stereo-pair configurations, where extensive cross-line datasets are very limited.

As we focused on pushbroom geometric scenarios in our study, we only investigated two camera poses for triangulation, and we hypothesize that having an adequate number of homologous points for each camera pose can refine the pose and eliminate the reliance on challenging-to-obtain GCP in coastal areas. Such advancements in camera pose quality have the potential to significantly enhance the precision levels of drone observations, potentially meeting stringent standards like the Special order in clear shallow waters with textured seabeds.

Furthermore, based on the WCD uncertainty results, the Observed Fisher Information performance and its low sensitivity to sampling suggest that classical variance-covariance propagation approaches, are reliable except for certain challenging scenarios. These include high flight altitudes, low quality camera pose measurements, and viewing geometries with non coplanar FoVs (P_c case). These viewing geometries are more prevalent in frame imagery since the spatial footprint in frame imagery is rectangular, thus establishing the likelihood ratio statistic as a potential tool for robust uncertainty estimation in such scenarios.

Beyond the evaluated uncertainties, it's worth emphasizing that our results contribute to a deeper understanding of photogrammetric techniques for coastal photogrammetric surveying. The ability to accurately infer the water surface position from imagery alone reduces the reliance on additional tide data or separate WAI height observations. Although our initial assumptions considered a horizontal water surface, not accounting for surface fluctuations, the results showed satisfactory precision of around 17 cm when using large samples and non-intersecting viewing geometries. This precision level is particularly impressive considering calm sea conditions and light weather situations, which can be encountered in sheltered area with low significant wave heights. Nonetheless, it's important to consider that in a real-world scenario, coastal waters fluctuations could occur due to a range of factors such as changes in tide and weather, which may influence the temporal coherence of the imagery dataset. This consideration indicates that our approach can be further improved by taking into account these potential fluctuations. For instance, simulations of wave spectra and sea state conditions can be used to create more realistic scenarios, offering a comprehensive perspective on the influence of surface fluctuations on WAI height uncertainties and their subsequent impact on the derived bathymetric estimations. The noted viewing geometry condition for WAI height inference might favor in-track more than across-track satellite stereo pairs which often have the same incidence angles. Therefore, a continuation of this study would be extending the investigation of the effect of viewing geometry and proposing appropriate flight acquisition modes for WAI height inference. Also, the performance of r CI that we utilized to estimate uncertainties in WAI height were not assessed through hypothesis testing, in contrast to what we performed for the WCD. This examination was out of the scope of this study and therefore, could serve as a potential area for further investigation and research. Moreover, our approach for WAI inference can be effectively adapted with stationary high-quality stereo camera observations as a technique for tide monitoring.

The results also invite a deeper examination of innovative uncertainty modeling methods. Such methods can be beneficial in harmonizing the geometric inference of WCD with other forms of inference like radiometric estimation with analytical radiative transfer models, within a unified theoretical likelihood framework as explored by [15; 99]. Interestingly, the relative insensitivity of the geometric inference to depth variations, which contrasts with its radiometric counterpart as suggested by these studies, indicates potential complementarity between the geometric and radiometric inference. However, it's important to recognize that both approaches, geometric and radiometric, require a degree of optical water clarity. Therefore, the impact of depth can introduce inherent constraints on both types of inferences, especially in environments with turbid waters.

Our study is a robust step forward in uncertainty modeling for bathymetric photogrammetry in coastal shallow waters and has unveiled several insights. The main focus of our study is the investigation of camera pose uncertainties in through water photogrammetry. However,

it is important to acknowledge that uncertainties may arise from additional sources, such as matching errors, camera imperfections and wave dynamics, which are significant factors in coastal waters imagery.

5 Conclusion

This study represents a detailed exploration of the potential and accuracy of through water photogrammetry, with a specific emphasis on WCD and WAI height inferences. Our observations reveal the profound influence of viewing geometry and camera pose quality on the resulting uncertainties, overshadowing the impact of depth.

Our approach bridges the gap between advanced probabilistic modeling and stereo-photogrammetric triangulation. This innovative integration provides a comprehensive understanding of the complexities associated with through water 3D reconstruction methods. The utility of drone technology, complemented by high quality camera pose measurement and spectral imagery, proves to be a compelling tool for high-precision through water photogrammetry. Importantly, these advancements contribute to the provision of a framework for through water photogrammetry predictive uncertainties. Additionally, we demonstrate that inferring the water surface elevation is achievable from camera pose measurements reducing the dependence on auxiliary data sources such as tide level measurements or WAI height observations.

Notwithstanding the success of our investigations, we acknowledge the limitations of our current study. Specifically, the questions related to providing compelling recommendations for viewing geometries and hypothesis testing for WAI height, requiring further exploration and elucidation.

Chapter 4

Likelihood-based Inference for Bathymetric Uncertainties in Semi-Analytical Models

In Chapter 4, we extend the foundational theories of statistical inference outlined in Chapter 2 and build upon the applications discussed in Chapter 3. This chapter delves into the complexities of applying likelihood-based first-order methods to semi-analytical models for inferring WCD through radiometric data, as well as exploring second-order adjustments to address the challenges posed by numerous nuisance parameters and inherent variability of coastal spectral imagery data.

Initially, the chapter reviews related works to contextualize advancements in SA models for bathymetric mapping, identifying gaps our approach aims to fill. Methodology is articulated next, outlining the statistical techniques underpinning the theoretical framework of likelihood and the Monte Carlo simulations employed for evaluating the robustness of asymptotic CI.

Comprehensive analysis of findings is presented in the results section, showcasing empirical validation of the likelihood framework's statistical tests for evaluating WCD uncertainties. Subsequent discussion evaluates these findings within the broader context of bathymetric mapping, reflecting on the implications for environmental monitoring practices and the limitations of current statistical methods.

The chapter concludes by summarizing our contributions and reflecting on the impact of this research on SA models for bathymetric estimation.

1 Related works

In this section, we straightforwardly focus on SA models since they are computationally practical for inversion while ensuring the physical interpretability of RT approaches and providing the ability to conduct parametric inference of environmental parameters. These advantages favors them over empirical approaches which are inherently predictive. Indeed, [7] evaluated uncertainty when derived with empirical models and highlighted its sensitivity to a range of factors, including optical conditions of the water column and the number of spectral images used. This suggests that empirical approaches may not be robust across varying datasets and environmental conditions, and may require extensive calibration. Having explored the complexities of sensor and AC in Section 2.3, it becomes imperative to understand how the associated uncertainties propagate through SA models to influence the estimated WCD. In the context of SA models, which typically use R_{rs} as an input, R_{rs} uncertainties have a direct impact on the estimated environmental parameters. Understanding its uncertainties is fundamental, as these directly translate into variances in the estimated environmental parameters including WCD. Consequently, uncertainty evaluation methods for the R_{rs} quantity will be reviewed first before addressing prior works on the WCD.

1.1 R_{rs} uncertainty evaluation

In the radiometric estimation, sensor noise and environmental factors introduce a layer of complexity that cannot be ignored [44; 8]. Sensor noise, which includes factors like photon, dark current, and digitization noise, affects the reliability of the estimated parameters. Environmental factors such as atmospheric and sunglint effects in spectral imagery add another layer of uncertainty. Methods for estimating uncertainties in R_{rs} fall into three primary categories: empirical, scene-based, and pixel-based approaches. Empirical methods, such as those by [100; 101], compare satellite data to a "ground truth" in order to provide a general sense of sensor performance across various environmental conditions. These methods often reveal that atmospheric correction has a more significant impact on R_{rs} uncertainty than sensor calibration, especially in complex coastal regions. Scene-based approaches introduce the metric of Noise Equivalent Reflectance Difference (NE Δ R) [43; 102; 103]. This metric quantifies R_{rs} uncertainty by considering both sensor noise and environmental factors, without requiring detailed sensor noise modeling. However, its application can be limited in optically shallow waters where environmental conditions are variable [104; 15; 105; 8; 106]. Pixel-based methods, such as those developed in [107; 108; 109], aim for a more granular estimation by propagating sensor uncertainties through AC and sun glint correction at the pixel level. Despite their sophistication, these pixel-based radiative transfer methods are limited by predetermined aerosol models and an invariant Lambertian characterization of the surface

1.2 WCD uncertainty in Semi-Analytical models

Bootstrapping has been employed to estimate the distribution of estimates in order to capture the derived distribution of SA model parameters [110; 8]. Although straightforward, bootstrapping remains less suited for large datasets and real-time applications due to the resampling and the additional required inversions. Furthermore, the evaluation of uncertainties derived from bootstrapping techniques in the context of iteratively optimized SA models has not been explicitly explored. Such challenge is arguably computational because a thorough analysis requires a robust performance of the optimizer used for bootstrapping in this context. Due to the nonlinear nature of SA models, both classically used local optimizers and bootstrapping are most susceptible to dramatically fail in low statistical information scenarios (low SNR, deep waters, complex IOP) as reported in previous studies [32; 8].

To the best of our knowledge, research on classical error propagation, such as prescribed by the GUM, in shallow water SA models has not been explicitly addressed. In his works on spectral imagery products uncertainty in shallow waters, [8] highlighted the difficulty of extending variance-covariance error propagation to the settings of shallow waters SA models. On the other hand, variance-covariance error propagation has been applied in the context of ocean color SA models which are relatively simpler (optically deep waters) where WCD and seabed features are excluded [111; 112; 113]. However, [114; 115] demonstrated that these models suffer from ill-posedness and ambiguity issues which can have a significant impact on uncertainty evaluation through variance-covariance framework. The challenges with ill-posedness and ambiguity faced by ocean color SA models, already simplified by excluding WCD and seabed features, indicate that these issues could be even more significant in the complex settings of shallow water SA models. This enhancement of issues underscores the inherent difficulties in executing error propagation methods within these settings. The majority of the research in this field suggests that the transition to hyperspectral data could potentially alleviate some of these issues, although similar challenges can arise in low SNR hyperspectral measurements [30; 116]. [117] analyzed the ability of SA models to estimate WCD using hyperspectral data, and found robust behavior in terms of WCD identifiability when evaluated through a global optimization technique. Although this behavior was demonstrated at predefined parameterizations, this indicates that the encountered issues of ambiguity and ill-posedness are stemming from noise consideration and from the model structure. This converges with the broader debate on structural identifiability versus practical identifiability, with the latter being crucial for uncertainty assessment [118; 119; 77]. Practical identifiability, especially in scenarios with small sample sizes, often leads to asymmetric CI. The main issue with practical identifiability arises from the difficulty in determining precise lower or

upper confidence limits, which directly affects the certainty of parameter estimates. In an earlier work related to this manuscript [99], we illustrated how profiling likelihood, whose principles are presented in Section 4.2.1 of Chapter 2, is an effective tool for identifying such problems, highlighting the importance of thoroughly exploring first-order methods (such as Wald tests, likelihood ratios, and the score method) to address the inherent challenges faced by SA models.

Within the likelihood framework, an equivalent study to variance-covariance propagation would be [15] who employed EFIM for predicting SA models parameters uncertainty in shallow waters under additive Gaussian noise (see Sections 1.1 and 2 on this equivalence). This study demonstrated the feasibility of analytically tracking WCD uncertainties in SA models for both hyperspectral and multispectral data, reporting higher uncertainty predictions typically for multispectral bands and optically complex waters. [120] extended this line of research by introducing prior information in the computation of EFIM uncertainty for hyperspectral data. This was motivated by the argument of information introduced by bounded optimization, which is often used in practice in order to obtain robust estimations in optically complex waters. Arguably, uniform priors are equivalent to restricted MLE whereas introducing Gaussian priors may potentially yield optimistic confidence bounds, especially if one takes into account the fast-decaying tails of the Gaussian distribution. In addition, taking into account the variability of water column conditions in coastal waters, establishing priors can be difficult and may fail in applications requiring objective and reliable measurements such as shallow waters bathymetric mapping. The propagation of these uncertainties through SA models, therefore, becomes a focal point of this chapter, aiming to provide a comprehensive understanding of the limitations and potentials in remotely sensed shallow water bathymetry uncertainties. Building on the Cramér-Rao bound explored by [15], our aim is to assess the performance of the first-order and higher order asymptotic inferences in the context of shallow waters SA models. Unlike most of studies which primarily focused on the variance-covariance of the MLE in SA models, the current work rigorously evaluates the MLE in terms of CI performance with Monte Carlo simulations. This nuanced analysis is particularly relevant for small samples settings such as multispectral measurements and turbid waters, where the statistical information concerning WCD is often not as rich as in hyperspectral configurations and clear waters.

2 Methodology

In our study, WCD is modeled through the SA approach proposed by Lee’s model for describing the remote sensing reflectance in terms of biophysical parameters [14]. For a given pixel in a spectral datacube, the parameter vector is represented as $\boldsymbol{\theta} = (z, \boldsymbol{\omega})$, where z is the WCD. The vector $\boldsymbol{\omega}$ encapsulates various nuisance parameters and can be decomposed

into $\boldsymbol{\omega} = (\boldsymbol{\omega}_c, \boldsymbol{\omega}_b, \boldsymbol{\omega}_g, \boldsymbol{\omega}_e)$. Here, $\boldsymbol{\omega}_c$ and $\boldsymbol{\omega}_b$ are associated with the water IOPs and bottom properties, respectively. The viewing geometry is captured by $\boldsymbol{\omega}_g$, which itself is decomposed into $\boldsymbol{\omega}_g = (\xi_s, \xi_v)$, representing the solar zenith and viewing angles. $\boldsymbol{\omega}_g$ is considered fixed as it can be extracted directly from sensor metadata, assuming the sensor's geometric performance is reliable. For our study, we selected a solar zenith angle of 30° and a viewing angle of 0° , with the latter representing the nadir direction for off-zenith angles, typically corresponding to standard surveying geometries. The vector $\boldsymbol{\omega}_e$ comprises empirical coefficients from the SA model, retrieved from literature, and will be denoted by γ , β , or ν , indexed according to their specific use as described in the following. These empirical parameters, characterized by regional and seasonal variability, will be considered as fixed, thus reducing the nuisance parameters to $\boldsymbol{\omega} = (\boldsymbol{\omega}_c, \boldsymbol{\omega}_b)$. This practice is prevalent since these parameters are commonly derived from established processes such as laboratory analysis of water samples or data-driven methods, and considering them as fixed facilitates the use of the models in their natural configurations, improving the clarity and accuracy of the outcomes.

2.1 Shallow water Semi-Analytical model [14]

The above-surface remote sensing reflectance \mathbf{R}_{rs}^+ in terms of depth z , water column parameters $\boldsymbol{\omega}_c$, bottom parameters $\boldsymbol{\omega}_b$ is related to the subsurface remote sensing reflectance \mathbf{R}_{rs}^- by:

$$\mathbf{R}_{rs}^+(z, \boldsymbol{\omega}_c, \boldsymbol{\omega}_b) = \frac{\gamma_s \times \mathbf{R}_{rs}^-(z, \boldsymbol{\omega}_c, \boldsymbol{\omega}_b)}{1 - \beta_s \times \mathbf{R}_{rs}^-(z, \boldsymbol{\omega}_c, \boldsymbol{\omega}_b)} \quad (4.1)$$

While this model is underpinned by radiative transfer (RT) theory, it incorporates empirical components such as bottom spectra and chlorophyll absorption spectra, which are inherently variable and region-specific. These empirical components are selected based on established literature values, recognizing their variability. This approach allows us to focus on the primary objectives of the model without the need for detailed justification of these empirical choices, which, although secondary, are essential for the model's application.

The empirical coefficients γ_s and β_s encapsulate the surface effects of factors such as viewing geometry, water properties and internal reflections. These are fixed at the values $\gamma_s = 0.5$ and $\beta_s = 1.5$ as provided in [14].

The subsurface remote sensing reflectance \mathbf{R}_{rs}^- is modeled as the sum of the remote sensing reflectances due to water column \mathbf{R}_{rs}^C and bottom \mathbf{R}_{rs}^B :

$$\mathbf{R}_{rs}^-(z, \boldsymbol{\omega}_c, \boldsymbol{\omega}_b) = \mathbf{R}_{rs}^C(z, \boldsymbol{\omega}_c) + \mathbf{R}_{rs}^B(z, \boldsymbol{\omega}_c, \boldsymbol{\omega}_b) \quad (4.2)$$

The remote sensing reflectance due to bottom contribution \mathbf{R}_{rs}^B is expressed as:

$$\mathbf{R}_{rs}^B(z, \boldsymbol{\omega}_c, \boldsymbol{\omega}_b) = \frac{\boldsymbol{\rho}(\boldsymbol{\omega}_b)}{\pi} \exp(-\mathbf{K}_u^B(\boldsymbol{\omega}_c) \times z) \quad (4.3)$$

Here, $\boldsymbol{\rho}(\boldsymbol{\omega}_b)$ is the seabed reflectance, which is modeled as a sum-to-one linear mix of sand and vegetation reflectances. We use two empirical spectra, $\boldsymbol{\rho}_1$ and $\boldsymbol{\rho}_2$, representing the spectra for sand and vegetation, respectively. The parameter α_m controls the mixing ratio between them as the sole component of $\boldsymbol{\omega}_b$:

$$\boldsymbol{\rho}(\alpha_m) = (1 - \alpha_m)\boldsymbol{\rho}_1 + \alpha_m\boldsymbol{\rho}_2 \quad (4.4)$$

The remote sensing reflectance due to water column \mathbf{R}_{rs}^C is given by:

$$\mathbf{R}_{rs}^C(z, \boldsymbol{\omega}_c) = \mathbf{r}_{rs}^{dp}(\boldsymbol{\omega}_c) \left(1 - \exp(-\mathbf{K}_u^C(\boldsymbol{\omega}_c) \times z)\right) \quad (4.5)$$

\mathbf{K}_u^C and \mathbf{K}_u^B are the diffuse attenuation coefficients for the water column and bottom, respectively whereas \mathbf{r}_{rs}^{dp} is the remote-sensing reflectance for optically deep waters. These are functions of the optically active constituents of the water, all parameterized by $\boldsymbol{\omega}_c$:

$$\mathbf{K}_b(\boldsymbol{\omega}_c) = \left(\frac{1}{\cos(\xi_s)} + \frac{\gamma_b \sqrt{1 + \beta_b \mathbf{u}(\boldsymbol{\omega}_c)}}{\cos(\xi_v)} \right) \boldsymbol{\kappa}(\boldsymbol{\omega}_c), \quad (4.6)$$

$$\mathbf{K}_c(\boldsymbol{\omega}_c) = \left(\frac{1}{\cos(\xi_s)} + \frac{\gamma_c \sqrt{1 + \beta_c \mathbf{u}(\boldsymbol{\omega}_c)}}{\cos(\xi_v)} \right) \boldsymbol{\kappa}(\boldsymbol{\omega}_c), \quad (4.7)$$

$$\mathbf{r}_{rs}^{dp}(\boldsymbol{\omega}_c) = (\gamma_{dp} + \beta_{dp} \mathbf{u}(\boldsymbol{\omega}_c)) \mathbf{u}(\boldsymbol{\omega}_c). \quad (4.8)$$

The empirical coefficients are set to the values $\gamma_c = 1.03, \gamma_b = 1.04, \beta_c = 2.4, \beta_b = 5.4$ as provided in [14]. Here, $\boldsymbol{\kappa}$ and \mathbf{u} are defined as:

$$\boldsymbol{\kappa}(\boldsymbol{\omega}_c) = \mathbf{a}(\boldsymbol{\omega}_c) + \mathbf{b}_b(\boldsymbol{\omega}_c), \quad \mathbf{u}(\boldsymbol{\omega}_c) = \frac{\mathbf{b}_b(\boldsymbol{\omega}_c)}{\boldsymbol{\kappa}(\boldsymbol{\omega}_c)}. \quad (4.9)$$

For modeling the absorption \mathbf{a} and backscattering \mathbf{b}_b coefficients, we consider the absorption contributions from water, phytoplankton, CDOM, and Total Suspended Matter (TSM), as well as the backscattering contributions from water and TSM. For a detailed description of the equations modeling absorptions and backscattering, the reader is referred to Sections 1 and 2.

Consequently, the primary parameters besides the $\mathbf{WCD}(z)$, are the seabed albedo mixing ratio α_m , and the concentrations of chlorophyll (in mg m^{-3}), CDOM (in m^{-1}), and TSM (in g m^{-3}). Formally, $\boldsymbol{\theta} = \{\psi : z, \boldsymbol{\omega} : \{\boldsymbol{\omega}_b : \alpha_m, \boldsymbol{\omega}_c : \{\text{Chl, CDOM, TSM}\}\}\}$.

To account for sensor-specific effects and the integration over the sensor's spectral response functions, we redefine the sensor-dependent above-surface remote sensing reflectance, denoted as \mathbf{R}_{rs}^{S+} . This measurement includes the dependency on each of the sensor's discrete sampling bands. The integrated remote sensing reflectance for each band B_k is defined as:

$$\mathbf{R}_{rs}^{S+}(z, \boldsymbol{\omega}, B_k) = \frac{\int_{\lambda \in B_k} S_k(\lambda) \cdot \mathbf{R}_{rs}^+(z, \boldsymbol{\omega}, \lambda) d\lambda}{\int_{\lambda \in B_k} S_k(\lambda) d\lambda} \quad (4.10)$$

where B_k represents each discrete spectral band of the sensor, and $S_k(\lambda)$ is the spectral response function of the sensor at each wavelength λ within the band B_k . This normalized integration ensures that the reflectance values are adjusted for the overall sensitivity of the sensor across its bandwidth.

2.2 Statistical modeling

In our model, we consider a Gaussian measurement model for the remote sensing reflectance at n different wavelengths, spanning the VNIR spectrum [15]. For each band B_k , $k = 1, \dots, n$, the observed above-surface remote sensing reflectance $\mathbf{y}(B_k)$ is modeled as:

$$\mathbf{y}(B_k) = \mathbf{R}_{rs}^{S+}(z, \boldsymbol{\omega}, B_k) + \boldsymbol{\epsilon}(B_k) \quad (4.11)$$

Here, $\mathbf{R}_{rs}^{S+}(z, \boldsymbol{\omega}, B_k)$ is the true above-surface remote sensing reflectance at depth z , with parameter vector $\boldsymbol{\omega}$, and at band B_k . The term $\boldsymbol{\epsilon}(B_k)$ represents the measurement noise at band B_k , $\boldsymbol{\epsilon}$ is assumed to follow a multivariate Gaussian distribution $\boldsymbol{\epsilon} \sim \mathcal{N}(\mathbf{0}, \boldsymbol{\Sigma})$.

The log-likelihood can be computed as:

$$\ell(z, \boldsymbol{\omega}; \mathbf{y}) = -\frac{1}{2}(\mathbf{y} - \mathbf{R}_{rs}^{S+})^T \boldsymbol{\Sigma}^{-1}(\mathbf{y} - \mathbf{R}_{rs}^{S+}) + \text{Cte} \quad (4.12)$$

The score for the interest parameter, i.e., the derivative of the log-likelihood with respect to all the parameters $\boldsymbol{\theta}$, is expressed as follow:

$$\frac{\partial \ell}{\partial \boldsymbol{\theta}} = \left(\frac{\partial \mathbf{R}_{rs}^{S+}}{\partial \boldsymbol{\theta}} \right)^T \boldsymbol{\Sigma}^{-1}(\mathbf{y} - \mathbf{R}_{rs}^{S+}) \quad (4.13)$$

The Expected Fisher Information Matrix (EFIM) $\mathbf{i}(\boldsymbol{\theta})$ and the Observed Fisher Information Matrix (OFIM) $\mathbf{j}(\boldsymbol{\theta}; \mathbf{y})$ are given by [81]:

$$\mathbf{i}(\boldsymbol{\theta}) = \left(\frac{\partial \mathbf{R}_{rs}^{S+}}{\partial \boldsymbol{\theta}} \right)^T \boldsymbol{\Sigma}^{-1} \left(\frac{\partial \mathbf{R}_{rs}^{S+}}{\partial \boldsymbol{\theta}} \right), \quad \mathbf{j}(\boldsymbol{\theta}; \mathbf{y}) = \mathbf{i}(\boldsymbol{\theta}) - (\mathbf{y} - \mathbf{R}_{rs}^{S+})^T \boldsymbol{\Sigma}^{-1} \frac{\partial^2 \mathbf{R}_{rs}^{S+}}{\partial \boldsymbol{\theta}^2} \quad (4.14)$$

i_p and j_p used for WCD first-order inference in Wald test statistics (2.11) and (2.10) can be readily obtained as the first diagonal element corresponding to z of $\mathbf{i}^{-1}(\hat{\boldsymbol{\theta}})$ and $\mathbf{j}^{-1}(\hat{\boldsymbol{\theta}}; \mathbf{y})$. Using the likelihood derivative (4.13) with respect to z at the constrained MLE $\hat{\boldsymbol{\theta}}_\psi$, it's straightforward to compute the score test (2.12).

In pursuing higher-order inference, we employ the following second-order profile likelihood adjustment presented in [83]:

$$\ell_m(\psi; \mathbf{y}) = \ell_p(\psi; \mathbf{y}) + \frac{1}{2} \log(\det(\mathbf{j}_{\omega\omega}(\hat{\boldsymbol{\theta}}_\psi))) - \mathbb{E}_{\hat{\boldsymbol{\theta}}}[\ell_\omega(\hat{\boldsymbol{\theta}})\ell_\omega(\hat{\boldsymbol{\theta}})^T] \quad (4.15)$$

where $\mathbf{j}_{\omega\omega}(\hat{\boldsymbol{\theta}}_\psi)$ is the observed information for the nuisance parameter evaluated at the constrained MLE $\hat{\boldsymbol{\theta}}_\psi$. The additional adjustment term $\mathbb{E}_{\hat{\boldsymbol{\theta}}}[\ell_\omega(\hat{\boldsymbol{\theta}})\ell_\omega(\hat{\boldsymbol{\theta}})^T]$ for the profile likelihood under this statistical model is derived as described in Section 3.

3 Results

The results section aims to present the empirical findings of our study. We conducted a series of experiments to investigate the performance of WCD inference under various environmental setups. These experiments were carried out for different configurations of the parameter vector $\tilde{\boldsymbol{\theta}} = \{\tilde{\psi} : \tilde{z}, \tilde{\omega} : \{\tilde{\alpha}_m, \tilde{\text{Chl}}, \tilde{\text{CDOM}}, \tilde{\text{TSM}}\}\}$, covering different environmental conditions and sensor technologies.

3.1 Experimental setup

We explored distinct water conditions by adjusting the WCD z in 5-meter increments from 1 to 20 meters, according to different IOP parameterizations and seabed reflectance mixing ratios. The experimental conditions of the water column and the seabed are comprehensively detailed in Table 4.1.

Table 4.1 – True parameter values ($\tilde{\theta}$) of the water column used in the analysis.

	Chl (mg/m^3)	CDOM (m^{-1})	TSM (g/m^3)	α_M
CWBB	0.05	0.05	0.1	0.8
TWBB	0.5	0.5	3	0.8
CWDB	0.05	0.05	0.1	0.1
TWDB	0.5	0.5	3	0.1

These conditions, visually represented in Table 4.3, are illustrated with their spectral reflectances and Red Green Blue (RGB) approximations derived from the theoretical R_{rs} values to highlight spectral discrepancies across parameter sets. Parametrizations were established based on distinct aquatic and substrate conditions, designated as CWBB for clear water bodies over sandy substrates, CWDB for clear water bodies over vegetated or dark substrates, TWBB for turbid or nutrient-rich waters over sandy bottoms, and TWDB for turbid waters over dark or organic-rich substrates. These categorizations cover a spectrum of chlorophyll, dissolved organic material, suspended solids, and albedo parameters, to represent the diverse conditions under which WCD inference was evaluated.

Monte Carlo simulations and optimization procedures were conducted as outlined in Table 4.2. These procedures employed 10,000 iterations for Monte Carlo simulations and leveraged the trust-region method from the SciPy library for optimization [121], selected for its optimal performance in our testing scenarios. The experiments spanned a wavelength range of 400-800 nm with a spectral resolution of 1 nm, adhering to the spectral range commonly used in coastal optical remote sensing. The variance for modeling the reflectance noise was set to 1×10^{-7} , which is a representative value of high-end satellite imagers in the coastal cover [15]. The

Table 4.2 – Experimental configuration.

Parameter	Value
Noise (R_{rs} variance)	1×10^{-7}
Wavelength Range	400-800nm
Spectral resolution	1nm
Optimizer	Trust-region
Monte Carlo Samples	10,000
Profiling samples	50

optimization approach, devoid of boundary constraints, was chosen to satisfy the regularity conditions necessary for the asymptotic theory, ensuring a smooth and convex likelihood landscape around the MLE. Initiating the experiments from true parameter values facilitated swift convergence to a statistically significant local log-likelihood maximum, thereby bolstering the robustness of our findings. To highlight the significance of spectral data granularity on WCD inference accuracy, our study further differentiated between two sensor technologies. We analyzed multispectral data captured by the Sentinel MSI2 sensor alongside hyperspectral data obtained from the HySpex sensor, the response characteristics of which are detailed in Section 1.1 of Chapter 1. This comparative approach enabled a deeper understanding of how sensor resolution influences WCD inference outcomes.

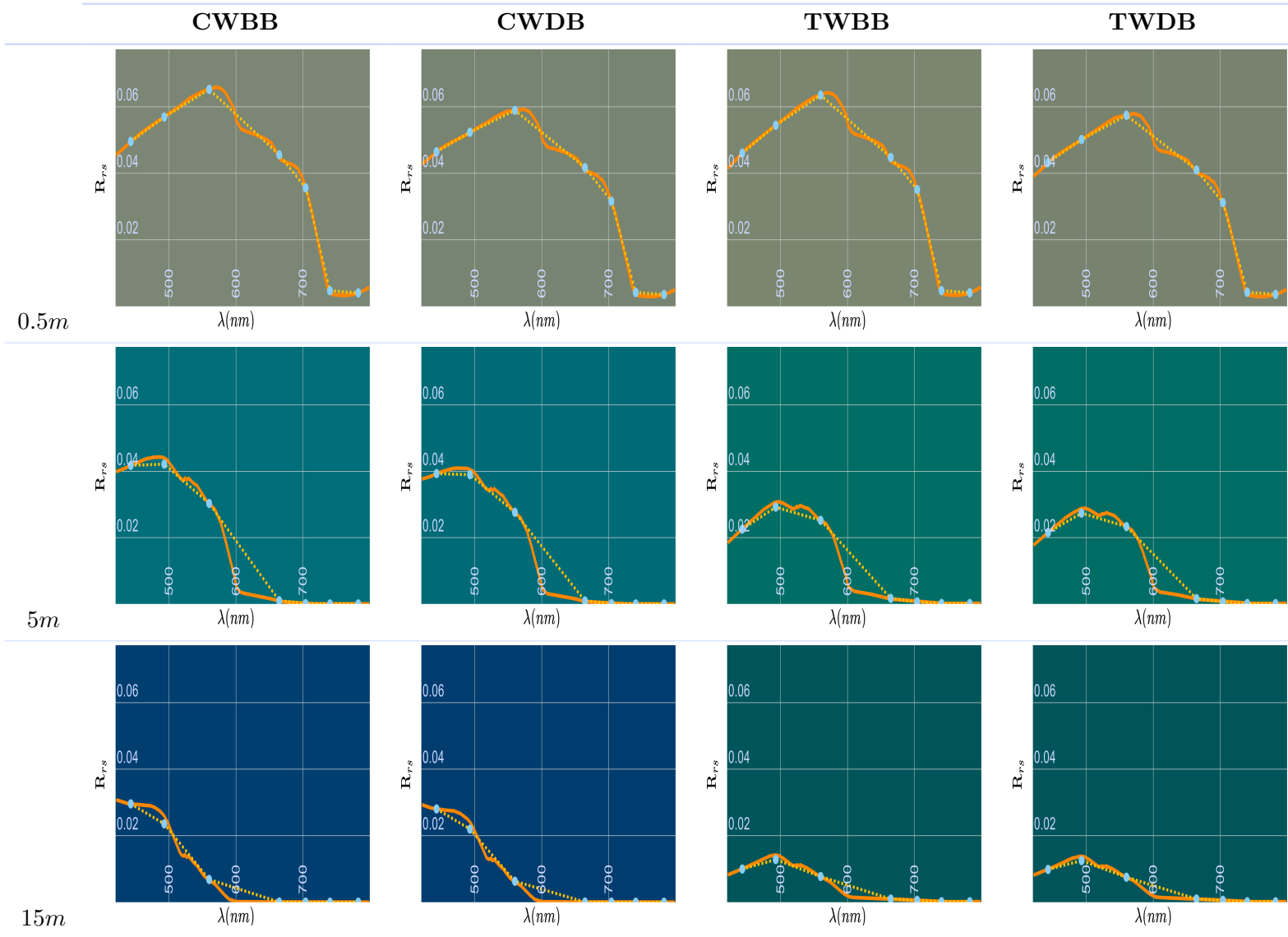


Table 4.3 – Theoretical and Sentinel-2A MSI-sampled R_{rs} spectra for water column parameterizations at 0.5m, 5m and 15m depths, corresponding to the parameterizations in Table 4.1. Orange lines indicate the Lee model’s theoretical R_{rs} , while yellow dashed lines with cyan dots show Sentinel-2A MSI samples. Background colors are derived from the CMIE93 method using CIE 1931 2 degree standard observer Colour Matching Functions (CMF).

3.2 WCD profiling results

Having established the experimental configurations and the analytical framework, we now proceed to examine the profiling process. This section delves into the profiling diagnosis, critically assessing the refinement of MLE estimates under varying environmental conditions.

3.2.1 Profiling analysis

This section presents a selective summary through specific instances of the profiles typically encountered, offering justifications or arguments supporting the various findings.

3.2.1.a Ideal case The hyperspectral context for the CWBB scenario at a depth of 5 meters, exemplifies an ideal case for profiling the WCD parameter. Figure 4.1 shows a sym-

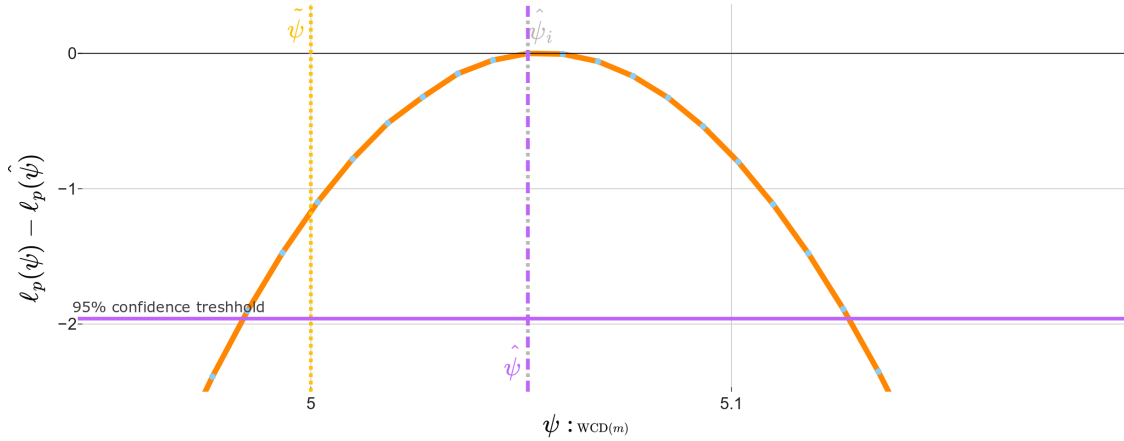


Figure 4.1 – Profile likelihood in hyperspectral scenarios for the parameterization CWBB at a WCD of 5 meters. The orange curve depicts the normalized log-likelihood, $\ell_p(\psi) - \ell_p(\hat{\psi})$, with the yellow dashed vertical line indicating the true WCD value. The initial and refined MLEs, $\hat{\psi}_i$ and $\hat{\psi}$ are denoted by grey and melrose dashed vertical lines, respectively.

metric parabolic curve around the MLE, indicating a well-behaved likelihood surface. In this figure, two MLE estimates are shown: $\hat{\psi}_i$, the initial MLE provided by the optimizer and $\hat{\psi}$, the refined MLE. Due to the non-linearities in SA models, the overall MLE $\hat{\theta}$ does not coincide with the profile maximum indicating the presence of local minimas. In our analysis, the refined MLE is simply chosen as the interest value maximizing the sampled profile likelihood $\arg \max_{\psi} \ell_p(\psi)$. The two estimates overlap, indicating a successful optimization for the WCD parameter z in this case.

In conjunction with the profiling of hyperspectral data for the CWBB scenario, we examine the curves of first-order test statistics calculated for the same sample. Figure 4.2, illustrates that all statistics r , t_e , t_o , and s —defined in Section 4.2.2 of Chapter 2—exhibit linearly

decreasing slopes. This behavior is emblematic of likelihood theory in large sample scenarios, where the test statistics are expected to converge and provide consistent inference results.

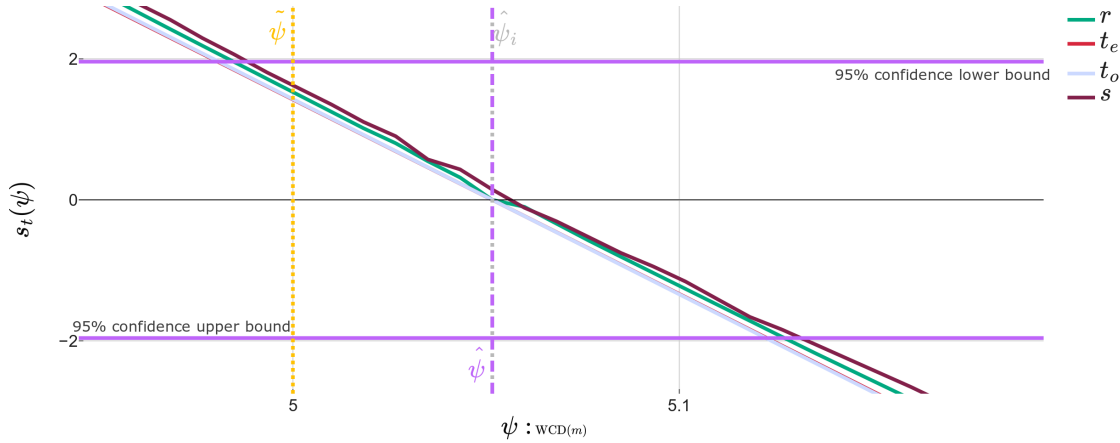


Figure 4.2 – First-order test statistics curves for the parameterization CWBB at a WCD of 5 meters. $\hat{\psi}_i$, $\hat{\psi}$ and $\tilde{\psi}$ are illustrated as in 4.1. The horizontal lines in melrose color depict the 95% CI thresholds for the lower and upper bounds.

The clear convergence of the statistics reaffirms the strength of the large-sample theory in providing a robust framework for uncertainty quantification in optimal conditions. Such alignment among the different test statistics underscores the reliability of the likelihood-based inference in these optimal conditions. It is also worth indicating that the true parameter value is encompassed by the 95% CI, as is statistically expected in 95% of cases.

3.2.1.b Asymmetric case An interesting aspect of profiling is when it reveals asymmetry, significantly influencing the shape of CI in both hyperspectral (Figures 4.3 and 4.4) and multispectral (Figure 4.5) scenarios. In hyperspectral data, the asymmetric behavior of the profile likelihood and corresponding statistics only begins to emerge under the unfavorable optical conditions TWBB and TWDB, when coupled with depths greater than 10 meters. This contrasts with scenarios involving clear waters, which tend to align with the ideal case, showing general agreement up to 20 meters in our simulations. In Figure 4.3, both the profile likelihood and the associated curves of statistical tests are presented to demonstrate the implications of this asymmetry.

The profile likelihood reveals that the CI derived from r and s are asymmetric, which may more accurately reflect the distribution of the MLE. While both r and s will result in asymmetric 95% CI, the latter is consistently more sensitive to the asymmetry than the likelihood ratio due to its direct dependence on the likelihood first derivative. The s test’s curve, in particular, reveals a heightened sensitivity which can be indicative of model fitting issues at the different hypothesis at which the profile is sampled. In contrast, the Wald test statistics demonstrate a subtle agreement between the EFIM and the OFIM. However, the Wald tests symmetric intervals could be misleading in the presence of such an asymmetric likelihood.

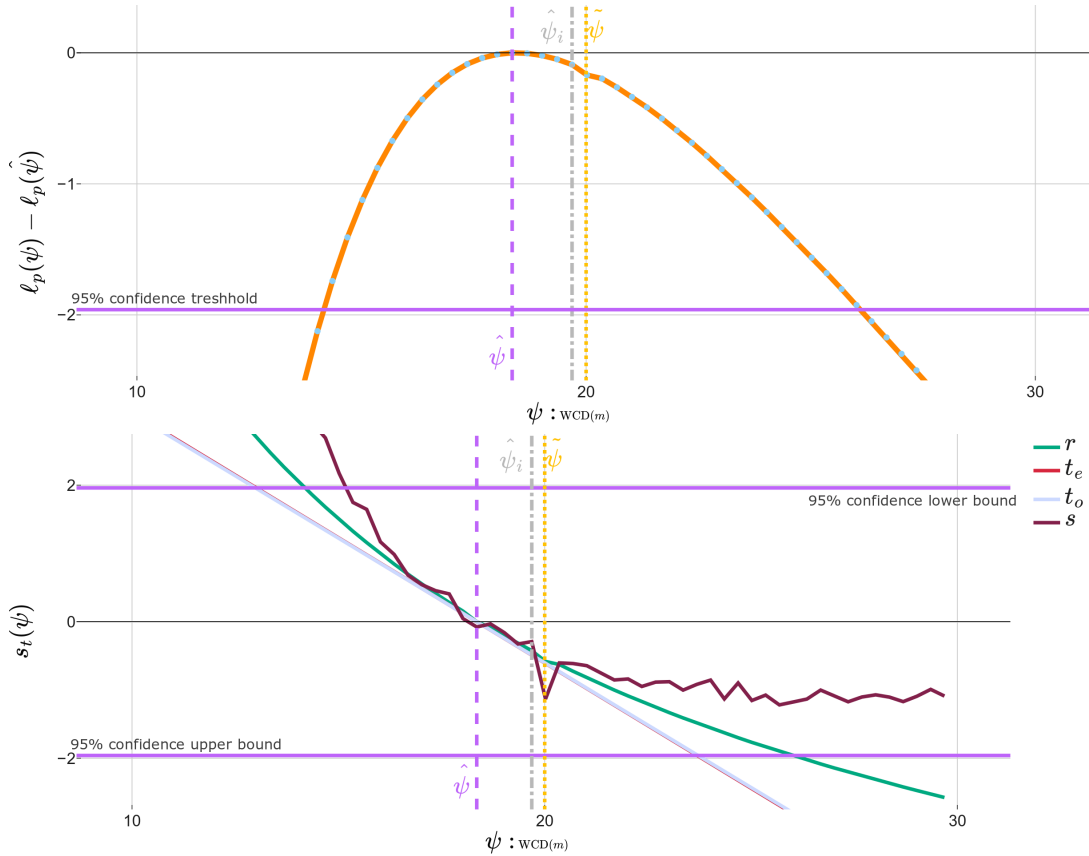


Figure 4.3 – Top: Profile likelihood for the parameterization TWDB at a WCD of 20 meters in hyperspectral scenarios. Bottom: The corresponding first-order test statistics curves. The Figure notations are the same as those detailed in Figures 4.1 and 4.2.

Furthermore, this case presents an example where the initial MLE, $\hat{\psi}_i$, is notably displaced from the final MLE, $\hat{\psi}$, indicating a significant update of 2.4m meters through profiling. This update is crucial as it impacts the standard deviations of both Wald tests. If the profiling is not executed, the standard deviations would be 3.5m and 4.5m for t_e and t_o respectively. However, when the matrices are computed at the final MLE, the standard deviations decrease to approximately 2.9m and 3.1m, respectively. This suggests a potential overestimation of uncertainty if one were to rely solely on the optimizer’s initial MLE. The impact of this update on the inference of WCD estimation and its uncertainty varies significantly from sample to sample and from scenario to scenario. This variability and its implications on the WCD uncertainty are further analyzed in the subsequent subsection 3.2.2.

The statistical distribution of the MLE for the same sample further corroborates the asymmetric nature of the uncertainty in the WCD estimation. Figure 4.4, illustrates this skewed distribution, reinforcing the need for caution when interpreting symmetric intervals provided by Wald statistics in the presence of such asymmetry.

In contrast to hyperspectral data, significant asymmetry is observed in multispectral data

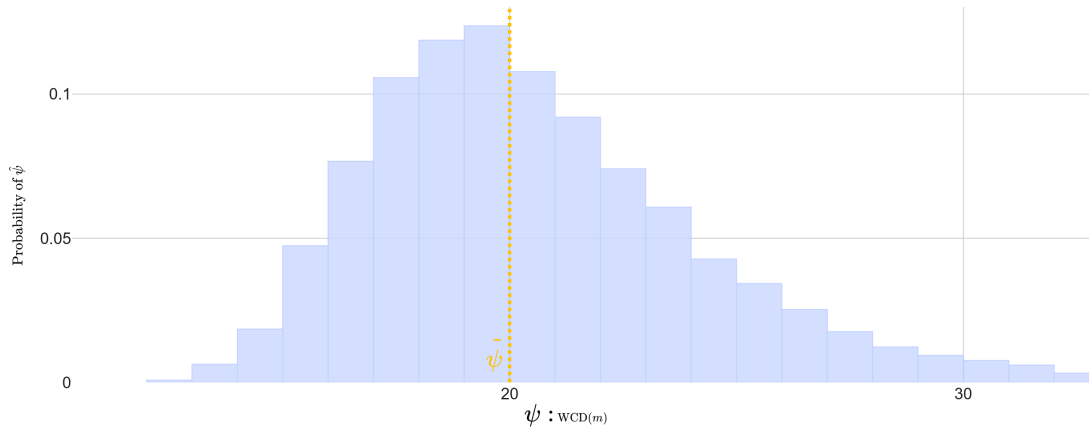


Figure 4.4 – Statistical distribution of the WCD MLE for the parameterization TWDB at a WCD of 20 meters in the hyperspectral scenario, presented as the probability of each bin relative to the number of samples.

(Sentinel MSI-2), becoming apparent at depths as shallow as 5 meters, even in clear waters as demonstrated in Figure 4.5.

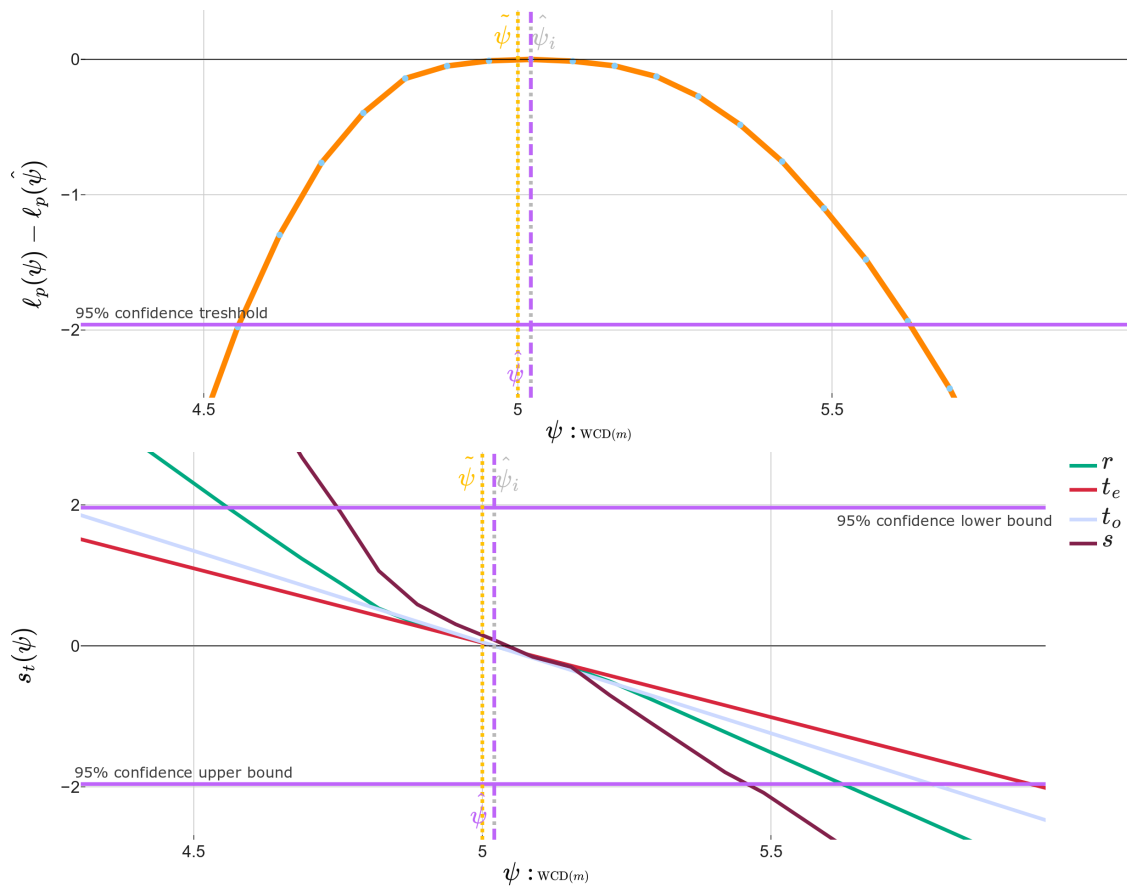


Figure 4.5 – Top: Profile likelihood for the parameterization CWBB at a WCD of 5 meters in multispectral scenarios using Sentinel MSI-2. Bottom: The corresponding first-order test statistics curves.

The profile likelihood and test statistics r and s start showing notable asymmetry for the parametrization CWBB at a depth of 5 meters. This flatness in the likelihood surface, particularly evident in clear water scenarios at this depth, highlights the increasing challenges in WCD inference as the amount of sample size information decreases. The asymmetry observed in these cases can be attributed to the inherent difficulty in ascertaining the precise end of the water column. It reveals the inherent challenges of SA models in interpreting the data unambiguously and deriving the upper bound of WCD, which is swiftly translated into the flatness observed in the likelihood profile as illustrated by the multispectral case.

3.2.1.c Practical identifiability case This case delves into scenarios where extreme asymmetry leads to practical identifiability issues, particularly notable in the multispectral data for the TWDB scenario at greater depths as illustrated in Figure 4.6.

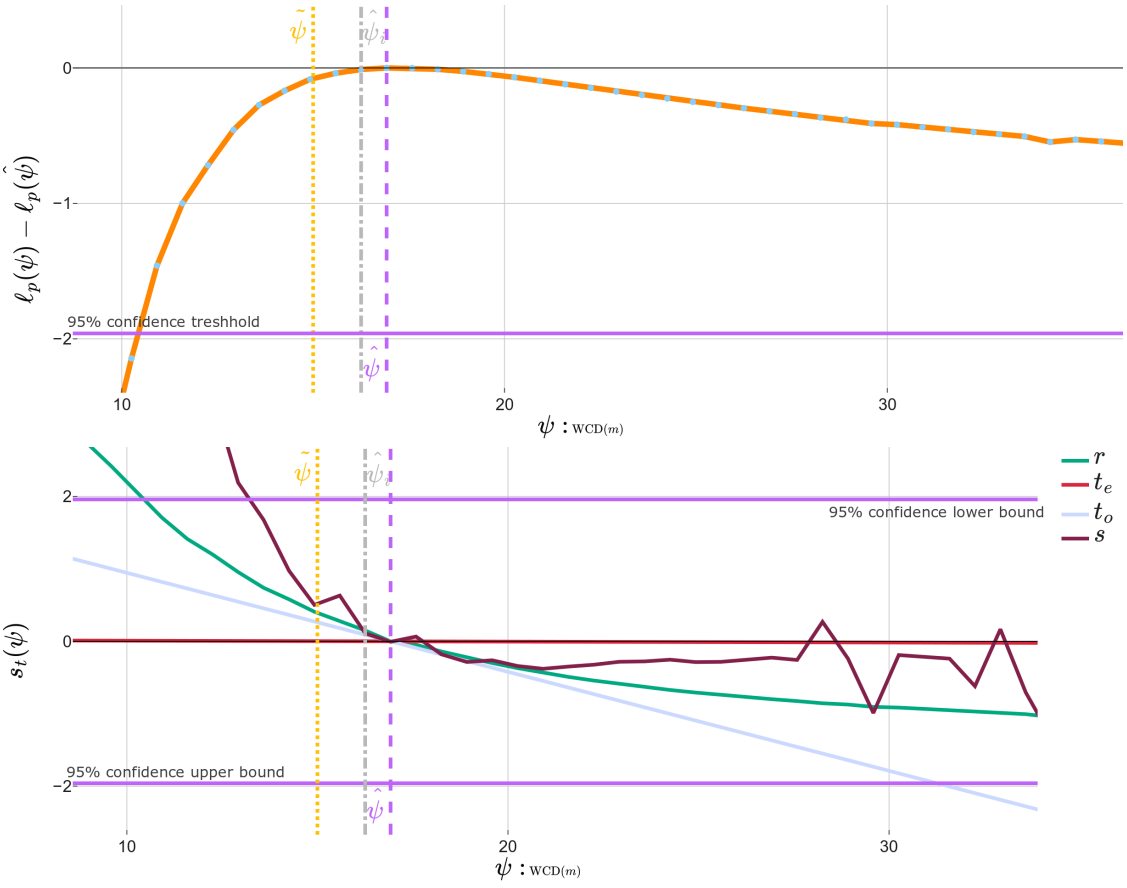


Figure 4.6 – Top: Profile likelihood for the parameterization TWDB at a WCD of 15 meters in a multispectral scenario using Sentinel MSI-2. Bottom: The corresponding first-order test statistics curves indicating inability to identify the upper bounds for the tests r and s . The Figure notations are the same as those detailed in Figures 4.1 and 4.2.

We notice a significant distortion in the likelihood surface as depth increases, marked by a slow decline in the likelihood relative to decreases in depth.

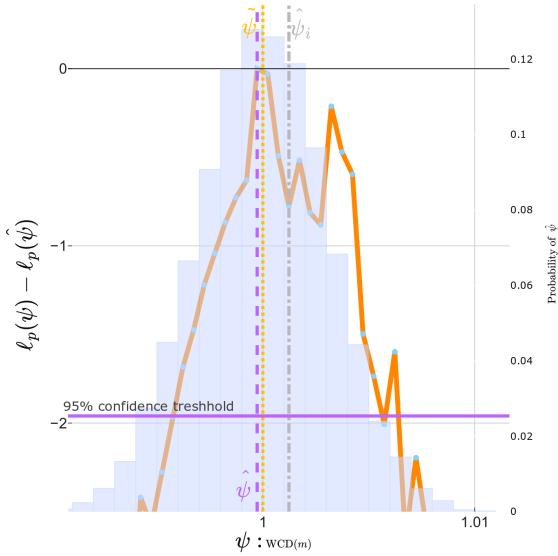
This extreme asymmetry results in non-identifiable upper bounds for both the likelihood ratio and score tests, highlighting the challenges of interpreting the first-order 95% CI in settings with low sample sizes such as multispectral data. It is important to note that this behavior is not necessarily sample-specific; another sample may exhibit identifiable 95% confidence bounds for the likelihood ratio and the score.

Interestingly, the slope of the t_e test statistic is notably low compared to others, a behavior which is also confirmed for the case illustrated in Figure 4.5. This indicates that variance-covariance propagation, equivalent to the Wald test t_e , tends to provide inflated 95% CI in the multispectral setup. In our calculations of r and s rejection rates, for cases where no intersection for the upper bound was found, we only consider the position of the true hypothesis in relation to the lower bound—if it is greater, it is retained; if it is smaller, it is rejected.

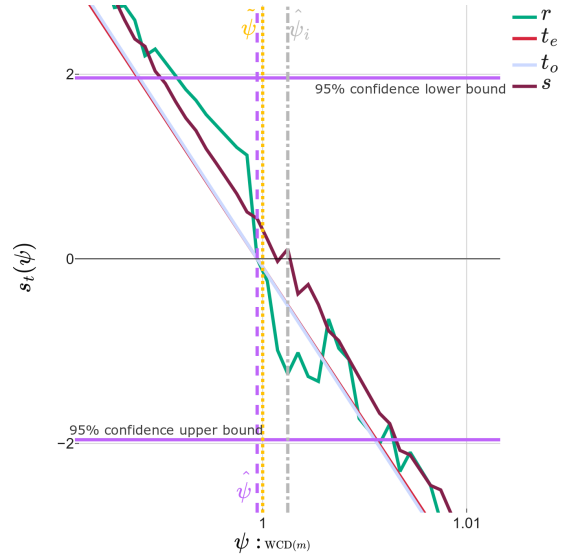
3.2.1.d Outliers case Transitioning from the previously diagnosed cases, certain profiles exhibit outliers that disrupt the expected parabolic characteristics typically expected in large sample scenarios. This irregularity is even observed in hyperspectral data, which is generally considered to provide high-resolution and stable estimates. Outliers presented in Figures 4.7a and 4.7b in the profile likelihood are most pronounced in scenarios involving shallow clear waters, where water constituents, mainly TSM in this case, become non-identifiable. This can be diagnosed on the Fisher Information Matrices, which exhibits large variance for these parameters under such conditions. Additionally, the obtained constrained MLEs along the profile for TSM are constant. This behavior of TSM non-identifiability which can mainly result from data insensitivity to changes in turbidity at this shallow depth. These anomalies can lead to irregular shapes in the profile likelihood, such as ramps, which may accidentally result in multiple intersection points on the statistical curves.

In the presented multispectral outlier scenario of turbid waters at a depth of 10 meters (Figures 4.7c and 4.7d), the profile likelihood behaves quite differently compared to the hyperspectral case. Although the r statistic demonstrates a well-behaved profile with a discernible peak, there is notable asymmetry and flatness around the maximum, which is indicative of robust yet complex underlying dynamics in the water column. This complexity is further manifested in the s statistic, which reveals hidden irregularities. Specifically, the first derivative of the likelihood, sensitive to low statistical information, leads to multiple intersection points.

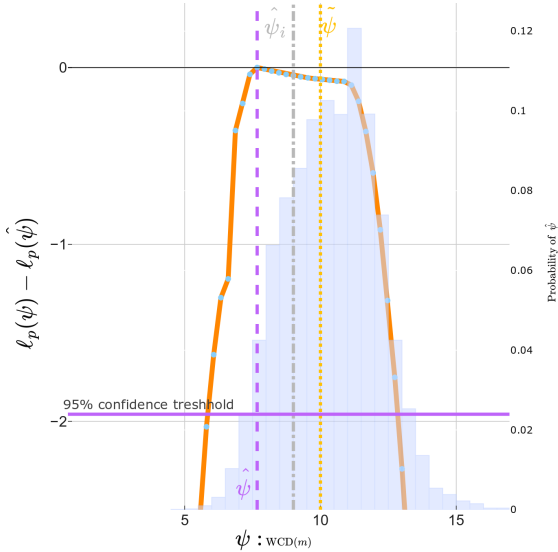
This multiple intersections phenomenon underscores the challenges in interpreting statistics like the score and likelihood ratio tests under conditions of limited data richness, a common issue in both hyperspectral and multispectral analyses. The presence of multiple intersections, observed at both lower and upper confidence bounds, is particularly concerning as it may reflect potential ambiguities in parameter identifiability or optimization challenges. This may



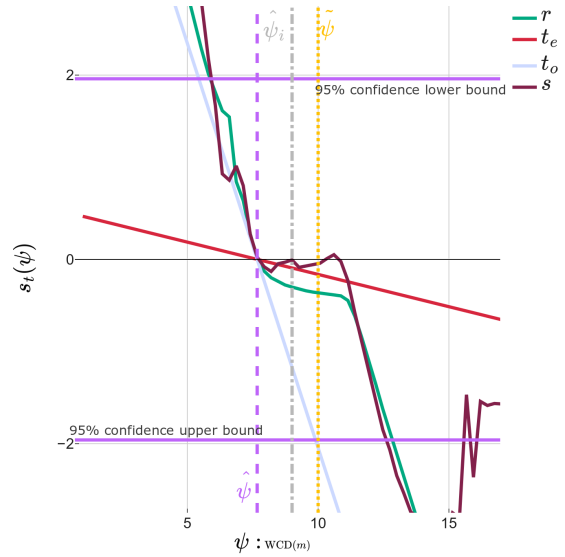
(a): Profile likelihood for CWBB at 1 meter in hyperspectral data, depicting outliers with multiple intersections.



(b): Statistical curves for CWBB at 1 meter in hyperspectral data, showing the impact of outliers on the uncertainty estimation with multiple intersections.



(c): Profile likelihood for TWDB at 10 meters in multispectral data, showing asymmetry and flatness around the maximum.



(d): Statistical curves for TWDB at 10 meters in multispectral data, with irregularities in the score statistic leading to dual intersections at the lower bound.

Figure 4.7 – Profiling outlier cases in hyperspectral (a and b) and multispectral scenarios (c and d). The Figure notations are the same as those detailed in Figures 4.1 and 4.2.

complicate the interpretation of model outputs, indicating areas where the data may not sufficiently inform the parameter estimates. To ensure conservative and robust reporting of uncertainty, we choose the farthest intersection point in our analyses, regardless of whether it appears at the upper or lower bounds. This methodological choice is crucial to mitigate the

risk of underestimating the true uncertainty.

3.2.2 Refinement impact

To further investigate the impact of refining the MLE on the WCD inference, we introduce four pivotal metrics: the update frequency, the Average Estimation Update (AEU), the Average Precision Update (APU) and the Directional Average Precision Update (DAPU), defined as follows:

1. **Update Frequency:** the proportion of samples for which the MLE is updated during the profiling process. This metric reflects the frequency of refinements needed to achieve convergence.

$$\text{Refinement Frequency (\%)} = \left(\frac{\text{Number of Samples with Updated MLE}}{\text{Total Number of Samples}} \right) \times 100\%$$

2. **Absolute Estimated Uncertainty (AEU):** the average absolute percentage change in the WCD estimates before and after profiling. It quantifies the average adjustment magnitude applied to the MLE values.

$$AEU = \frac{1}{N} \sum_{i=1}^N \left| \frac{\hat{\psi}_i - \hat{\psi}}{\hat{\psi}} \right| \times 100\%$$

where N is the number of samples, $\hat{\psi}_i$ is the initial MLE estimate, and $\hat{\psi}$ is the refined MLE estimate.

3. **Absolute Profiling Update (APU):** the absolute relative change in the standard deviations of the Wald tests before and after profiling, indicating the degree of change in uncertainty quantification.

$$APU = \frac{1}{N} \sum_{i=1}^N \left| \frac{\sigma_{t_e} - \sigma_{t_{e_i}}}{\sigma_{t_e}} \right| \times 100\%$$

where σ_{t_e} and $\sigma_{t_{e_i}}$ are the standard deviations refined and at the initial MLE, respectively.

4. **Directional Absolute Profiling Update (DAPU):** Similar to APU, but computed without taking the absolute value to capture the direction of the update (overestimation or underestimation).

$$DAPU = \frac{1}{N} \sum_{i=1}^N \left(\frac{\sigma_{t_e} - \sigma_{t_{e_i}}}{\sigma_{t_e}} \right) \times 100\%$$

Negative values indicate an overestimation of uncertainty prior to profiling, while positive values suggest an underestimation.

The MLE refinement metrics for HySpex are presented in Table 4.4 while those for MSI-2 are presented in Table 4.5. These results show uneven levels of refinement accross scenarios. Update frequencies above 50% in most scenarios, particularly noted in multispectral MSI-2 measurements, indicate a significant potential for refinement. However, AEU values under 5% suggest that the absolute improvements in parameter estimation through profiling are modest.

Table 4.4 – HySpex MLE refinement metrics

Depth (m)	Param.	Refinement Metrics (%)				95% Monte Carlo CI (m)
		Freq.	AEU	t_e APU (DAPU)	t_o APU(DAPU)	
1.0	CWBB	68.0	1.0	0.0(0.0)	0.0(0.0)	0.01
	CWDB	72.0	0.0	0.0(0.0)	2.0(-1.0)	0.01
	TWBB	86.0	0.0	8.0(4.0)	29.0(-9.0)	0.02
	TWDB	83.0	0.0	7.0(3.0)	26.0(-9.0)	0.02
10.0	CWBB	80.0	0.0	0.0(0.0)	1.0(0.0)	0.45
	CWDB	79.0	0.0	0.0(0.0)	1.0(0.0)	0.49
	TWBB	68.0	2.0	3.0(3.0)	4.0(4.0)	1.44
	TWDB	59.0	2.0	3.0(3.0)	5.0(5.0)	1.57

Table 4.5 – MSI-2 MLE refinement metrics

Depth (m)	Param.	Update Metrics (%)				95% Monte Carlo CI (m)
		Freq.	AEU	t_e APU (DAPU)	t_o APU(DAPU)	
1.0	CWBB	54.0	0.0	1.0(0.0)	9.0(-2.0)	0.04
	CWDB	48.0	0.0	1.0(0.0)	9.0(-48.0)	0.05
	TWBB	68.0	1.0	24.0(16.0)	37.0(-11.0)	0.06
	TWDB	44.0	1.0	22.0(15.0)	29.0(-4.0)	0.06
10.0	CWBB	68.0	2.0	12.0(-2.0)	69.0(-63.0)	1.74
	CWDB	29.0	3.0	17.0(-2.0)	116.0(-113)	1.95
	TWBB	86.0	10.0	50.0(-15.0)	136.0(-120.0)	5.74
	TWDB	89.0	10.0	58.0(-23.0)	134.0(-119.0)	6.33

In contrast, the APU demonstrates substantial impacts on uncertainty estimates for WCD, with updates approaching 50% in several cases. The DAPU, especially its negative values observed in the tables, indicates a prevailing overestimation of WCD uncertainty in initial

MLEs. This overestimation is effectively corrected through profiling, which not only refines the parameter estimates but also adjusts their associated uncertainties, thereby enhancing the reliability of WCD inference through variance-covariance propagation. The MLE refinements, as evidenced by the metrics APU and DAPU, underscores the importance of profiling in achieving a more accurate representation of uncertainty.

With the profiling framework in place, the subsequent analyses bifurcate into evaluations specific to hyperspectral and multispectral data. Each dataset presents unique challenges and insights into the bathymetric inference process, which we explore in the following subsections.

3.3 First-order inference results

This section evaluates the performance of the first-order statistical tests r , t_o , t_e , and s in estimating the 95% CI (CI) for WCD based on their coverage probabilities, as detailed in Section 4.3 of Chapter 2. The variability in performance between multispectral and hyperspectral data is significant, prompting a thorough analysis of the 95% CI derived from these tests under various scenarios. Initially, we conduct a detailed analysis of the 95% CI for both data types, followed by an assessment of the overall performance of these statistical tests based on their rejection rates.

To effectively evaluate their performance, we categorize the rejection rates as follows:

1. Greater than 8% indicates a conservative response, suggesting that the 95% CI are narrower than expected.
2. Less than 3% indicates a liberal response, implying that the 95% CI are wider than ideal.
3. Values between 3% and 8% represent a moderate response, suggesting well-calibrated 95% CI.

Additionally, we evaluate the statistical distribution of the 95% CI bounds using violin plots to visualize their variability and assess the overall performance of these statistical tests based on their rejection rates.

3.3.1 Hyperspectral data

As depicted in the profiling diagnosis results obtained with hyperspectral data, WCD profile likelihoods are aligned with symmetric parabolic curves, which signals that all the first-order test statistics will yield the same uncertainty estimates resulting in symmetric CI. Figure 4.8 presents a violin plot illustrating the distribution of computed 95% CI for the Wald statistic t_e at a depth of 1 meter in clear water conditions. In this nearly ideal case, the t_e statistic exhibits a symmetric distribution with the median and quartile box closely aligned with the empirical

Monte Carlo derived confidence bounds. Notably, the central tendency of the average MLE, as marked by the dashed melrose line, shows a remarkable adherence to the true parameter value, underlining the absence of bias in the MLE estimations. Such symmetry and alignment with theoretical quantiles serve as a benchmark, setting the stage for subsequent comparative analyses among various first-order statistical tests. Having established the benchmark under

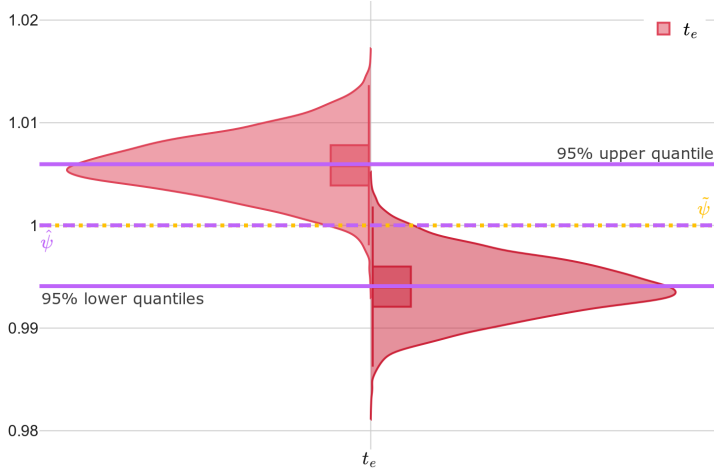


Figure 4.8 – Violin plot for the t_e statistic at 1m depth in clear water conditions. The Melrose horizontal lines denote the Monte Carlo derived average MLE (dashed) and the corresponding 95% quantiles (solid). The true parameter value $\hat{\psi}$ is marked by a yellow dashed line, and its alignment with the Monte Carlo average $\hat{\psi}$ indicates insignificant bias. The quartile boxes within the plot represent the interquartile range of the distribution, showing the 25th to 75th percentile range around the median.

near-ideal conditions, we now shift our focus to the performance of these statistical tests under more extreme scenarios, specifically at greater depths and in environments with more complex optical properties. For dark vegetated seabeds, we examine conditions at a depth of 20 meters, whereas for turbid waters, we limit our depth to 15 meters due to increased complexity and challenges such as outliers, practical identifiability issues, and bounded parameter space, which compromise the robustness of confidence interval computations at 20 meters. At the 20-meter depth clear water scenario CWDB, the violon plots show a consistent and symmetrical CI distribution, with modes closely adhering to the empirical Monte Carlo-derived confidence bounds, and an insignificant bias.

However, particularly for the TWDB parameterization in turbid and optically complex waters at a depth of 15 meters, noticeable disparities arise among the performance of the test statistics. As demonstrated in Figure 4.9b, while the r statistic continues to exhibit robustness, a slight bias is evident in the other test statistics, where the modes of their confidence bounds are discernibly shifted away from the Monte Carlo derived quantiles. Additionally, for the TWDB parameterization at 15 meters, the bias is not only evident in the shift of the 95% CI modes but also in the pronounced skewness. This skewness is particularly noticeable around the upper bounds of the confidence intervals, where the distributions stretch further,

emphasizing the uncertainty in these estimates. Moreover, there is a distinct asymmetry in the tails of the distributions, extending more on one side, indicative of the complex optical conditions at these depths and optical water properties.

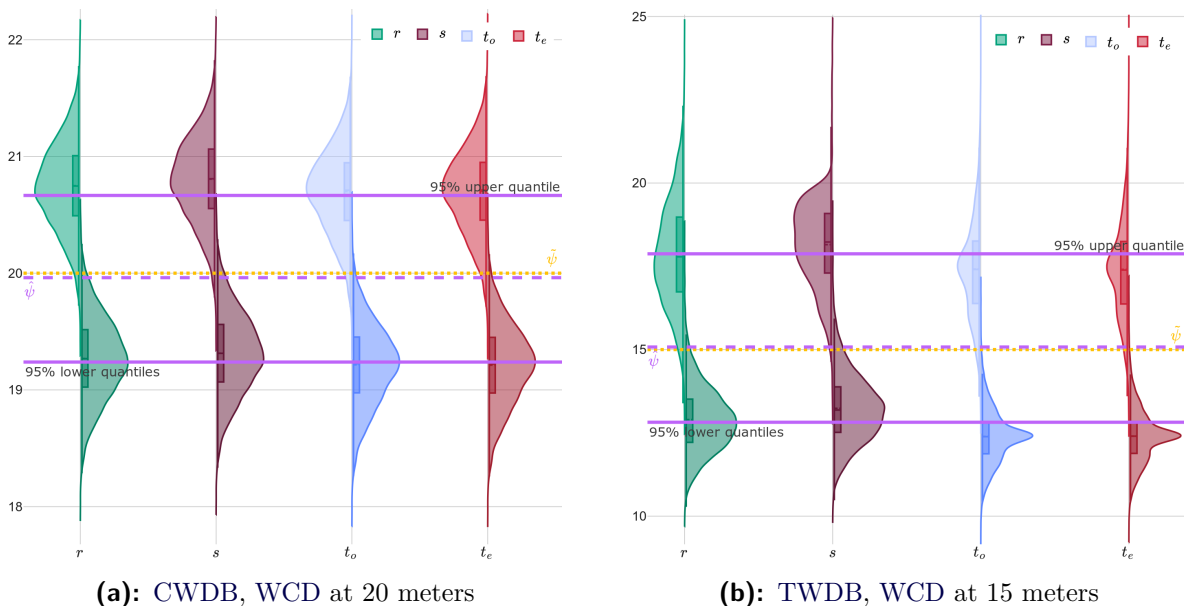


Figure 4.9 – Violin plots illustrating the distribution of computed 95% CI from first order statistical tests for the CWDB scenario at 20 meters (a) and the TWDB scenario at 15 meters (b).

The analysis above indicates that as the water clarity diminishes, the robustness of first-order test statistics may encounter challenges as the depth increases in the hyperspectral setting. This deviation is a clear sign that the water column conditions—characterized by a significant presence of suspended solids or organic matter exert a significant influence on the first-order WCD CI derived from SA models in the hyperspectral setting.

The finding for the hyperspectral scenario in Table 4.6 demonstrates that rejection rates frequently align with the nominal 5% value. This alignment underscores the first-order tests’ efficacy in providing reliable 95% CI for WCD parameters in the presence of semi-analytical nuisance parameters. While some deviations occur, they generally indicate a robust performance across the board. The collective performance of these statistics illustrates an effective framework for evaluating WCD uncertainties with a high degree of reliability in the hyperspectral context.

- The r statistic shows a small deviation from the nominal rejection rate that suggests a moderately superior capability in maintaining an accurate 95% CI coverage probability. It demonstrates a consistent and reliable measure of uncertainty, underscoring its robustness in complex scenarios compared to the other tests.
- The t_o and t_e statistics exhibit closely correlated rejection rates, implying that Wald tests share a similar impact on the estimation’s confidence levels. As in geometric

Table 4.6 – First-order statistical tests performance for the HysPex sensor. Rejection rates colored in red indicate conservative response (uncertainty underestimation) and those in orange indicate liberal response (uncertainty overestimation).

Depth (m)	Parameterization	Rejection rates (%)			
		r	t_o	t_e	s
1.0	CWBB	6.4	4.5	4.4	5.0
	CWDB	6.3	4.7	4.6	5.4
	TWBB	4.7	4.0	2.5	6.3
	TWDB	6.0	3.6	2.1	8.1
5.0	CWBB	4.8	4.8	4.7	4.8
	CWDB	5.1	4.9	4.8	5.1
	TWBB	4.9	5.2	4.3	6.5
	TWDB	4.9	5.2	4.5	6.1
10.0	CWBB	5.2	4.9	4.7	5.4
	CWDB	5.1	4.9	4.8	5.4
	TWBB	5.0	5.2	5.2	4.9
	TWDB	4.9	5.3	5.3	4.9
15.0	CWBB	4.5	4.4	4.3	12.3
	CWDB	4.7	5.2	5.1	5.1
	TWBB	4.6	5.7	5.6	40.5
	TWDB	5.4	5.4	5.4	5.8
20.0	CWBB	4.8	5.6	5.5	5.1
	CWDB	4.5	4.4	4.3	4.7
	TWBB	5.6	7.2	7.0	9.4
	TWDB	5.0	7.6	7.5	10.0

inference chapter findings, this suggests that the variability of the OFIM uncertainty across samples is low, affirming variance-covariance propagation effectiveness in this setup.

- The s statistic shows deviations in specific parameterizations, notably at depths of 15 and 20.0 meters. This is mainly associated to the sensitivity of this test statistic to outliers in complex scenarios.

3.3.2 Multispectral data

The transition to multispectral data highlights the challenges posed by reduced spectral resolution on likelihood-based inference in SA models. Within this context, we delve into statistical

metrics, particularly CI and rejection rates, to discern the effects of spectral granularity on bathymetric uncertainty estimation. In multispectral analysis with the MSI-2 sensor, examining the clear water case (CWBB) at 1 meter, shown in Figure 4.10a, we note an optimal performance where first-order statistics effectively capture the confidence interval bounds. This ideal behavior, however, is observed exclusively in this minimal depth scenario within the simulated conditions presented in Table 4.3.

Extending the analysis to 5 meters under the same CWBB parameterization, as depicted in Figure 4.10b, subtle deviations begin to emerge except for the Wald test t_e which overestimates the WCD significantly. The tests s and observed Wald t_o show a slight displacement of their modes from the Monte Carlo bounds, and a marked asymmetry is noted in the wider distribution of the upper bounds. The broader upper bounds and presence of outliers, particularly noted with the t_o test, suggest complications due to ill-conditioned or nearly singular Fisher information matrices, exacerbated by the multispectral sensor’s reduced spectral resolution compressing complex spectral features into fewer bands.

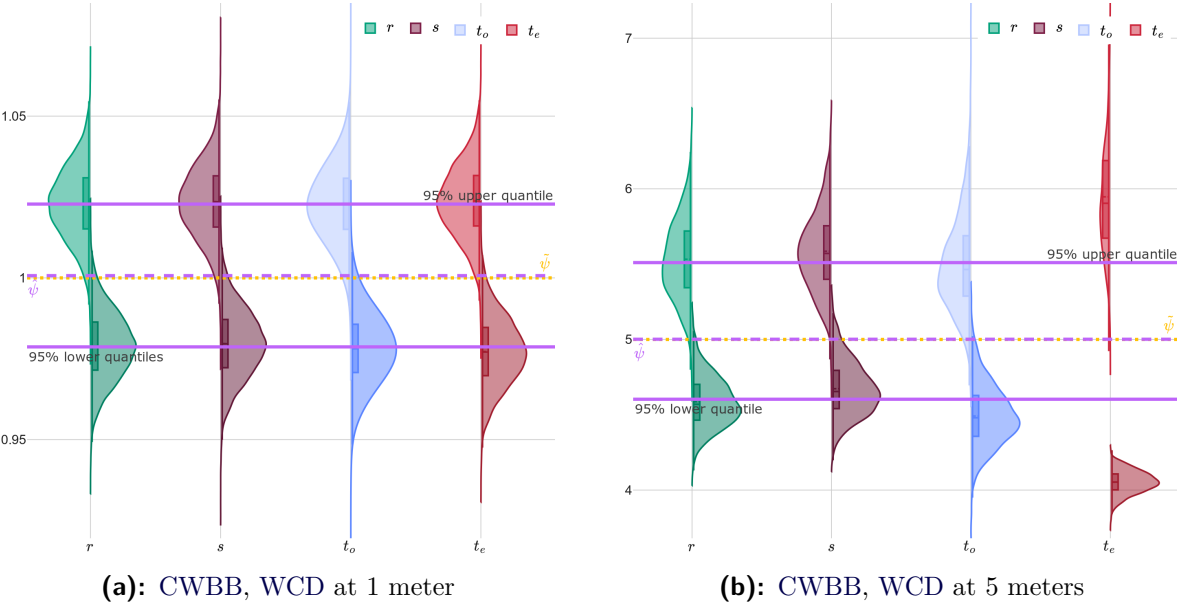


Figure 4.10 – Violin plots illustrating the distribution of computed 95% CI from first-order statistical tests for the CWBB scenario at 1 meter (a) and 5 meters (b) depths.

In a comparative analysis of 95% CI bounds distribution at 1 meter depth under differing seabed conditions, the CWBB scenario exhibits ideal statistical behavior across all metrics. The 95% CI bounds are unbiased and symmetric for all tests, indicating an insignificant performance sensitivity to the seabed variability. However, the observed Wald test t_o in particular displays a wider distribution at both bounds, reflecting the variability of the observed information inherent to this parameterization.

In contrast, for the TWBB considering water condition influence, Figure 4.11b shows similar

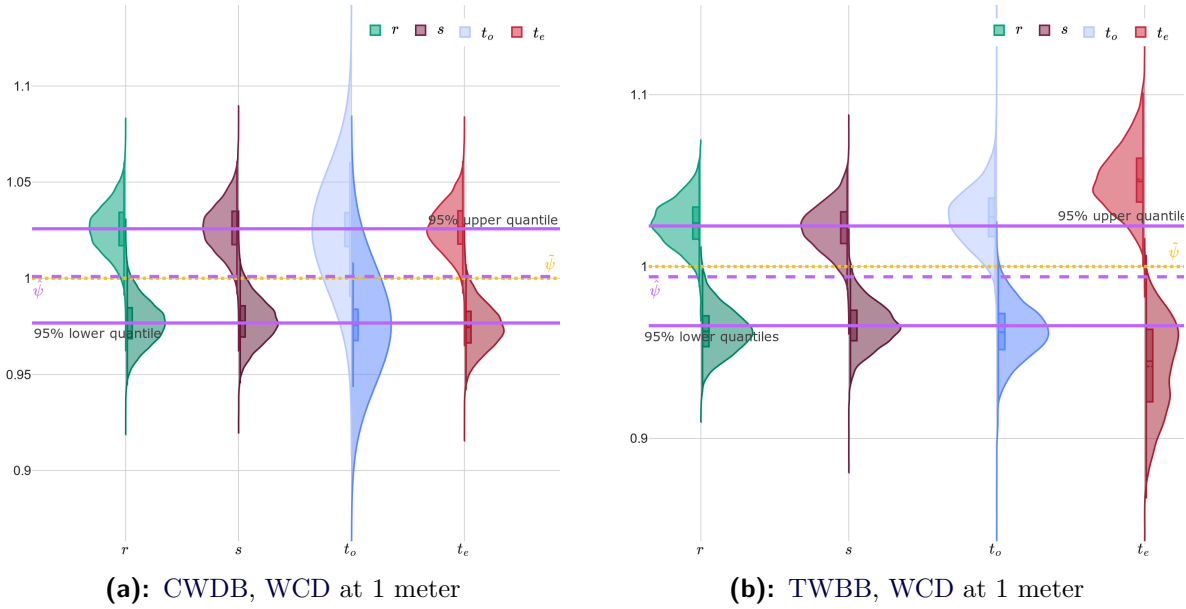


Figure 4.11 – Violin plots illustrating the distribution of computed 95% CI from first-order statistical tests for CWDB (a) and TWBB (b) scenarios at 1 meter depth.

deviations such as those highlighted for the CWBB scenario at 5 meters. Here, the Wald test t_e also overestimates the WCD uncertainty, and t_o exhibits elongated tails, signaling the presence of outliers. This case demonstrates distinct distributions for the tests, with small 95% CI bound bias for the likelihood ratio test r and minimal bias for the score test s . This pattern, more pronounced in hyperspectral data only at depths above 10 meters or under turbid conditions, illustrates the profound impact of reduced spectral resolution.

Following our analysis across different scenarios, we push the diagnosis to extreme cases to expose the limitations of the likelihood ratio and the score tests within the SA models. In the rigorous analysis of extreme cases for multispectral data, the likelihood ratio r test upholds its stature as a reliable estimator, maintaining a negligible bias even amidst the variability of environmental conditions. Figures 4.12b and 4.12a, focused on r and s statistics for the 10-meter TWDB and 20-meter CWDB scenarios, show that the score test s slightly underestimates the WCD uncertainty, with its outliers particularly present at the lower bound. These outliers can be attributed to redundancy of the score outliers as illustrated in Figure 4.7d.

Despite these intricacies, the overall performance affirms the MLE’s reliability, as the slight bias observed is insignificant relative to the broader uncertainty, ensuring the estimator’s credibility. Notably, while the Wald test t_e is present in the full spectrum of the analysis, it is characterized by inflated confidence intervals, with its modes extending beyond the plot’s range, leaving only the tails visible within the figures. This depiction highlights the challenges in accurately capturing confidence intervals in such complex modeling scenarios and

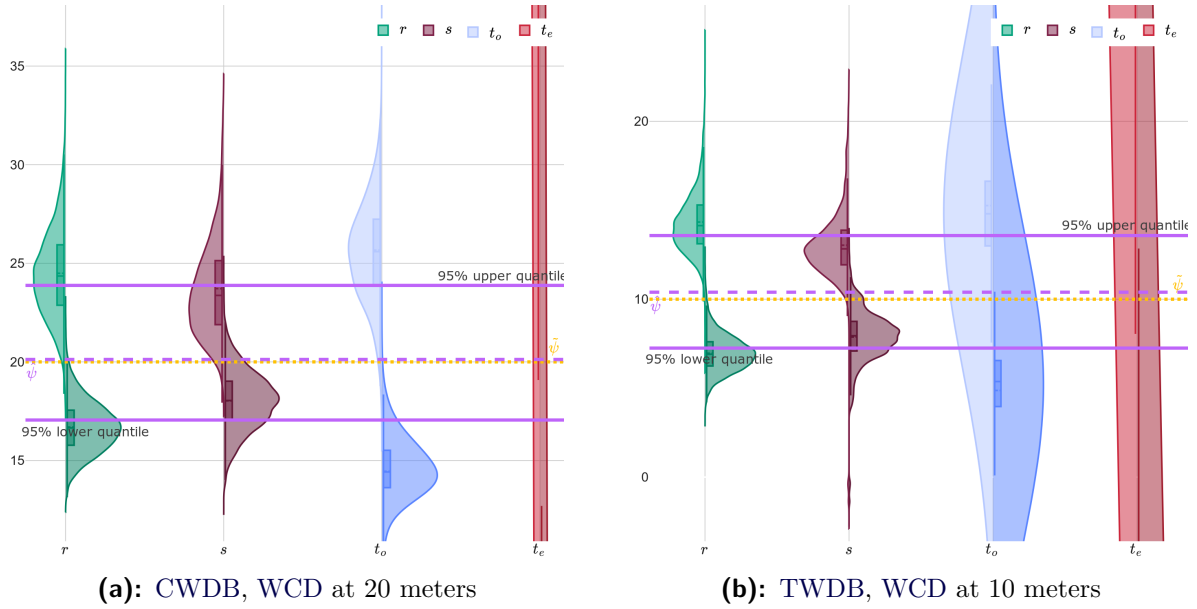


Figure 4.12 – Violin plots illustrating the distribution of computed 95% CI from first-order statistical tests for CWDB (a) and TWDB (b) scenarios at 20 meters and 10 meters respectively. The Figure notations are the same as those detailed in Figure 4.1.

underscores the importance of nuanced statistical evaluation in semi-analytical bathymetric modeling.

For the CWDB case at lower depths, t_o slightly overestimates the WCD, indicating a minor deviation from optimal performance. Notably, unlike in hyperspectral scenarios where the MLE typically aligns closely with the true depth, in multispectral settings, there is a consistent slight overestimation of the true depth by the MLE. This bias, while small, underscores the influence of reduced spectral resolution on the precision of bathymetric estimations, further emphasizing the need for careful calibration and validation of SA models under varying environmental conditions and sensor capabilities. The assessment of the MSI-2 sensor’s performance presented in Table 4.7 for WCD uncertainty evaluation reveals distinct outcomes compared to the hyperspectral data analysis. Notably, the rejection rates of first-order statistical tests (r , t_o , t_e , and s) exhibit a divergence from the anticipated nominal 5% value, underscoring a broader variability in the efficacy of these tests within the multispectral data context.

- The r statistic’s rejection rates are often close to the nominal 5%. However low rejection rates in challenging conditions suggest conservative 95% CI that may extend beyond the necessary bounds for certain water conditions. This tendency towards conservative estimations underscores the need for a nuanced interpretation of r in the multispectral analysis.
- A noticeable performance gap between the t_o and t_e statistics is observed, with t_o demonstrating a more accurate representation of uncertainty except for turbid waters

with depth greater than 5 meters. In contrast, t_e struggles to capture the WCD uncertainty particularly in scenarios involving complex water compositions and depths.

- The s statistic exhibits heightened rejection rates in specific configurations, notably under the TWDB parameterization, indicating a potential underestimation of uncertainty.

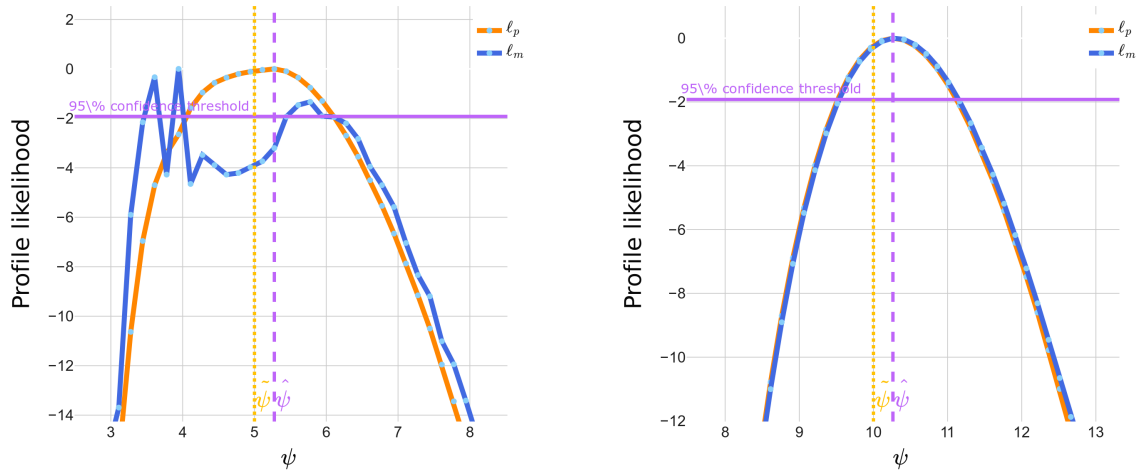
Table 4.7 – First-order statistical tests rejection rates for the MSI-2 sensor.

Depth (m)	Parameterization	Rejection Rates (%)			
		r	t_o	t_e	s
1.0	CWBB	5.0	5.8	3.8	6.1
	CWDB	5.0	5.6	4.0	6.2
	TWBB	3.1	5.4	3.8	6.5
	TWDB	4.3	6.6	4.5	6.7
5.0	CWBB	3.1	5.2	0.0	6.5
	CWDB	3.0	5.1	0.1	5.6
	TWBB	2.1	9.8	3.0	5.5
	TWDB	2.1	8.9	2.3	28.4
10.0	CWBB	1.4	4.8	50.0	17.5
	CWDB	1.9	7.6	50.0	22.1
	TWBB	0.8	16.3	49.9	15.6
	TWDB	1.2	14.4	49.8	13.9
15.0	CWBB	1.8	5.1	74.9	21.0
	CWDB	1.9	4.6	75.3	17.7
	TWBB	0.8	26.2	52.7	94.8
	TWDB	52.2	46.5	53.1	64.2
20.0	CWBB	2.7	4.9	74.9	14.6
	CWDB	2.5	5.0	75.2	13.5
	TWBB	28.4	52.0	54.1	32.4
	TWDB	30.9	52.3	54.7	35.8

3.4 Second-order inference results

The exploration of first-order inference has demonstrated its effectiveness under certain conditions, yet it has also highlighted the potential gains of implementing second-order adjustments in challenging optical scenarios, particularly when working with multispectral data. These scenarios often yield complex likelihood profiles and pose optimization challenges, hindering precise uncertainty quantification.

In most of the scenarios, the adjusted profile likelihood ℓ_m was found to be highly sensitive to outliers near the MLE such as those highlighted in Section 3.2.1.d. This sensitivity often led to multiple intersections in the adjusted curves and misinterpretations of confidence intervals, as illustrated in Figures 4.13a for a multispectral scenario with turbid waters at 5 meters.



(a): Profile likelihood and second-order adjustments for the multispectral scenario TWDB at 5 meters.

(b): Smooth second-order adjustments on the profile likelihood for the hyperspectral scenario TWDB at 5 meters.

Figure 4.13 – Second-order adjustments in multispectral (a) and hyperspectral (b) data for the scenario TWDB at 5 meters.

However, a contrasting scenario was observed in the hyperspectral data for turbid waters (TWDB) where high concentrations of water constituents ensures their identifiability, avoiding singularities in the terms necessary for computing adjustments. The adjusted profile for this scenario is smooth, as shown in Figure 4.13b. Interestingly, among all the evaluated scenarios presented in Table 4.1, only the turbid waters cases modeled for the hyperspectral sensor provided a suitable environment for deriving second-order adjustments without the complicating influence of outliers. The case depicted in Figure 4.13b exemplifies these favorable conditions under the hyperspectral context for the TWDB scenario at a depth of 5 meters. The smooth second-order adjustments on the profile likelihood in this case, yielded an adjusted likelihood ratio with a rejection rate of 5.0%, closely aligning with the original likelihood ratio performance of 4.9%. This result indicates that when first-order methods perform well, second-order adjustments, when applicable, should theoretically align with these outcomes. However, from a practical standpoint, there is no compelling need for second-order adjustments in scenarios where first-order methods have already proven effective. The limited scope for validating the potential of second-order adjustments arises due to the presence of outliers and singularities in settings where the likelihood ratio underperforms, thus reducing the opportunities to assess the true benefits of second-order corrections in relevant scenarios.

However, the fact that second-order adjustments were not validated in more complex scenarios does not discount the inherent limitations of first-order methods in these situations. This is evidenced by the previously established small sample effects, which are evident in the flatness and asymmetry of the likelihood surface observed in our first-order results, particularly under the challenging conditions prevalent in these regions with sparse statistical information.

4 Discussion

The findings in this study provided a detailed exploration of the utilization of likelihood-based inference for evaluating bathymetric uncertainties within SA models, with a special emphasis on the influence of environmental factors and the sensor’s spectral resolution on the uncertainties of WCD.

The exploration of first-order inference results presents an assessment of the reliability and limitations of statistical methods within the realm of radiometric inference for WCD. In the realm of SA WCD uncertainty evaluation, earlier work by [15] has indicated that for platforms like Sentinel-2A, which we also simulated, variance-covariance or equivalently Cramér-Rao bounds can dramatically increase under certain conditions, specifically at depths beyond 5 meters. Our findings suggest that going beyond the limits of traditional approaches—its performance through more sophisticated asymptotic analysis—provides a more accurate and reliable framework for capturing the nuances of SA models uncertainties. This not only aligns with theoretical expectations but also offers practical advantages in terms of computational feasibility and interpretability, especially in scenarios with significant environmental complexity. While [120]’s method serves to tame the often inflated uncertainty estimates associated with the expected information in the Wald test t_o , it can be seen as artificially constraining the estimator’s variance. Conversely, our comprehensive evaluation of asymptotic performance across various statistical tests (i.e., r , s , and t_o) demonstrates an enhanced capacity to capture the complexities and asymmetries inherent in SA models.

Notably, hyperspectral data emerges as a more conducive medium for the application of first-order statistics, exhibiting favorable outcomes that underscore the adequacy of the variance-covariance framework for uncertainty evaluation in such contexts. In contrast, we show the inefficacy of applying variance-covariance methods or more generally first-order statistical tests, indiscriminately within multispectral settings, and signal the need for cautious interpretation when considering the influence of water column optical properties and seabed characteristics on the WCD uncertainty. The findings for the EFIM based Wald test t_e suggest that while the variance-covariance approach remains a viable method for uncertainty quantification, practitioners should proceed with caution in these environments due to the heightened potential for misestimation of WCD uncertainties. Remarkably, multispectral data presents

a challenging landscape for the application of first-order asymptotic theory, revealing variable performance across different statistical tests. Notable concerns are: **WCD** uncertainty asymmetry, practical identifiability issues, uncertainty overestimation by the Wald tests, sensitivity of the score test to outliers. These encountered challenges contribute to a deviation from optimal uncertainty assessment practices. However, the likelihood ratio test, which has proven its robustness in both geometric and radiometric inference, stands out for its ability to accommodate asymmetrical **CI**—an attribute particularly relevant for multispectral data used in nonlinear **SA** models.

The benefits of **MLE** refinement through profiling extend beyond the scope of our controlled experiments, which were initiated from true parameters. In practical scenarios, the reliance on global optimizers may not be the most efficient approach due to the vast volume and ongoing collection of spectral data, which can impede performance due to computational constraints. Consequently, the quality of parameter estimation often hinges on the choice of the optimizer and its initial conditions [106], which frequently results in a suboptimal medium for likelihood-based inference. As demonstrated in our findings, refining the **WCD MLE** through profiling allows us to navigate around these initial suboptimal conditions. Most scenarios within our experimental domain exhibited little to no bias, satisfying the first-order asymptotic properties of the **MLE**. Notably, the likelihood ratio test r consistently demonstrated good statistical performance, underscoring the robustness of the refined **MLE**. This was particularly evident as we employed non-bounded optimizations, contrasting with many studies on **SA** models including those addressing local minima issues. These results indicate that the common problems associated with local minima in **SA** models can be effectively mitigated through profiling, which not only enhances the accuracy of **MLE** but also enables a more precise evaluation of uncertainties as demonstrated for the Wald tests. This dual advantage is achieved with fewer constraints compared to methods like bootstrapping or reliance on multiple initializations, which can be computationally demanding and subjective, especially when applied to large spectral datacubes. By streamlining the optimization process and reducing reliance on extensive resampling, profiling presents a cost-effective and efficient solution to the challenges of **SA** model inference.

The examination of second-order adjustments from higher-order asymptotic theory was undertaken with the intent to sharpen the estimation of uncertainty, particularly by addressing the performance of likelihood ratio adjustments. While these modifications maintained consistent performance in optimal conditions, such as with hyperspectral data and in clear water scenarios—environments where the likelihood ratio already perform well—they faltered under more challenging circumstances. Notably, in low information samples, which inherently strain optimizer capabilities, the adjustments proved to be overly sensitive, diminishing their utility precisely when robust interventions are most needed. This outcome, somewhat paradoxical, underlines the nuanced balance between theoretical enhancements and their practical appli-

cation. Despite this, pursuing such adjustments marks a significant stride towards a more nuanced understanding and handling of uncertainties within SA models, signaling a complex yet crucial pathway for future methodological advancements in accurately quantifying uncertainties.

5 Chapter conclusion

This chapter’s investigation into likelihood-based inference for bathymetric uncertainties within SA models illuminates the intricate balance between theoretical precision and the pragmatic challenges encountered in real-world environmental monitoring. Through rigorous examination of first and second-order inference, profiling refinement, and the distinct performance across hyperspectral and multispectral data, this study underscores the complexity of accurately estimating WCD and its associated uncertainties.

The refined application of MLE through profiling emerged as a crucial technique, enhancing the robustness of parameter estimation under the diverse conditions presented by SA models. This methodology, proven effective across both idealized and challenging initial conditions, offers a pivotal advancement in the optimization landscape, particularly valuable in the complex environments typical of bathymetric mapping where multiple nuisance factors may be involved.

The analysis reveals that while hyperspectral data offers a favorable platform for the application of first-order statistical tests, ensuring reliable variance-covariance-based uncertainty evaluation, multispectral data presents significant challenges. The variability in the performance of statistical tests within multispectral analysis underscores the necessity for cautious interpretation and application, particularly in optically complex waters where overestimation of uncertainties may occur.

Furthermore, the exploration into second-order inference adjustments highlights the nuanced interplay between theoretical enhancements and their practical efficacy. While these adjustments maintain consistency in optimal conditions, their utility diminishes in low-information scenarios, underscoring the limitations of current statistical methods in addressing the inherent challenges of SA models.

In conclusion, this research advocates for a methodical and cautious approach to the application of statistical inference within SA models, emphasizing the need for further advancements to accurately quantify uncertainties.

Chapter 5

Conclusion

This dissertation advances bathymetric mapping by developing and applying methodologies to rigorously evaluate uncertainties in **WCD** estimations from passive imagery, using both geometric and radiometric analyses. This research highlights the critical yet often overlooked role of uncertainty in spectral imagery-based **WCD** estimation. Starting from foundational concepts outlined in Chapter 1 on spectral imagery characteristics and estimation methods, the study has filled significant gaps in the literature by effectively demonstrating the suitability of a likelihood-based framework for estimating and characterizing **WCD** uncertainties.

The methodology employs **MLE** as the central estimator within a likelihood framework, forming the backbone of our analysis as detailed in Chapter 2. This includes traditional approaches like the variance-covariance method and introduces higher-order extensions to enhance inference accuracy in small samples. These innovations underscore the thesis's contributions to improving the reliability of **WCD** uncertainties evaluation.

In this concluding chapter, we revisit our research objectives, examining the outcomes of geometric and radiometric inferences and discussing their broader implications. We reflect on the journey of this research and its place in the field, setting the stage for future contributions to bathymetric mapping. This final overview not only showcases the impact of our work but also highlights its potential to inform future research and practical applications in the field.

1 Revisiting research objectives

This research aimed to advance the understanding and methodology of inferring **WCD** from spectral imagery, with a specific focus on the critical role of uncertainty in its estimation. Our specific objectives were defined as follows:

1. Design a geometric inferential model adapted to stereo-photogrammetric triangulation,

allowing for the evaluation of **WCD** uncertainties within the likelihood framework.

2. Design a radiometric inferential approach that utilizes **RT** modeling, including **SA** models, to facilitate the evaluation of **WCD** uncertainties within likelihood framework.

Each objective laid out at the outset of this thesis has been addressed thoroughly across different chapters, highlighting both theoretical advancements and practical applications.

1.1 Geometric **WCD** inference

This study successfully designed a geometric inferential model adapted to stereo-photogrammetric triangulation, allowing for the comprehensive evaluation of **WCD** uncertainties within a likelihood framework, as outlined in our specific objectives. **WCD** geometric inference, specifically addressed in Chapter 3, involved the development and application of a novel triangulation method tailored for evaluating geometric uncertainties in through-water photogrammetry. This approach explicitly accounts for the refraction of light within the water body, a critical factor that is often addressed either with posterior corrections or implicitly in the current approaches. In the geometric analysis, the **MLE** estimator's evaluation hinged primarily on two statistical tests: the observed Wald test and the likelihood ratio. The observed Wald test exhibited strong performance and low variability to resampling, especially when high-quality sensor poses were used, affirming the sufficiency of traditional variance-covariance methods commonly upheld in photogrammetric literature. This confirmed the reliability of established methods in optimal settings, where precision in bathymetric estimations is critical.

Conversely, the likelihood ratio demonstrated a robust performance, particularly when addressing noisy data. Its resilience was most noticeable in challenging scenarios marked by lower quality sensor poses and higher flight altitudes, where traditional methods often falter. The performance of the likelihood ratio, particularly demonstrated by its robust coverage probability, ensures that first-order inference is sufficiently rigorous for geometric analysis, especially in hydrographic applications. This obviates the need for higher-order inference investigations, aligning with the industry consensus that survey-grade navigation and optical sensors typically require precision achievable through established first-order methods. This approach not only confirms the robustness of our statistical framework but also supports its practical application in hydrography, where reliability and accuracy are paramount.

An additional notable findings from our geometric analysis is the ability inference of the water interface position without ancillary tide or wave information. This finding underscores the effectiveness of the proposed pushbroom sensor imagery techniques, particularly when implemented with cross-line flight patterns. This offers the ability to identify the geometric influence of water refraction and derive bathymetric maps solely relying on passive imagery. Such advancements in methodological strategies highlight a forward path in hydrographic

survey techniques, where detailed planning and sensor configuration play pivotal roles in data acquisition efficacy.

However, our study encountered several limitations that restrict the full realization of its potential. Primarily, the study did not address the integration of overlap in both across and along flight directions. Such redundancy in the geometric data is typically expected in multi-view geometry to increase sensor pose samples and reduce uncertainty in triangulation. While the focus on maintaining a uniform analysis across sensor poses facilitated a direct comparison of the effects of stereo geometry, it also limited the scope to scenarios typically reliant on stereo-pair configurations in photogrammetric studies.

Moreover, the research was confined to sensor pose modeling and did not extend to a comprehensive geometric modeling of light rays, which can vary significantly with different sensor technologies. For instance, frame cameras can track geometric distortions through internal calibration more readily than pushbroom sensors, which might require more extensive modeling. However, these aspects can be effectively integrated into the likelihood-based framework employed in this study, suggesting a path for future enhancements.

1.2 Radiometric WCD inference

In addressing the second objective, our study successfully designed a radiometric inferential approach utilizing **RT** modeling and **SA** models within a likelihood framework. The adoption of **SA** models was strategic, facilitating direct parameter inference from observational data which inherently aligns with the methodological need to handle uncertainties more coherently. This approach allows for an adaptable and direct evaluation of **WCD** uncertainties, distinguishing it from empirical or machine learning methods that often rely on indirect parameter prediction.

Comprehensive spectral details of hyperspectral data aligned well with **MLE** large sample properties, enabling effective use of first-order statistical measures such as the Wald tests for reliable uncertainty estimation. These capabilities proved advantageous even in moderately complex water column conditions, affirming the robustness of traditional approaches for hyperspectral analysis.

Conversely, multispectral data, constrained by its limited spectral resolution, often resembles a small-sample scenario, posing significant challenges for traditional statistical methods except in optimal conditions such as clear waters and shallow depths. Under less than ideal circumstances, the variability in water column content significantly affects the performance of statistical tests. Notably, the likelihood ratio test showcased resilience and adaptability, emerging as a robust method for managing uncertainties in more complex aquatic environments. Despite its strengths, the test revealed deviations from assumed large-sample prop-

erties, such as characteristic asymmetry and practical identifiability issues, underscoring the necessity for confidence intervals over traditional variance metrics in uncertainty assessments.

The findings highlight the need for refined statistical methods capable of integrating the unique complexities presented by multispectral data into bathymetric estimations. It also underscores the importance of continuous, granular management of uncertainty tailored to specific environmental conditions and dataset characteristics, possibly extending to per-pixel analyses in other imagery research fields.

The refinement of **MLE** through profiling has significantly bolstered the robustness of uncertainty estimations across varying environmental conditions, marking a pivotal advancement in handling **SA** model challenges. Profiling effectively countered the limitations posed by local minima in most of the scenarios, showcasing its utility across different optimization settings. Additionally, the superiority of the likelihood ratio can be leveraged in handling the **SA** parameters other than **WCD** which argues in favor of its adoption over traditional variance-covariance methods in coastal studies.

Although the study effectively implemented these models within the specified framework, it predominantly utilized simplistic homoscedastic error assumptions. This simplification in error modeling could be seen as a starting point rather than a limitation, suggesting that future work could expand to include heteroscedastic or correlated errors. Addressing this could enhance the robustness of the findings and further affirm the adaptability of the inferential methods used, providing a solid foundation for more detailed uncertainty assessments in radiometric water column depth inference. These limitations encountered in applying first-order statistical tests in multispectral analysis and the challenges of profiling under low-information scenarios suggest avenues for future research. These include the development of more adaptive and resilient inference methods that can handle the complexities of **SA** models more effectively, particularly in optically complex waters.

2 Implications for future research

Our work on **WCD** uncertainties has laid a foundational step towards enhancing the understanding and application of statistical methods in the estimation of bathymetric uncertainties from spectral imagery. The insights gained from the application of likelihood-based inference provide a valuable guide for future studies aiming to refine these techniques further.

By simulating known data-generating processes, the thesis demonstrates the capability of inference methods to inform the limits of traditional approaches in small sample scenarios, thus emphasizing the value of simulation-based research challenging the prevalent bias towards real data which may obscure the diversity and nuance of scientific findings. By focusing on

the meticulous evaluation of uncertainty either in geometric or radiometric analysis, this work paves the way toward more accurate and reliable bathymetric uncertainty products, essential for the sustainable management of marine and coastal ecosystems.

2.1 Practical applications

This thesis opens several avenues for future research, particularly in the application of likelihood-based inference frameworks to real-world datasets.

2.1.1 Application to real datasets

Throughout this thesis, the methodologies developed for evaluating **WCD** uncertainties have been rigorously tested under controlled conditions, remote sensing reflectance data for radiometric inference and sensor pose data for geometric inference. These controlled experiments have proven essential for demonstrating the efficacy and limits of the likelihood-based inference framework. However, the transition to real-world applications presents its own set of challenges and opportunities.

1. Real-world spectral imagery, especially of coastal areas, remains scarce. High-resolution satellite stereo pairs, which could dramatically improve the resolution and accuracy of **WCD** estimations, are not openly accessible. Furthermore, in-situ data are often limited and present calibration challenges such as **AC** correction, as discussed in Chapter 1. These issues complicate the application of our methodologies to real datasets but do not diminish their potential impact.
2. The calibration of errors and the adjustment for biases are critical when applying our models to real datasets. Our methodology assumes that the statistical model is representative of the data-generating process and accounts for various random factors within the data. Should any biases exist, profiling techniques can be leveraged to adjust for these biases, as demonstrated in our approach to **WAI** height geometric inference addressing the refraction systematic bias as well as its uncertainties through the likelihood ratio. This adjustment process is essential for ensuring that the inferential methods remain valid under practical conditions.

Despite these challenges, there is confidence that our methodology for retrieving **WCD** uncertainties, which has been verified under well-known models, can be applied effectively to real datasets.

2.1.2 Integration with existing technologies

Incorporating the inferential methods developed in this thesis with remote sensing technologies, such as drones and satellites, offers significant enhancements in data accuracy for applications.

From our study, we noted that while geometric **WCD** inference demonstrated the adequacy of variance as a metric of uncertainty, radiometric inference—especially using multispectral data which is prevalent in satellite imagery—highlighted the limitations in defining upper bounds of uncertainty. This suggests an innovative approach for **Geographic Information Systems (GIS)** integration where uncertainties are represented as two raster bands for 95% confidence intervals, potentially including missing values where practical unidentifiability occurs. This method, although complex, provides a comprehensive view of uncertainties but must be balanced with considerations for data storage and readability.

Additionally, the integration of our statistical models can benefit optical sensing technologies such as topobathymetric **LiDAR**, which primarily uses geometric inference. These technologies can greatly benefit from enhanced statistical modeling to address their known limitations in optically complex waters. Moreover, integrating frame and pushbroom sensor data could significantly improve geometric accuracy while enabling access to fine spectral resolution and higher **SNR**, which is particularly valuable in coastal areas where acquiring ground control points is challenging. Frame imagery, with its inherent geometric precision, can complement pushbroom sensor data to optimize bathymetric mapping in these critical zones. Video frame imagery emerges as a particularly promising avenue, especially since it can provide extensive overlap between images, which might enable detailed seabed mapping by granularly resolving the water-air interface effects such as sunglint and wave distortions. This capability was underscored in our study on geometric inference, which demonstrated the ability to resolve the average **WAI** height and enhance its inference through redundancy. As the technology for multispectral and hyperspectral video imaging continues to mature, video frame data—predominantly in **RGB** format—provides a fertile ground for applying computer vision techniques. Coupled with a likelihood framework, these methods can be tailored to exploit the rich data from video frames, designing novel statistical models that effectively retrieve uncertainties in geometric parameters. This integration not only leverages the inherent geometric precision of frame imagery but also optimizes the bathymetric mapping process in crucial maritime zones.

To maximize the impact of our research, we recommend the integration of likelihood-based inference in advanced uncertainty guides and training programs for practitioners. The statistical methods and tools developed throughout this study can be used to supply professionals with the knowledge to tackle environmental parameters uncertainties effectively.

2.2 Integrated approaches

The integration of geometric and radiometric WCD inference presents a promising strategy to mitigate the shortcomings of each method while enhancing the overall robustness and accuracy of bathymetric mapping. This approach is particularly valuable in addressing the limitations encountered when each type of inference is applied in isolation. For instance, radiometric inferences using multispectral data often yield asymmetric or non-identifiable upper bounds. In such scenarios, incorporating geometric data—characterized by parabolic profiles at depths greater than 15 meters—can significantly refine these upper bounds. By integrating radiometric and geometric information, particularly at feature points where the radiometric inference lacks defined upper bounds, it is possible to establish comprehensive confidence bounds, thereby enhancing the certainty and reliability of the estimations.

Conversely, geometric inference, which may fail in non-textured environments, can be substantially bolstered by incorporating radiometric information. This mutual support not only aids in overcoming the respective limitations of each method but also facilitates a more nuanced integration of data. For example, geometric data can be utilized to obtain or refine prior assessments of water column characteristics which can be practically beneficial in clear water conditions, enhancing the precision of radiometric measurements. Similarly, radiometric data can be instrumental in determining and adjusting for geometric biases, aiding in the intercalibration of various data aspects.

Integrated approaches can be fully implemented on the basis of the likelihood-based inference, involving strategies where nuisance parameters are managed more effectively. By leveraging geometric information to investigate prior water column characteristics or using radiometric data to assist in determining geometric biases, we can ensure a more coherent and accurate bathymetric assessment. However, it is crucial to acknowledge that such approaches are also subject to the limitations inherent to each class of data—geometric and radiometric—such as calibration errors, systematic offsets, and environmental complexities. To rigorously implement these integrated approaches and truly benefit from their potential, there is a need for joint characterization of the spectral data, encompassing both geometric and radiometric dimensions. This comprehensive approach not only enhances data integrity but also provides a stronger basis for implementing these integration approaches, enhancing the reliability of bathymetric mapping in challenging marine and coastal settings.

2.2.1 Expanded application of likelihood-based inference

The uncertainty estimation grounded in likelihood-based inference and developed in this thesis for the optically-derived WCD are adaptable to various fields beyond bathymetric mapping, including coastal zone management, environmental monitoring, and marine resource manage-

ment. These areas often encounter problems similar to those in bathymetric estimations, such as pixel-dependent mapping, inversion problems, limited prior information, and the susceptibility of traditional variance-covariance methods under complex conditions.

The robustness of non-traditional statistical approaches like the likelihood ratio and observed information methods in our bathymetric studies suggests they could effectively manage uncertainties in these expanded domains. However, it's essential to simulate the specific data-generating processes of these application areas first. This simulation-based validation helps diagnose uncertainty evaluation or estimator performance, allowing to verify that standard variance-covariance practices are effective.

When the interest is investigating the robustness of uncertainties evaluation, 'model before data' strategy is recommended when adapting our methodologies to new fields. By rigorously testing the statistical models under controlled, simulated conditions, we ensure that they are adapted accurately to handle the complexities of new environments. This approach mitigates risks associated with model misfit or data inadequacies, enhancing the precision and reliability of assessments, which is crucial for supporting sustainable practices and informed decision-making in environmental and resource management.

3 Final perspectives

In this manuscript, we have focused intensively on per-pixel or per-feature analysis within both radiometric and geometric dimensions of bathymetric mapping. Looking forward, it's crucial to explore how we might expand our methodologies to more effectively aggregate and interpret these data. By synthesizing information across different classes (radiometric or geometric), within the same image to identify autocorrelated pixels, or across overlapping images from different surveys, we can enhance the clarity and accuracy of our environmental assessments.

Neural radiance fields and variational inference represent two such forward-thinking approaches. Neural radiance fields, for instance, could be adapted to underwater imaging by accommodating the specific optical properties of water, such as refraction [122; 123]. This adaptation could vastly improve our ability to render three-dimensional representations of underwater scenes from 2D spectral frame imagery, offering detailed insights into both the water column content and seabed characteristics.

Meanwhile, variational inference, a technique grounded in the principles of likelihood-based inference, offers a way to efficiently handle the complexities of large datasets typical in spectral imagery [124]. By approximating probability densities through optimization, variational inference can be used to integrate or intercalibrate different types of data, supporting more

coherent and computationally feasible analyses.

Additionally, targeted maximum likelihood estimation which is often associated with causal inference, may lead to creative approaches for refining the inference of **WCD** in our context [125]. By targeting the estimation process towards the **WCD**, targeted maximum likelihood estimation related mechanisms can be borrowed to help isolate and address specific uncertainties, enhancing the precision of our mapping efforts.

These innovative methodologies suggest a vibrant future for bathymetric mapping, where data from various sources and perspectives can be integrated more effectively. This not only improves the data's integrity but also aids in crafting more informed strategies for managing and preserving our marine and coastal environments.

For a detailed list of all related academic and professional activities during the course of this research, please refer to Table B.1.

Appendix A

1 GUM methodology for uncertainty

The GUM provides a general and practical methodology to estimate the combined uncertainty of measurements [70]. The methodology for evaluating and expressing the uncertainty of a measurement is summarized in the following steps:

1. Describe the mathematical relationship f between measurements and input quantities:

$$Y = f(X_1, X_2, \dots, X_N) \quad (\text{A.1})$$

Y and X_i are implicitly treated as random variables of which the realization is noted y and x_i respectively. The function f should contain corrections and correction factors, that can contribute to a significant component of uncertainty to the result of the measurements.

2. Determine x_i , the estimated value of input quantity X_i , either on the basis of the statistical analysis of series of observations or by other means.
3. Evaluate the standard uncertainty $u(x_i)$ of each input estimate x_i .
4. Evaluate the covariances associated with any input estimates if they are correlated.
5. Compute the result of the measurements, that is, the estimate y of the measurand Y , from the functional relationship f using for the input quantities X_i the estimates x_i .
6. Determine the combined standard uncertainty $u_c(y)$ of the measurement result y from the standard uncertainties and covariances associated with the input estimates.

$$u_c(y) = \frac{1}{n} \sqrt{\sum_{i=1}^{i=n} \frac{\partial f}{\partial x_i}^2 u_c^2(x_i)} \quad (\text{A.2})$$

If the measurement determines simultaneously more than one output quantity, calculate their covariances.

7. If it is necessary to give an expanded uncertainty U , whose purpose is to provide an interval $y - U$ to $y + U$ that may be expected to encompass a large fraction of the distribution of values that could reasonably be attributed to the measurement Y , multiply the combined standard uncertainty $u_c(y)$ by a coverage factor k , typically in the range 2 to 3, to obtain $U = k_c(y)$. Select k on the basis of the level of confidence required of the interval.
8. Report the result of the measurements y together with its combined standard uncertainty $u_c(y)$ or expanded uncertainty U as discussed in the seventh step and describe how y and $u_c(y)$ or U were obtained.

1.1 Variance-covariance matrix in linear and non-linear models

Consider the linear model defined as:

$$\mathbf{y} = \mathbf{A}\boldsymbol{\theta} + \boldsymbol{\epsilon} \quad (\text{A.3})$$

where \mathbf{y} is the response vector, \mathbf{A} is the design matrix, $\boldsymbol{\theta}$ is the parameter vector, and $\boldsymbol{\epsilon}$ is the error vector with covariance matrix $\boldsymbol{\Sigma}_y$.

The LS estimator $\hat{\boldsymbol{\theta}}$ for the linear model is given by:

$$\hat{\boldsymbol{\theta}} = (\mathbf{A}^T \boldsymbol{\Sigma}_y^{-1} \mathbf{A})^{-1} \mathbf{A}^T \boldsymbol{\Sigma}_y^{-1} \mathbf{y} \quad (\text{A.4})$$

The variance-covariance matrix of $\hat{\boldsymbol{\theta}}$ is:

$$\boldsymbol{\Sigma}_{\hat{\boldsymbol{\theta}}} = (\mathbf{A}^T \boldsymbol{\Sigma}_y^{-1} \mathbf{A})^{-1} \quad (\text{A.5})$$

For a non-linear model, the relationship is defined as:

$$\mathbf{y} = \boldsymbol{\eta}(\boldsymbol{\theta}) + \boldsymbol{\epsilon} \quad (\text{A.6})$$

Linearizing the non-linear function $\boldsymbol{\eta}(\boldsymbol{\theta})$ around the estimated parameters $\hat{\boldsymbol{\theta}}$ using a Taylor series expansion, we get:

$$\boldsymbol{\eta}(\boldsymbol{\theta}) \approx \boldsymbol{\eta}(\hat{\boldsymbol{\theta}}) + \mathbf{J}(\boldsymbol{\theta} - \hat{\boldsymbol{\theta}}) \quad (\text{A.7})$$

where \mathbf{J} is the Jacobian matrix of $\boldsymbol{\eta}$ evaluated at $\hat{\boldsymbol{\theta}}$.

The approximation of the variance-covariance matrix in the non-linear case is then given by:

$$\boldsymbol{\Sigma}_{\hat{\boldsymbol{\theta}}} \approx (\mathbf{J}^T \boldsymbol{\Sigma}_y^{-1} \mathbf{J})^{-1} \quad (\text{A.8})$$

where \mathbf{J} is the Jacobian matrix of partial derivatives of $\boldsymbol{\eta}(\boldsymbol{\theta})$ with respect to the parameters $\boldsymbol{\theta}$ evaluated at $\hat{\boldsymbol{\theta}}$. This expression for the variance-covariance matrix is equivalent to the inverse of the EFIM at the MLE, known from the theory of Gaussian errors [74], Section 3.9.

Under the assumption of Gaussian errors, MLE for the parameter vector $\boldsymbol{\theta}$ and LS estimation are equivalent. The log-likelihood function for a model $\eta(\cdot)$ with centered additive Gaussian errors $\mathcal{N}(0, \boldsymbol{\Sigma})$ is:

$$\ell(\boldsymbol{\theta}; \mathbf{y}) = -\frac{1}{2}(\mathbf{y} - \boldsymbol{\eta}(\boldsymbol{\theta}))^T \boldsymbol{\Sigma}^{-1}(\mathbf{y} - \boldsymbol{\eta}(\boldsymbol{\theta})) + \text{constant}, \quad (\text{A.9})$$

where \mathbf{y} is the vector of observations, and $\boldsymbol{\Sigma}$ is the covariance matrix of the errors. The EFIM can be computed under the closed form:

$$\mathbf{i}(\hat{\boldsymbol{\theta}}) = \mathbf{J}^T \boldsymbol{\Sigma}^{-1} \mathbf{J}. \quad (\text{A.10})$$

Therefore, the inverse of expected Fisher $\mathbf{i}^{-1}(\hat{\boldsymbol{\theta}})$ information provides the same estimation of precision for the parameter estimates as the variance-covariance matrix derived from the LS estimator as shown in Equation A.8.

2 Equivalence between the EFIM Wald test and the variance-covariance propagation under Gaussian errors

Consider the inference of a parameter $\boldsymbol{\theta} = (\psi, \boldsymbol{\omega})$ and the following partitioning of \mathbf{i}

$$\mathbf{i}(\boldsymbol{\theta}) = \begin{pmatrix} \mathbf{i}_{\psi\psi}(\boldsymbol{\theta}) & \mathbf{i}_{\psi\boldsymbol{\omega}}(\boldsymbol{\theta}) \\ \mathbf{i}_{\boldsymbol{\omega}\psi}(\boldsymbol{\theta}) & \mathbf{i}_{\boldsymbol{\omega}\boldsymbol{\omega}}(\boldsymbol{\theta}) \end{pmatrix} \quad (\text{A.11})$$

According to [126] section 4.6, the estimator $\hat{\psi}$ is asymptotically unbiased with variance:

$$i_p(\hat{\psi})^{-1} = \left(\mathbf{i}_{\psi\psi}(\hat{\boldsymbol{\theta}}) - \mathbf{i}_{\psi\boldsymbol{\omega}}(\hat{\boldsymbol{\theta}}) \mathbf{i}_{\boldsymbol{\omega}\boldsymbol{\omega}}(\hat{\boldsymbol{\theta}})^{-1} \mathbf{i}_{\boldsymbol{\omega}\psi}(\hat{\boldsymbol{\theta}}) \right)^{-1} \quad (\text{A.12})$$

$i_p(\hat{\psi})$ is the "partial" expected information of ψ which is simply the diagonal value of $\mathbf{i}(\hat{\boldsymbol{\theta}})^{-1}$ at the block ψ . Equation A.10 proves that $i_p(\hat{\psi})^{-1}$ is also the diagonal value of the variance-covariance matrix as defined in Equation 2.3 under additive centered Gaussian errors. Furthermore, it can be shown that :

$$i_p(\hat{\psi}) = \mathbb{E} \left[- \frac{\partial^2 \ell_p(\hat{\psi}; \mathbf{y})}{\partial \psi^2} \right] \quad (\text{A.13})$$

where $\ell_p(\psi) = \ell(\psi, \hat{\boldsymbol{\omega}}_\psi)$ is the profile likelihood and $-\frac{\partial^2 \ell_p(\hat{\psi}; \mathbf{y})}{\partial \psi^2}$ is the observed information for ψ . This establishes the equivalence between classical variance-covariance inference and the Wald test $i_p(\hat{\psi})^{-1/2}(\hat{\psi} - \psi)$ for evaluating confidence intervals of ψ .

3 Derivation of the profile adjustment

Let's consider a general smooth model f that can represent \mathbf{R}_{rs}^+ . From the score equation 4.13, we can write:

$$\ell_{\omega}(\boldsymbol{\theta}) = \left(\frac{\partial f(\boldsymbol{\theta})}{\partial \boldsymbol{\omega}} \right)^T \Sigma^{-1}(\mathbf{y} - f(\boldsymbol{\theta}))$$

Expanding the product $\ell_{\omega}(\boldsymbol{\theta}_1)\ell_{\omega}(\boldsymbol{\theta}_2)^T$:

$$\left(\frac{\partial f(\boldsymbol{\theta}_1)}{\partial \boldsymbol{\omega}} \right)^T \Sigma^{-1}(\mathbf{y} - f(\boldsymbol{\theta}_1))(\mathbf{y} - f(\boldsymbol{\theta}_2))^T \Sigma^{-1} \left(\frac{\partial f(\boldsymbol{\theta}_2)}{\partial \boldsymbol{\omega}} \right)$$

when $\boldsymbol{\theta}_1 = \boldsymbol{\theta}_2$, the expected value of the core term can be simplified to:

$$\mathbb{E}[(\mathbf{y} - f(\boldsymbol{\theta}_1))(\mathbf{y} - f(\boldsymbol{\theta}_2))^T] = \Sigma$$

Consequently, the expected value of the product of score functions simplifies to:

$$\mathbb{E}[\ell_{\omega}(\boldsymbol{\theta})\ell_{\omega}(\boldsymbol{\theta})^T] = \left(\frac{\partial f(\boldsymbol{\theta})}{\partial \boldsymbol{\omega}} \right)^T \Sigma^{-1} \left(\frac{\partial f(\boldsymbol{\theta})}{\partial \boldsymbol{\omega}} \right)$$

Appendix B

Here, we elaborate on the equations used to model the IOPs of the water, specifically the absorption \mathbf{a} and backscattering \mathbf{b}_b coefficients.

1 Absorption

We consider the IOPs of the water, specifically for modeling the absorption \mathbf{a} and backscattering \mathbf{b}_b coefficients. In coastal waters, light is absorbed notably by water itself \mathbf{a}_w , phytoplankton \mathbf{a}_ϕ , Colored Dissolved Organic Matter (CDOM) \mathbf{a}_{cdom} and the absorption \mathbf{a}_{nap} due to suspended inorganic matter. These absorption contributions are modeled as follows (units in m^{-1}):

$$\mathbf{a}_\phi(\text{Chl}, \lambda) = \gamma_\phi(\lambda) \cdot \text{Chl}^{\nu_\phi(\lambda)} \quad (\text{B.1})$$

$$\mathbf{a}_{\text{cdom}}(\text{CDOM}, \lambda) = \text{CDOM} \cdot \exp(-\beta_{\text{cdom}} \cdot (\lambda - 443)) \quad (\text{B.2})$$

$$\mathbf{a}_{\text{nap}}(\text{TSM}, \lambda) = \text{TSM} \cdot \gamma_{\text{nap}} \cdot \exp(-\beta_{\text{nap}} \cdot (\lambda - 443)) \quad (\text{B.3})$$

\mathbf{a}_w is provided in [127], \mathbf{a}_ϕ is modeled with the empirical spectra $\gamma_\phi(\lambda)$, $\nu_\phi(\lambda)$ derived from [128] whereas the empirical values β_{cdom} , γ_{nap} and β_{nap} are set to .0176, 0.036, 0.0123 respectively, as average values for coastal waters as proposed in [129].

2 Backscattering

Contributions to the backscattering \mathbf{b}_b originate mainly from water \mathbf{b}_w and suspended particulate matter \mathbf{b}_p .

$$\mathbf{b}_b = \mathbf{b}_w + \mathbf{b}_p \quad (\text{B.4})$$

$$\mathbf{b}_p(\text{TSM}, \lambda) = \text{TSM} \cdot \gamma_{bp} \cdot \left(\frac{\lambda}{555.0} \right)^{-\nu_{bp}}, \quad (\text{B.5})$$

$$\mathbf{b}_w(\lambda) = \gamma_{bw} \cdot \left(\frac{\lambda}{500.0} \right)^{\nu_{bw}}. \quad (\text{B.6})$$

The spectral power coefficient for suspended particulate matter backscattering ν_{bp} varies globally and seasonally within the range 0.5,4.5 depending on the empirical algorithm [130]. We set these empirical values at $\gamma_{bp} = 0.0077$, $\nu_{bp} = -0.2$ from [14].

For water backscattering, values were fixed at $\gamma_{bw} = 0.0035$, $\nu_{bw} = -4.32$ from [131].

The water column IOP's parameter is then $\omega_c = (\text{Chl}, \text{CDOM}, \text{TSM})$, where Chl is in mg m^{-3} , CDOM in m^{-1} , and the Total Suspended Matter TSM in g m^{-3} .

3 Academic achievements

Table B.1 – List of achievements

Event	Title	Author(s) and Affiliations
Conference Paper: Whispers <i>08 February 2021</i>	Likelihood ratio statistic for inferring the uncertainty of satellite derived bathymetry.	Sicot G. ¹ , GHANNAMI M.A. ¹ , Lennon M. ² , LOYER S. ³ , Thomas N. ²
Conference Paper: Whispers <i>2021</i>	Estimability study of the parameters of the semi-analytical lee model with hyperspectral data.	Sicot G. ² , GHANNAMI M.A. ^{1,2} , Lennon M. ² , Loyer S. ³ , Thomas N. ²
Conference Paper: Whispers <i>2021</i>	A Method for propagating uncertainties of the top of atmosphere sentinel-2 measurements to bottom of atmosphere reflectance for aquatic applications.	Thomas N. ² , Lennon M. ² , Danilo C., Sicot G. ² , Ghannami M.A. ^{1,2} , Loyer S. ³
CHC22 <i>08 June 2022</i>	Combining radiometric and geometric information in spectral imagery for improving water column estimation in shallow waters.	GHANNAMI M.A. ^{1,2} , Daniel S. ¹ , Sicot G. ² , Quidu I. ²
Speed Mapping Challenge <i>09 June 2022</i>	2nd place award/Team Cross	Abair S. ⁴ , Noman J. ¹ , GHANNAMI M.A. ^{1,2} , Cassol W.N. ¹
LabSTICC M3 Seminar <i>23 March 2023</i>	Statistical inference of water column depth obtained by radiometric and geometric analysis of spectral imagery.	GHANNAMI M.A. ^{1,2} , Daniel S. ¹ , Quidu I. ² , Sicot G. ²
Assises de la Mer 2022 <i>03 June 2022</i>	Statistical inference of water column depth obtained by radiometric and geometric analysis of spectral imagery.	GHANNAMI M.A. ^{1,2} , Daniel S. ¹ , Quidu I. ² , Sicot G. ²
CHC24 <i>27 May 2024</i>	Uncertainty assessment of water depth estimation based on triangulation method using a pushbroom sensor.	GHANNAMI M.A. ^{1,2} , Daniel S. ¹ , Sicot G. ² , Quidu I. ²
Review Article <i>2024</i>	A Likelihood-based triangulation method for uncertainties in through-water depth mapping. <i>Remote Sens.</i> 2024, 16	GHANNAMI M.A. ^{1,2} , Daniel S. ¹ , Sicot G. ² , Quidu I. ²
Review Article <i>Submission scheduled for January 2024</i>	Likelihood based inference for bathymetric uncertainties in semi-analytical models. <i>IEEE TGRS</i>	GHANNAMI M.A. ^{1,2} , Daniel S. ¹ , Sicot G. ² , Quidu I. ²

¹Université Laval, Département des sciences géomatiques, Québec, Canada.

²ENSTA Bretagne, M3 Team - Lab-STICC, UMR-CNRS 6285, Brest, France. ³Shom, Brest, France. ⁴INRS, Québec, Canada.

Bibliography

- [1] M.L. Martínez, A. Intralawan, G. Vázquez, O. Pérez-Maqueo, P. Sutton, and R. Landgrave. The coasts of our world: Ecological, economic and social importance. *Ecological Economics*, 63(2):254–272, 2007. ISSN 0921-8009. doi: <https://doi.org/10.1016/j.ecolecon.2006.10.022>. URL <https://www.sciencedirect.com/science/article/pii/S0921800906005465>. Ecological Economics of Coastal Disasters.
- [2] Davide Pasquali and Alessandro Marucci. The effects of urban and economic development on coastal zone management. *Sustainability (Switzerland)*, 13, 6 2021. ISSN 20711050. doi: 10.3390/su13116071.
- [3] G. Singh, R. Cottrell, T. Eddy, and A. Cisneros-Montemayor. Governing the land-sea interface to achieve sustainable coastal development. *Frontiers in Marine Science*, 2021. doi: 10.3389/fmars.2021.709947. URL <https://www.frontiersin.org/articles/10.3389/fmars.2021.709947/pdf>.
- [4] Shridhar Jawak, Shekhar Vadlamani, and Alvarinho Luis. A synoptic review on deriving bathymetry information using remote sensing technologies: Models, methods and comparisons. *Advances in Remote Sensing*, 4:147–162, 06 2015. doi: 10.4236/ars.2015.42013.
- [5] Mohammad Ashphaq, Pankaj K. Srivastava, and D. Mitra. Review of near-shore satellite derived bathymetry: Classification and account of five decades of coastal bathymetry research. *Journal of Ocean Engineering and Science*, 6:340–359, 12 2021. ISSN 24680133. doi: 10.1016/j.joes.2021.02.006.
- [6] David Lyzenga. Passive remote sensing techniques for mapping water depth and bottom features. *Applied Optics*, 379, 02 1978.
- [7] B. Lubac, Olivier Burvingt, A. N. Lerma, and N. Sénéchal. Performance and uncertainty of satellite-derived bathymetry empirical approaches in an energetic coastal environment. *Remote Sensing*, 14(10):2350, 2022. doi: 10.3390/rs14102350. URL <https://www.mdpi.com/2072-4292/14/10/2350/pdf?version=1652360089>.

- [8] Rodrigo Alejandro Garcia. *Uncertainty in Hyperspectral Remote Sensing: Analysis of the Potential and Limitation of Shallow Water Bathymetry and Benthic Classification*. PhD thesis, Curtin University, Podunk IN, 2015.
- [9] Thierry Toutin. Geometric processing of remote sensing images: Models, algorithms ,methods. *International Journal of Remote Sensing*, 25:1893–1924, 5 2004. ISSN 01431161. doi: 10.1080/0143116031000101611.
- [10] R. K. Slocum, W. Wright, C. Parrish, B. Costa, M. Sharr, and T. A. Battista. Guidelines for bathymetric mapping and orthosubsectionimage generation using suas and sfm, an approach for conducting nearshore coastal mapping. NOAA technical memorandum NOS NCCOS 265, United States, National Ocean Service; National Centers for Coastal Ocean Science (U.S.); United States, National Oceanic and Atmospheric Administration; Coral Reef Conservation Program (U.S.), 2019. URL <https://doi.org/10.25923/07mx-1f93>.
- [11] Brian Calder and David Wells. Cube user’s manual, 2007.
- [12] International Hydrographic Organization. International hydrographic organization standards for hydrographic surveys s-44 edition 6.0.0, 2020. URL https://iho.int/uploads/user/pubs/standards/s-44/S-44_Edition_6.1.0.pdf.
- [13] Kai Zhang, Xin Wang, Ziyin Wu, Fanlin Yang, Hongchun Zhu, Dineng Zhao, and Jinshan Zhu. Improving statistical uncertainty estimate of satellite-derived bathymetry by accounting for depth-dependent uncertainty. *IEEE Transactions on Geoscience and Remote Sensing*, 60:1–9, 2022. doi: 10.1109/TGRS.2021.3069868.
- [14] Zhongping Lee, Kendall L. Carder, Curtis D. Mobley, Robert G. Steward, and Jennifer S. Patch. Hyperspectral remote sensing for shallow waters: 2. deriving bottom depths and water properties by optimization. *Applied Optics*, 38(18):3831–3843, 1999.
- [15] Sylvain Jay, Mireille Guillaume, Malik Chami, Yannick Deville Audrey Minghelli, Bruno Lafrance, and Véronique Serfaty. Predicting minimum uncertainties in the inversion of ocean color geophysical parameters based on cramer-rao bounds. *OPTICS EXPRESS*, 26, 01 2018.
- [16] A.R. HUETE. Remote sensing for environmental monitoring. In Janick F. Artola, Ian L. Pepper, and Mark L. Brusseau, editors, *Environmental Monitoring and Characterization*, pages 183–206. Academic Press, Burlington, 2004. ISBN 978-0-12-064477-3. doi: <https://doi.org/10.1016/B978-012064477-3/50013-8>. URL <https://www.sciencedirect.com/science/article/pii/B9780120644773500138>.

- [17] Alessandro Benelli, Chiara Cevoli, and Angelo Fabbri. In-field hyperspectral imaging: An overview on the ground-based applications in agriculture. *Journal of Agricultural Engineering*, 51:129–139, 09 2020. doi: 10.4081/jae.2020.1030.
- [18] Karen E. Joyce, Kate C. Fickas, and Michelle Kalamandeen. The unique value proposition for using drones to map coastal ecosystems. *Cambridge Prisms: Coastal Futures*, 1:e6, 2023. doi: 10.1017/cft.2022.7.
- [19] P. Agrafiotis and A. Georgopoulos. Camera constant in the case of two media photogrammetry. *The International Archives of the Photogrammetry, Remote Sensing and Spatial Information Sciences*, XL-5/W5:1–6, 2015. doi: 10.5194/isprsarchives-XL-5-W5-1-2015. URL <https://isprs-archives.copernicus.org/articles/XL-5-W5/1/2015/>.
- [20] Margaret Kalacska, Oliver Lucanus, Leandro Sousa, Thiago Vieira, and Juan Pablo Arroyo-Mora. Freshwater fish habitat complexity mapping using above and underwater structure-from-motion photogrammetry. *Remote Sensing*, 10(12), 2018. ISSN 2072-4292. doi: 10.3390/rs10121912.
- [21] Lei Hao Jia Guorui, Zhao Huijie. Uncertainty propagation algorithm from the radiometric calibration to the restored earth observation radiance. *Optics Express*, 22:9442, 4 2014. ISSN 1094-4087. doi: 10.1364/oe.22.009442.
- [22] Susan Barbara Kay. *Radiative transfer modeling for sun glint correction in marine satellite imagery*. Doctoral dissertation, University of Exeter, 12 2011.
- [23] P. Agrafiotis, D. Skarlatos, T. Forbes, C. Poullis, M. Skamantzari, and A. Georgopoulos. Underwater photogrammetry in very shallow waters: Main challenges and caustics effect removal. *The International Archives of the Photogrammetry, Remote Sensing and Spatial Information Sciences*, XLII-2:15–22, 2018. doi: 10.5194/isprs-archives-XLII-2-15-2018. URL <https://isprs-archives.copernicus.org/articles/XLII-2/15/2018/>.
- [24] Richard Stumpf, Kristine Holderied, and Mark Sinclair. Determination of water depth with high-resolution satellite imagery over variable bottom types. *Limnology and Oceanography*, 48:547,557, 2003.
- [25] Ankita Misra, Zoran Vojinovic, Balaji Ramakrishnan, Arjen Luijendijk, and Roshanka Ranasinghe. Shallow water bathymetry mapping using support vector machine (svm) technique and multispectral imagery. *International Journal of Remote Sensing*, 39:1–20, 01 2018. doi: 10.1080/01431161.2017.1421796.
- [26] Vanesa Mateo-Pérez, Marina Corral-Bobadilla, Francisco Ortega-Fernández, and Eliseo P. Vergara-González. Port bathymetry mapping using support vector machine

- technique and sentinel-2 satellite imagery. *Remote Sensing*, 12(13), 2020. ISSN 2072-4292. doi: 10.3390/rs12132069. URL <https://www.mdpi.com/2072-4292/12/13/2069>.
- [27] Noha Kamal and Nagwa El-Ashmawy. Potential of using machine learning regression techniques to utilize sentinel images for bathymetry mapping of Nile river. *The Egyptian Journal of Remote Sensing and Space Sciences*, 26(3):545–555, 2023. ISSN 1110-9823. doi: <https://doi.org/10.1016/j.ejrs.2023.06.004>. URL <https://www.sciencedirect.com/science/article/pii/S1110982323000431>.
- [28] Amin Jalilzadeh and Saeed Behzadi. Machine learning method for predicting the depth of shallow lakes using multi-band remote sensing images. *Journal of Soft Computing in Civil Engineering*, 3(2):54–64, 2019. ISSN 2588-2872. doi: 10.22115/scce.2019.196533.1119. URL https://www.jssoftcivil.com/article_95794.html.
- [29] Mahmoud Al Najar, Rachid Benshila, Youssra El Bennioui, Grégoire Thoumyre, Rafael Almar, Erwin W. J. Bergsma, Jean-Marc Delvit, and Dennis G. Wilson. Coastal bathymetry estimation from sentinel-2 satellite imagery: Comparing deep learning and physics-based approaches. *Remote Sensing*, 14(5), 2022. ISSN 2072-4292. doi: 10.3390/rs14051196. URL <https://www.mdpi.com/2072-4292/14/5/1196>.
- [30] Curtis Mobley, Lydia Sundman, Curtiss Davis, Jeffrey Bowles, Trijntje Downes, Robert Leathers, Marcos Montes, W. Bissett, David Kohler, R. Reid, Eric Louchard, and Arthur Gleason. Interpretation of hyperspectral remote-sensing imagery by spectrum matching and look-up tables. *Applied Optics*, 44:3576–92, 07 2005. doi: 10.1364/AO.44.003576.
- [31] Phinn S Hedley J, Roelfsema C. Efficient radiative transfer model inversion for remote sensing applications. *Remote Sensing of Environment*, 113:2527–2532, 07 2009.
- [32] Thomas Petit, T. Bajjouk, P. Mouquet, S. Rochette, B. Vozel, and Christophe Delacourt. Hyperspectral remote sensing of coral reefs by semi-analytical model inversion – Comparison of different inversion setups. *Remote Sensing of Environment*, 190:348–365, 2017. doi: 10.1016/j.rse.2017.01.004. URL <https://univ-rennes.hal.science/hal-01484526>.
- [33] James J. Butler, Steven W. Brown, Robert D. Saunders, B. Carol Johnson, Stuart F. Biggar, Edward F. Zalewski, Brian L. Markham, Paul N. Gracey, James B. Young, and Robert A. Barnes. Radiometric measurement comparison on the integrating sphere source used to calibrate the moderate resolution imaging spectro-radiometer (modis), the landsat 7 enhanced thematic mapper plus (etm+). *Journal of Research of the National Institute of Standards ,Technology*, 108(3), 2003.
- [34] Karim Lenhard. Improving the calibration of airborne hyperspectral sensors for earth observation, 2015.

- [35] Peter Gege, Jochen Fries, Peter Haschberger, Paul Schötz, Horst Schwarzer, Peter Strobl, Birgit Suhr, Gerd Ulbrich, and Willem Jan Vreeling. Calibration facility for airborne imaging spectrometers. *ISPRS Journal of Photogrammetry ,Remote Sensing*, 64:387–397, 7 2009. ISSN 09242716. doi: 10.1016/j.isprsjprs.2009.01.006.
- [36] Cheonggil Jin, Hoyong Ahn, Doochun Seo, and Chuluong Choi. Radiometric calibration and uncertainty analysis of kompsat-3a using the reflectance-based method. *Sensors*, 20(9), 2020. ISSN 1424-8220. doi: 10.3390/s20092564. URL <https://www.mdpi.com/1424-8220/20/9/2564>.
- [37] Aurelie M. Poncet, Thorsten Knappenberger, Christian Brodbeck, Michael Fogle, Joey N. Shaw, and Brenda V. Ortiz. Multispectral uas data accuracy for different radiometric calibration methods. *Remote Sensing*, 11, 2019. ISSN 20724292. doi: 10.3390/rs11161917.
- [38] Yahui Guo, J. Senthilnath, Wenxiang Wu, Xueqin Zhang, Zhaoqi Zeng, and Han Huang. Radiometric calibration for multispectral camera of different imaging conditions mounted on a uav platform. *Sustainability*, 11(4), 2019. ISSN 2071-1050. doi: 10.3390/su11040978. URL <https://www.mdpi.com/2071-1050/11/4/978>.
- [39] Olivier Burggraaff, Norbert Schmidt, Jaime Zamorano, Klaas Pauly, Sergio Pascual, Carlos Tapia, Evangelos Spyarakos, and Frans Snik. Standardized spectral and radiometric calibration of consumer cameras. *Opt. Express*, 27(14):19075–19101, 07 2019. doi: 10.1364/OE.27.019075. URL <https://opg.optica.org/oe/abstract.cfm?URI=oe-27-14-19075>.
- [40] W Barnes X Xiong. An overview of modis radiometric calibration, characterisation. *Advances in Atmospheric Sciences*, 23:69–79, 1 2006.
- [41] F. Mélin, G. Sclep, T. Jackson, and S. Sathyendranath. Sentinel-2 calibration, validation plan for the operational phase, 12 2014. URL www.esa.int.
- [42] K Thorne, B Markharn, P Slater Barker, and SJPE Biggar. Radiometric calibration of landsat. *Photogrammetric Engineering & Remote Sensing*, 63(7):853–858, 1997.
- [43] Howard R. Gordon. Atmospheric correction of ocean color imagery in the earth observing system era. *Journal of Geophysical Research*, 102(D14):17,081–17,106, 1997.
- [44] Bo-Cai Gao, Marcos J. Montes, Curtiss O. Davis, and Alexander F.H. Goetz. Atmospheric correction algorithms for hyperspectral remote sensing data of land and ocean. *Remote Sensing of Environment*, 113:S17–S24, 2009. ISSN 0034-4257.
- [45] Curtis D Mobley, Jeremy Werdell, Bryan Franz, Ziauddin Ahmad, and Sean Bailey. Atmospheric correction for satellite ocean color radiometry: A tutorial and documentation of the algorithms used by the nasa ocean biology processing group, 2016.

- [46] Karl Rinner. Problems of two-medium photogrammetry. *Photogrammetric Engineering*, pages 275–282, 3 1948. Presented at the Annual Convention of the American Society of Photogrammetry, Washington, D. C.
- [47] Toshimi Murase, Miho Tanaka, Tomomi Tani, Yuko Miyashita, Naoto Ohkawa, Satoshi Ishiguro, Yasuhiro Suzuki, Hajime Kayanne, and Hiroya Yamano. A photogrammetric correction procedure for light refraction effects at a two-medium boundary. *Photogrammetric Engineering and Remote Sensing*, 74:1129–1136, 09 2008. doi: 10.14358/PERS.74.9.1129.
- [48] Matus Hodul, Stephen Bird, Anders Jensen Knudby, and René Chénier. Satellite derived photogrammetric bathymetry. *ISPRS Journal of Photogrammetry and Remote Sensing*, 2018.
- [49] Justin Butler Stuart Lane, Jim H Chandler, and Ekaterini Porfiri. Through-water close range digital photogrammetry in flume and field environments. *Photogrammetric Record*, 17:419–439, 2002.
- [50] G. Zhou, X. Li, T. Yue, W. Huang, C. He, and Y. Huang. Solving the rational polynomial coefficients based on l curve. *The International Archives of the Photogrammetry, Remote Sensing and Spatial Information Sciences*, XLII-3:2511–2515, 2018. doi: 10.5194/isprs-archives-XLII-3-2511-2018.
- [51] Robin Rofallski and Thomas Luhmann. An efficient solution to ray tracing problems in multimedia photogrammetry for flat refractive interfaces. *Journal of Photogrammetry Remote Sensing and Geoinformation Science*, 90, 03 2022. doi: 10.1007/s41064-022-00192-1.
- [52] Chendi Zhang, Aoran Sun, Marwan A. Hassan, and Chao Qin. Assessing through-water structure-from-motion photogrammetry in gravel-bed rivers under controlled conditions. *Remote Sensing*, 14(21), 2022. ISSN 2072-4292. doi: 10.3390/rs14215351.
- [53] Danny Sims-Waterhouse, Mohammed Isa, Samanta Piano, and Richard Leach. Uncertainty model for a traceable stereo-photogrammetry system. *Precision Engineering*, 63: 1–9, 5 2020. ISSN 01416359. doi: 10.1016/j.precisioneng.2019.12.008.
- [54] Bincai Cao, Yong Fang, Zhengzhi Jiang, Li Gao, and Haiyan Hu. Shallow water bathymetry from worldview-2 stereo imagery using two-media photogrammetry. *European Journal of Remote Sensing*, 52:506–521, 1 2019. ISSN 22797254. doi: 10.1080/22797254.2019.1658542.
- [55] Bin Cao, Ruru Deng, and Shulong Zhu. Universal algorithm for water depth refraction correction in through-water stereo remote sensing. *International Journal of Applied*

- Earth Observation and Geoinformation*, 91:102108, 9 2020. ISSN 03032434. doi: 10.1016/j.jag.2020.102108.
- [56] Yu Zhou, Lejun Lu, Linlin Li, Qiong Zhang, and Peizhen Zhang. A generic method to derive coastal bathymetry from satellite photogrammetry for tsunami hazard assessment. *Geophysical Research Letters*, 48(21):e95142, November 2021. doi: 10.1029/2021GL095142.
- [57] Dimitrios Skarlatos and Panagiotis Agrafiotis. A novel iterative water refraction correction algorithm for use in structure from motion photogrammetric pipeline. *Journal of Marine Science and Engineering*, 6, 7 2018. ISSN 20771312. doi: 10.3390/jmse6030077.
- [58] G. C. Tewinkel. Water depths from aerial photographs. *Photogrammetric Engineering*, pages 1038–1042, 3 1963. Paper presented at the 29th Annual Meeting of the American Society of Photogrammetry, Washington, D. C.
- [59] Jie Shan. Relative orientation for two-media photogrammetry. *Photogrammetric Record*, 14(84):993–999, 10 1994.
- [60] Christian Mulsow. A flexible multi-media bundle approach. In *International Archives of Photogrammetry, Remote Sensing and Spatial Information Sciences*, volume XXXVIII, 2010.
- [61] Rudiger Kotowski. Phototriangulation in multi-media photogrammetry. In *International Archives of Photogrammetry and Remote Sensing*, volume XXVII, pages 324–334, 2010.
- [62] A. Okamoto. Wave influences in two-media photogrammetry. *Photogrammetric Engineering and Remote Sensing*, 48(9):1487–1499, 9 1982.
- [63] Marina Alterman, Yoav Y Schechner, and Yohay Swirski. Triangulation in random refractive distortions. *IEEE Transactions on Pattern Analysis and Machine Intelligence*, 39(3):603–616, 3 2017. doi: 10.1109/TPAMI.2016.2551740.
- [64] O. Barndorff-Nielsen and D. Cox. Asymptotic techniques for use in statistics. *Mathematics*, 1989. doi: 10.2307/2348202.
- [65] Thomas A. Severini. An empirical adjustment to the likelihood ratio statistic. *Biometrika*, 86(2):235–247, 06 1999.
- [66] Alessandra R. Brazzale and Anthony C. Davison. Accurate parametric inference for small samples. *Statistical Science*, 23(4):465–484, 2008. ISSN 08834237. URL <http://www.jstor.org/stable/20697653>.
- [67] P Driscoll, F Lecky, and M Crosby. An introduction to statistical inference. *Emergency Medicine Journal*, 17(5):357–363, 2000. ISSN 1351-0622. doi: 10.1136/emj.17.5.357. URL <https://emj.bmj.com/content/17/5/357>.

- [68] Julius Sim and Norma Reid. Statistical inference by confidence intervals: Issues of interpretation and utilization. *Physical Therapy*, 79(2):186–195, 02 1999. ISSN 0031-9023. doi: 10.1093/ptj/79.2.186. URL <https://doi.org/10.1093/ptj/79.2.186>.
- [69] B. Efron. Bootstrap methods: Another look at the jackknife. *The Annals of Statistics*, 7(1):1–26, 1979. ISSN 00905364. URL <http://www.jstor.org/stable/2958830>.
- [70] JCGM. Evaluation of measurement data-guide to the expression of uncertainty in measurement Évaluation des données de mesure-guide pour l’expression de l’incertitude de mesure, 2008. URL www.bipm.org.
- [71] Harald Cramér. *Mathematical Methods of Statistics*. Princeton University Press, Princeton, NJ, 1946. ISBN 0-691-08004-6.
- [72] Calyampudi Radakrishna Rao. Information and the accuracy attainable in the estimation of statistical parameters. *Bulletin of the Calcutta Mathematical Society*, 37:81–89, 1945.
- [73] Bradley Efron and David V. Hinkley. Assessing the accuracy of the maximum likelihood estimator: Observed versus expected fisher information. *Biometrika*, 65(3):457–482, 1978. ISSN 00063444. URL <http://www.jstor.org/stable/2335893>.
- [74] L. Steven M. Kay. *Fundamentals of Statistical Signal Processing: Estimation Theory*. Prentice Hall Signal Processing Series, 1993.
- [75] Bradley Efron. Uncertainty analysis for non-identifiable dynamical systems: Profile likelihoods, bootstrapping and more. *Conference on Computational Methods in Systems Biology*, 2014. URL <https://dblp.org/rec/conf/cmsb/FrohlichTH14>.
- [76] Matthew J. Simpson, Ruth E. Baker, Sean T. Vittadello, and Oliver J. Maclaren. Practical parameter identifiability for spatio-temporal models of cell invasion. *Journal of the Royal Society Interface*, 17(164):20200055, 2020. doi: 10.1098/rsif.2020.0055.
- [77] Rua Murray Nicholas N. Lam, Paul D. Docherty. Practical identifiability of parametrised models: A review of benefits and limitations of various approaches. *Mathematics and Computers in Simulation*, 199:202–216, 09 2022.
- [78] A. Raue, C. Kreutz, T. Maiwald, J. Bachmann, M. Schilling, U. Klingmüller, and J. Timmer. Structural and practical identifiability analysis of partially observed dynamical models by exploiting the profile likelihood. *Bioinformatics*, 25:1923–1929, 08 2009. doi: 10.1093/bioinformatics/btp358.
- [79] A. R. Brazzale, A. C. Davison, and N. Reid. *Applied Asymptotics: Case Studies in Small-Sample Statistics*. Cambridge University Press, Cambridge, 2007. URL <http://infoscience.epfl.ch/record/104219>.

- [80] Ib M. Skovgaard. Likelihood asymptotics. *Scandinavian Journal of Statistics*, 28(1): 3–32, 2001. doi: <https://doi.org/10.1111/1467-9469.00223>.
- [81] A. S. Tocquet. Likelihood based inference in non-linear regression models using the p^* and r^* approach. *Scandinavian Journal of Statistics*, 28(3):429–443, 2001. URL <https://www.jstor.org/stable/4616670>.
- [82] Donald Pierce and Ruggero Bellio. Modern likelihood-frequentist inference. *International Statistical Review*, 85, 08 2017. doi: 10.1111/insr.12232.
- [83] Luigi Pace and Alessandra Salvan. Adjustments of the profile likelihood from a new perspective. *Journal of Statistical Planning and Inference*, 10(10):3554–3564, 2006. doi: 10.1016/j.jspi.2004.11.016.
- [84] Thomas A. Severini. Modified estimating functions. *Biometrika*, 89(2):333–343, 2002. URL <https://www.jstor.org/stable/4140580>.
- [85] Xumeng Cao and James C. Spall. Relative performance of expected and observed fisher information in covariance estimation for maximum likelihood estimates. In *American Control Conference (ACC)*, pages 1871–1876, 2012. doi: 10.1109/ACC.2012.6315584.
- [86] G. Maldonado and S. Greenland. A comparison of the performance of model-based confidence intervals when the correct model form is unknown: coverage of asymptotic means. *Epidemiology*, 5(2):171–182, 1994. doi: 10.1097/00001648-199403000-00007.
- [87] Xiangyu Yuan and James C. Spall. Confidence intervals with expected and observed fisher information in the scalar case. In *2020 American Control Conference (ACC)*, pages 2599–2604, 2020. doi: 10.23919/ACC45564.2020.9147324.
- [88] Bruce G. Lindsay and Bing Li. On second-order optimality of the observed Fisher information. *The Annals of Statistics*, 25(5):2172 – 2199, 1997. doi: 10.1214/aos/1069362393. URL <https://doi.org/10.1214/aos/1069362393>.
- [89] Alessandra R. Brazzale and Valentina Mamei. Likelihood Asymptotics in Nonregular Settings: A Review with Emphasis on the Likelihood Ratio. *Statistical Science*, 39(2):322 – 345, 2024. doi: 10.1214/23-STS910. URL <https://doi.org/10.1214/23-STS910>.
- [90] P. Stoica and T.L. Marzetta. Parameter estimation problems with singular information matrices. *IEEE Transactions on Signal Processing*, 49(1):87–90, 2001. doi: 10.1109/78.890346.
- [91] Yen-Huan Li and Ping-Cheng Yeh. An interpretation of the moore-penrose generalized inverse of a singular fisher information matrix. *IEEE Transactions on Signal Processing*,

- 60(10):5532–5536, October 2012. ISSN 1941-0476. doi: 10.1109/tsp.2012.2208105. URL <http://dx.doi.org/10.1109/TSP.2012.2208105>.
- [92] Mohamed Ali Ghannami, Sylvie Daniel, Guillaume Sicot, and Iabelle Quidu. A likelihood-based triangulation method for uncertainties in through water depth mapping. *ISPRS Journal of Photogrammetry and Remote Sensing*, 06 2023. Submitted and currently under revision.
- [93] John T Dolloff. Rpc uncertainty parameters: Generation, application, and effects. In *Proceedings of the ASPRS Annual Convention*, pages 19–23, 2012.
- [94] Ali Coskun Kiraci and Gonul Toz. Theoretical analysis of positional uncertainty in direct georeferencing. *The International Archives of the Photogrammetry, Remote Sensing and Spatial Information Sciences*, XLI-B1:1221–1226, 10 2016. ISSN 1682-1750. doi: 10.5194/isprs-archives-xli-b1-1221-2016.
- [95] Craig Rodarmel, Mark Lee, John Gilbert, Ben Wilkinson, Henry Theiss, John Dolloff, and Christopher O’Neill. The universal lidar error model (approved for public release: 15-144). *Photogrammetric Engineering Remote Sensing*, 81(7):543–556, 2015. ISSN 0099-1112. doi: <https://doi.org/10.14358/PERS.81.7.543>. URL <https://www.sciencedirect.com/science/article/pii/S0099111215301713>.
- [96] Seyed-Mahdi Nasiri, Reshad Hosseini, and Hadi Moradi. The optimal triangulation method is not really optimal. *IET Image Processing*, 17(10):2855–2865, 2023.
- [97] Malcolm D. Shuster. A survey of attitude representations. *Journal of the Astronautical Sciences*, 41(4):439–517, 1993.
- [98] Christopher Bingham. An antipodally symmetric distribution on the sphere. *The Annals of Statistics*, 2(6):1201–1225, 1974.
- [99] Mohamed Ali Ghannami, Guillaume Sicot, Marc Lennon, Sohpie Loyer, and Nicolas Thomas. Likelihood ratio statistic for inferring the uncertainty of satellite derived bathymetry. In *2021 11th Workshop on Hyperspectral Imaging and Signal Processing: Evolution in Remote Sensing (WHISPERS)*, 03 2021.
- [100] Zhongping Lee Chuanmin Hu, Lian Feng. Uncertainties of seawifs, modis remote sensing reflectance: Implications from clear water measurements. *Remote Sensing of Environment*, 133:168–182, 6 2013. ISSN 00344257. doi: 10.1016/j.rse.2013.02.012.
- [101] F. Mélin, G. Sclep, T. Jackson, and S. Sathyendranath. Uncertainty estimates of remote sensing reflectance derived from comparison of ocean color satellite data sets. *Remote Sensing of Environment*, 177:107–124, 2016. ISSN 0034-4257. doi: <https://doi.org/10.1016/j.rse.2016.02.014>. URL <https://www.sciencedirect.com/science/article/pii/S0034425716300426>.

- [102] Magnus Wettle, Vittorio E. Brando, and Arnold G. Dekker. A methodology for retrieval of environmental noise equivalent spectra applied to four hyperion scenes of the same tropical coral reef. *Remote Sensing of Environment*, 93:188–197, 10 2004. ISSN 00344257. doi: 10.1016/j.rse.2004.07.014.
- [103] Stephen Sagar, Vittorio Brando, and Malcolm Sambridge. Noise estimation of remote sensing reflectance using a segmentation approach suitable for optically shallow waters. *IEEE Transactions on Geoscience and Remote Sensing*, 52:7504–7512, 2014. ISSN 01962892. doi: 10.1109/TGRS.2014.2313129.
- [104] J. Hedley, C. Roelfsemab, B. Koetz, and S. Phinn. Capability of the sentinel 2 mission for tropical coral reef mapping and coral bleaching detection. *Remote Sensing of Environment*, 02 2012.
- [105] Jay Sylvain, Mireille Guillaume, Audrey Minghelli, Yannick Deville, Malik Chami, Lafrance Bruno, and Véronique Serfaty. Hyperspectral remote sensing of shallow waters: Considering environmental noise and bottom intra-class variability for modeling and inversion of water reflectance. *Remote Sensing of Environment*, 200:352,367, 11 2017.
- [106] Rodrigo A. Garcia, Lachlan I.W. McKinna, John D. Hedley, and Peter R.C.S. Fearn. Improving the optimization solution for a semi-analytical shallow water inversion model in the presence of spectrally correlated noise. *Limnology and Oceanography: Methods*, 12:651–669, 2014. ISSN 15415856. doi: 10.4319/lom.2014.12.651.
- [107] Guorui Jia, Qian Xue, and Huijie Zhao. Uncertainty analysis for surface reflectance retrieved from hyperspectral remote sensing image using empirical line method. In *2018 9th Workshop on Hyperspectral Image and Signal Processing: Evolution in Remote Sensing (WHISPERS)*, pages 1–5, 09 2018. doi: 10.1109/WHISPERS.2018.8747131.
- [108] Nicolas Thomas, Marc Lennon, Céline Danilo, Guillaume Sicot, Mohamed Ali Ghanami, and Sophie Loyer. A method for propagating uncertainties of the top of atmosphere sentinel-2 measurements to bottom of atmosphere reflectance for aquatic applications. In *2021 11th Workshop on Hyperspectral Imaging and Signal Processing: Evolution in Remote Sensing (WHISPERS)*, pages 1–5, 2021. doi: 10.1109/WHISPERS52202.2021.9484050.
- [109] Elliot Pachniak, Yongzhen Fan, Wei Li, and Knut Stamnes. Quantifying uncertainties in oc-smart ocean color retrievals: A bayesian inversion algorithm. *Algorithms*, 16(6): 301, 2023. doi: 10.3390/a16060301.
- [110] J. Hedley, C. Roelfsema, and S. Phinn. Propagating uncertainty through a shallow water mapping algorithm based on radiative transfer model inversion. In *Proceedings of Ocean Optics XX*, Anchorage, AK, USA, 2010.

- [111] ZhongPing Lee, Robert Arnone, Chuanmin Hu, P. Jeremy Werdell, and Bertrand Lubac. Uncertainties of optical parameters and their propagations in an analytical ocean color inversion algorithm. *Applied Optics*, 49(3):369–381, 2010. doi: 10.1364/AO.49.000369.
- [112] Stéphane Maritorena and David A. Siegel. Consistent merging of satellite ocean color data sets using a bio-optical model. *Remote Sensing of Environment*, 94(4):429–440, 2005. ISSN 0034-4257. doi: <https://doi.org/10.1016/j.rse.2004.08.014>. URL <https://www.sciencedirect.com/science/article/pii/S0034425704002834>.
- [113] Mhd. Suhyb Salama, Frederic Melin, and Rogier Van der Velde. Ensemble uncertainty of inherent optical properties. *Optical Society of America*, 2011.
- [114] Michael Sydor, Richard Gould, Robert Arnone, Vladimir Haltrin, and Wesley Goode. Uniqueness in remote sensing of the inherent optical properties of ocean water. *Applied optics*, 43:2156–62, 04 2004. doi: 10.1364/AO.43.002156.
- [115] Michael Defoin-Platel and Malik Chami. How ambiguous is the inverse problem of ocean color in coastal waters? *Journal of Geophysical Research*, 112:C03004, 2007. doi: 10.1029/2006JC003847.
- [116] Rodrigo A. Garcia, Zhongping Lee, and Eric J. Hochberg. Hyperspectral shallow-water remote sensing with an enhanced benthic classifier. *Remote Sensing*, 10(1):147, 2018. doi: 10.3390/rs10010147.
- [117] Guillaume Sicot, Mohamed Ali Ghannami, Marc Lennon, and Sophie Loyer. Estimability study of the parameters of the semi-analytical lee model with hyperspectral data. *IEEE WHISPER*, page Unknown Pages, 2021.
- [118] Franz-Georg Wieland, Adrian L. Hauber, Marcus Rosenblatt, Christian Tönsing, and Jens Timmer. On structural and practical identifiability. *Current Opinion in Systems Biology*, 25:60–69, 3 2021. doi: 10.1016/j.coisb.2021.03.005.
- [119] Luc Pronzato and Andrej Pazman. *Design of Experiments in Nonlinear Models*. Springer, 2013.
- [120] Mireille Guillaume, Audrey Minghelli, Malik Chami, and Manchun Lei. Determination of bayesian cramér–rao bounds for estimating uncertainties in the bio-optical properties of the water column, the seabed depth and composition in a coastal environment. *Remote Sensing*, 15(9):2242, 2023. doi: 10.3390/rs15092242.
- [121] Richard H. Byrd, Robert B. Schnabel, and Gerald A. Shultz. Approximate solution of the trust region problem by minimization over two-dimensional subspaces. *Mathematical Programming*, 40(1):247–263, 1988. ISSN 1436-4646. doi: 10.1007/BF01580735. URL <https://doi.org/10.1007/BF01580735>.

- [122] Yifan Zhan, Shohei Nobuhara, Ko Nishino, and Yinqiang Zheng. Nerfrac: Neural radiance fields through refractive surface. In *Proceedings of the IEEE/CVF International Conference on Computer Vision (ICCV)*, pages 18402–18412, 11 2023.
- [123] Jen-I Pan, Jheng-Wei Su, Kai-Wen Hsiao, Ting-Yu Yen, and Hung-Kuo Chu. Sampling neural radiance fields for refractive objects. In *SIGGRAPH Asia 2022 Technical Communications*, SA '22, New York, NY, USA, 2022. Association for Computing Machinery. ISBN 9781450394659. doi: 10.1145/3550340.3564234. URL <https://doi.org/10.1145/3550340.3564234>.
- [124] Alp Kucukelbir David M. Blei and Jon D. McAuliffe. Variational inference: A review for statisticians. *Journal of the American Statistical Association*, 112(518):859–877, 2017. doi: 10.1080/01621459.2017.1285773.
- [125] Mark J. van der Laan and Daniel Rubin. Targeted maximum likelihood learning. *The International Journal of Biostatistics*, 2(1), 2006. doi: doi:10.2202/1557-4679.1043. URL <https://doi.org/10.2202/1557-4679.1043>.
- [126] Thomas A. Severini. *Likelihood Methods in Statistics*. Oxford Statistical Series, 03 2000.
- [127] Robin M. Pope and Edward S. Fry. Absorption spectrum (380–700 nm) of pure water. ii. integrating cavity measurements. *Appl. Opt.*, 36(33):8710–8723, 11 1997. doi: 10.1364/AO.36.008710. URL <https://opg.optica.org/ao/abstract.cfm?URI=ao-36-33-8710>.
- [128] Annick Bricaud, Marcel Babin, André Morel, and Hervé Claustre. Variability in the chlorophyll-specific absorption coefficients of natural phytoplankton: Analysis and parametrization. *Journal of Geophysical Research*, 100:13,321–13,332, 07 1995. doi: 10.1029/95JC00463.
- [129] Marcel Babin, Dariusz Stramski, Giovanni M. Ferrari, Herve Claustre, Annick Bricaud, Grigor Obolensky, and Nicolas Hoepffner. Variations in the light absorption coefficients of phytoplankton, nonalgal particles, and dissolved organic matter in coastal waters around europe. *Journal of Geophysical Research: Oceans*, 108(C7), 2003. doi: <https://doi.org/10.1029/2001JC000882>. URL <https://agupubs.onlinelibrary.wiley.com/doi/abs/10.1029/2001JC000882>.
- [130] Xiaolong Yu, Zhongping Lee, and Wendian Lai. Global distribution of the spectral power coefficient of particulate backscattering coefficient obtained by a neural network scheme. *Remote Sensing of Environment*, 296:113750, 2023. ISSN 0034-4257. doi: <https://doi.org/10.1016/j.rse.2023.113750>. URL <https://www.sciencedirect.com/science/article/pii/S0034425723003012>.

- [131] André Morel. Optical properties of pure water and pure sea water. *Limnology and Oceanography* - *LIMNOL OCEANOGR*, pages 1–24, 1974. doi: 10.4319/lo.2007.52.1.0217.

Titre : Inférence statistique de la profondeur de la colonne d'eau par analyses radiométrique et géométrique de l'imagerie spectrale

Mot clés : Hauteur de la colonne d'eau (WCD), Analyse radiométrique, Analyse géométrique, Imagerie spectrale, Inférence statistique, Quantification des incertitudes

Résumé : La cartographie précise des eaux peu profondes, particulièrement en zones côtières, reste un défi majeur, notamment en ce qui concerne les incertitudes dans la mesure de la profondeur de la colonne d'eau (WCD). Cette précision est essentielle tant pour la navigation que pour la recherche, qui s'est jusqu'ici principalement concentrée sur l'estimation de la WCD sans considérer pleinement les incertitudes associées. Les méthodes traditionnelles, qu'elles soient radiométriques ou géométriques, présentent chacune leurs limitations spécifiques. Notre travail propose un cadre d'inférence basé sur la vraisemblance pour estimer rigoureusement ces incertitudes. L'approche se développe selon deux axes : une analyse radiométrique fondée sur la modélisation du transfert radiatif avec des

techniques semi-analytiques, et une approche géométrique basée sur la triangulation stéréophotogrammétrique. Cette double méthodologie permet d'évaluer les biais et les erreurs inhérents à chaque approche. Le développement de ces cadres d'inférence dans les domaines radiométrique et géométrique est validé par des simulations réalistes, permettant une compréhension approfondie des incertitudes dans l'estimation de la WCD. Nos résultats démontrent l'efficacité de cette approche pour quantifier les incertitudes dans les deux types d'estimations. Cette recherche apporte une contribution significative à la télédétection passive et aux sciences marines en proposant des méthodes fiables pour évaluer les incertitudes dans la cartographie des eaux peu profondes.

Title: Statistical inference of Water Column Depth through radiometric and geometric analysis of Spectral Imagery

Keywords: Water Column Depth (WCD), Radiometric analysis, Geometric analysis, Spectral Imagery, Statistical inference, Uncertainties quantification

Abstract: The complexities of mapping shallow water bodies, particularly coastal areas, have long been studied, yet a focused understanding of Water Column Depth (WCD) uncertainties remains notably lacking. While accurate measurement of these uncertainties is crucial for reliable bathymetric charts and safe navigation, current research has primarily focused on WCD estimation without considering associated uncertainties. Traditional approaches, whether radiometric or geometric analyses of spectral imagery, face distinct limitations in optically complex waters and featureless seabeds, respectively. Our work introduces a likelihood-based inference framework designed for robust estimation of WCD uncertainties through two main objectives. First, we develop a radiometric inferential approach

based on Radiative Transfer (RT) modeling with Semi-Analytical (SA) techniques, enabling detailed analysis of uncertainties and inherent biases. Second, we establish a geometric inferential approach using stereo-photogrammetric triangulation to evaluate WCD uncertainties from a geometric perspective. These frameworks are validated through realistic simulations, focusing on understanding and quantifying WCD uncertainties. Our findings confirm the effectiveness of the likelihood-based inference framework in quantifying uncertainties for both radiometric and geometric WCD estimations. This research makes a significant contribution to passive remote sensing and marine science by providing reliable, comprehensive methods for assessing uncertainties in shallow water mapping.